Optical spectroscopy of thin film semiconductor structures

Eggleston, James Michael

OPTICAL SPECTROSCOPY OF THIN FILM SEMICONDUCTOR STRUCTURES

by James Michael Eggleston

Submitted for the degree of Ph.D.

University of Durham

Department of Physics, 1997.

TABLE OF CONTENTS

TABLE OF FIGURES

This thesis is dedicated to my family, especially Mam, Aunty Biz and Uncle Dez.

The little I have accomplished in life would have been impossible without the help you have all provided.

It is your care, harassment and beer that has enabled me to complete this thesis.

Thank you for so much.

I hearby declare that the work contained within this thesis is my own work and nothing that is a result of collaboration unless otherwise stated. No part of this work has been submitted for a degree or other qualification at this or any other university.

ABSTRACT

This thesis consists of a study of several thin film semiconductor structures of practical technological use either presently or in the near future.

The first system studied is an ultra thin film single crystal gallium arsenide layer. The absorption spectra of these layers are measured and transitions at both the Γ-point and L-point of the Brillouin Zone are observed, the latter are not normally measurable in thicker layers. The observed shift in the Γ-point absorption edge is attributed to contributions from the Franz-Keldysh Effect and the Moss-Burstein Effect. The temperature dependence of the L-point energy gap is measured and compared with previous data.

The next system investigated is an n-type porous silicon layer coated with p-type polyaniline. Both photoluminescence and electroluminescence spectra and the electrical characteristics have been measured for this system. The interface between the two layers is found to be a rectifying junction consistent with a potential barrier formed at the interface. In forward bias, it is possible to generate electroluminescence in the visible and near infra red regions.

The final structure studied is a thin film cadmium sulphide-cadmium telluride solar cell structure. The cells are found to have a low efficiency of around 1% as grown, but a process of treatment with cadmium chloride and annealing in air improves this by a factor of approximately ten. Photoluminescence measurements on the back surface of the cadmium telluride revealed three major emission bands at 1.59 eV, 1.55 eV and 1.45 eV. By varying temperature and incident laser power, attempts at assigning the bands to specific impurity centres in the cadmium telluride is made.

Using a novel bevelling etch technique to prepare samples, depth dependent measurement of the photoluminescence is possible. This reveals that the major changes associated with the improvement in efficiencies occurs at the interface between the CdS and the CdTe.

1. INTRODUCTION

This thesis aims to give an appreciation of the applications of optical spectroscopy in the analysis and understanding of semiconductor materials. Materials in the solid state have energy levels filled with the electrons from the constituent atoms and the spectroscopic techniques discussed here probe the separation, population and nature of these energy levels by the use of electromagnetic radiation.

From the data gathered it is often possible to infer information on the internal energy levels of the solids. Absorption and luminescence spectra can give information about which energy levels are normally present. By choosing a variety of samples which have been either differently treated or grown, it is sometimes feasible to investigate the process of how energy states are created or which energy states are associated with which of the elements present.

Chapter two contains the theory required to explain the origin of the physical properties of solids in terms of the nature of the electronic states and transitions which occur between them. Also covered are the fundamental concepts required to understand the physics of the measurements.

The techniques and equipment used to make the measurements are introduced in Chapter three, along with computer interfacing and calibration of the experimental apparatus required for the particular system developed for this thesis.

The following four chapters cover particular sets of experiments on three different types of semiconductor materials and devices. These are thin film gallium arsenide epitaxial layers, porous silicon/ conducting polymer layers and thin film cadmium

sulphide/cadmium telluride (CdS/CdTe) solar cells. In studying these materials, a wide variety of semiconductor devices, materials and technologies are covered.

GaAs is a widely available semiconductor material and by preparing very thin layers of the material it is possible to study its band structure and fundamental properties though absorption experiments. Previously, such measurements had not been made in the region of the spectrum corresponding to the L-point transition as any effects were masked by the absorption at the Γ-point which occurs at a lower energy. Other measurements of the transition have used thicker material and more indirect methods of measuring the energy gap.

Although porous silicon has been known about for many years it has been pushed to the forefront of research relatively recently. It was discovered by Canham et al [1] in 1990 that it was possible to excite visible luminescence from it, which meant it had the unusual and technologically advantageous property of being radiative despite silicon having an indirect bandstructure, providing a possible means of enabling luminescent devices to be fabricated on silicon. We have found it is possible to create a device which emits light under a forward bias by using a conducting organic polymer, polyaniline, as a contact to the porous silicon.

Finally, although thin film CdS/CdTe solar cell structures are already commercially available for the production of photovoltaic power from sunlight, further improvements can still be made in the efficiency of these devices. Small scale cells have already been produced with efficiencies in excess of 15%[2]. Fabrication of these cells involves a treatment which improves the cell efficiency from ≈1% to ≈10% and the process that causes this order of magnitude increase is not fully understood. It is hoped that this improvement in efficiency could be further increased if the underlying mechanisms of the cell improvement could be found.

2. THEORY

This chapter provides an overview of the theoretical foundations of modern solid state theory. We start with the Schrödinger Wave Equation for an electron in any crystalline material based upon a periodic lattice structure then from that deduce the band structure associated with the lattice. The electrical and optical properties of these bands along with the properties of impurities and imperfections in that lattice are then introduced and the properties of the vibrations of the lattice conclude this chapter.

.

2.1. Lattices and Reciprocal Space

The concept of reciprocal space is essential to the mathematical treatment of solids. Because of the self-repeating periodic nature of the material, it is simpler to treat the electrons in terms of their momentum-energy relationship rather than their position-energy relationship. This is a consequence of the solution of the Schrödinger equation which gives energy eigenstates which describe electrons using energy-momentum co-ordinates.

For any Bravais lattice, with primitive lattice vectors $\underline{a}_i$ which define the unit cell of the lattice, the relationship:

$$\underline{R} = \sum_{i=1,2,3} \underline{a}_i$$

gives $\underline{R}$, which in the approximation of an infinite lattice, is a vector from any point

in the lattice to another *identical* point in the lattice.

As moving through the lattice space under the transformation $\underline{r} \rightarrow \underline{r} + \underline{R}$ does not affect the surroundings of an electron (the electron will be unable to tell whether it is at $\underline{r}$ or $(\underline{r} + \underline{R})$ as there will be an infinite lattice surrounding it in both locations), it should be expected that any physical property, f, dependant on the electrons of the lattice should not be altered either, as the electron will be subject the same potential in both spatial locations, i.e. $f(\underline{r}) \equiv f(\underline{r} + \underline{R})$. In reality, the lattice will not be infinite and so the point cannot be said to be truly identical but the spatial extent of an electron wavefunction compared to the dimensions of a real lattice means that this is a valid approximation.

Since f is a periodic function it must be possible to express it as a Fourier Series:

$$f(\underline{r}) = \sum_{\underline{g}} A_{\underline{g}} \exp(i\underline{g}.\underline{x})$$

where $\underline{g} = \underline{b}_1 + \underline{b}_2 + \underline{b}_3$, with $\underline{b}_1 = 2\pi \frac{\underline{a}_2 \times \underline{a}_3}{\underline{a}_1 \cdot (\underline{a}_2 \times \underline{a}_3)}$, $\underline{b}_2 = 2\pi \frac{\underline{a}_3 \times \underline{a}_1}{\underline{a}_1 \cdot (\underline{a}_2 \times \underline{a}_3)}$ and $\underline{b}_3 = 2\pi \frac{\underline{a}_1 \times \underline{a}_2}{\underline{a}_1 \cdot (\underline{a}_2 \times \underline{a}_3)}$. Note that $\underline{g}$ has the units of inverse length (hence the term *reciprocal* lattice). The vectors $\underline{b}_i$ are the reciprocal lattice vectors and define the building block of the reciprocal lattice, in the same way as the $\underline{a}_i$'s define the building block of the spatial lattice.

Note that the smallest possible volume enclosed by the $\underline{b}_i$ vectors corresponds to the largest volume enclosed by the $\underline{a}_i$ vectors. This volume is known as the first Brillouin Zone and is a fundamental tool in the description of physical processes in the solid state. It is formed when the $\underline{a}_i$ vectors describe a unit cell of large size, i.e.

when the unit cell encompasses a large number of atoms. Because it contains a large amount of the lattice all the information about the solid that is needed to understand the physical properties is contained within the first Brillouin Zone. Although it will not be necessary to go into the construction of the Brillouin Zone it is necessary to understand the notation used to represent points in reciprocal space.

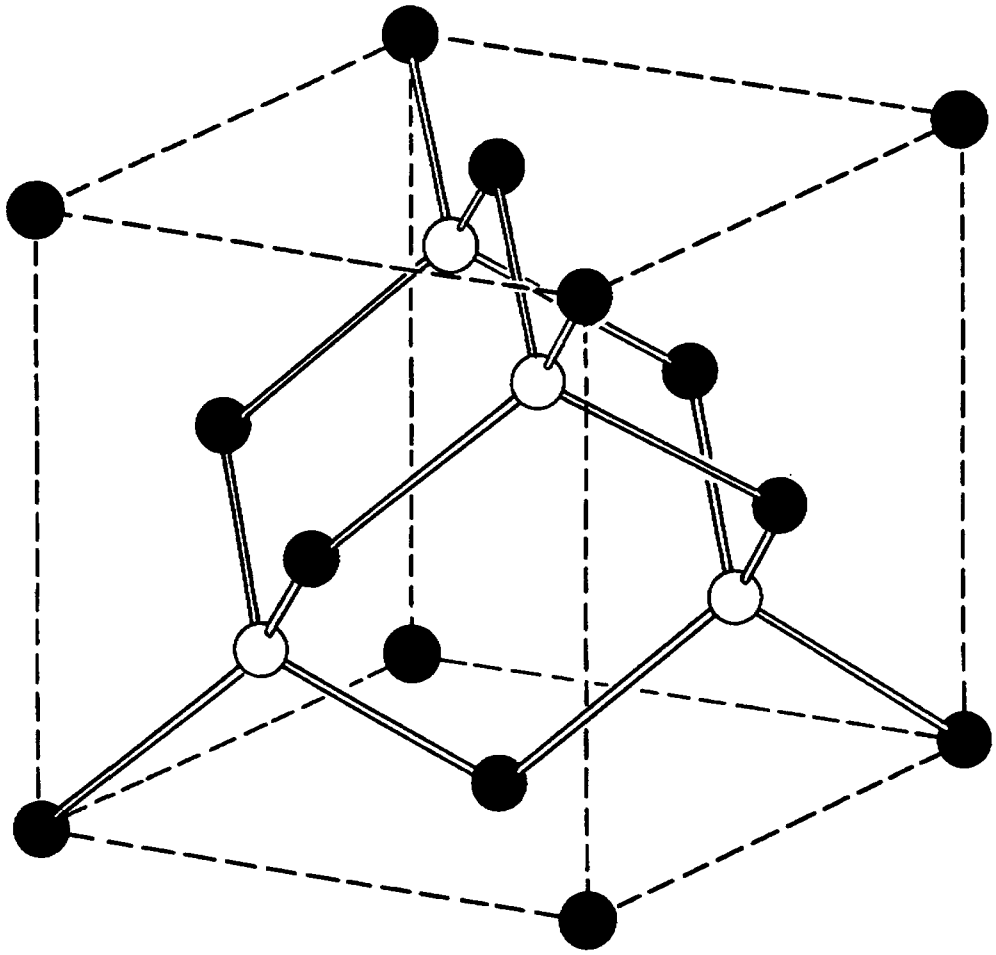

Figure 1: Zinc blende, or face centred cubic, structure

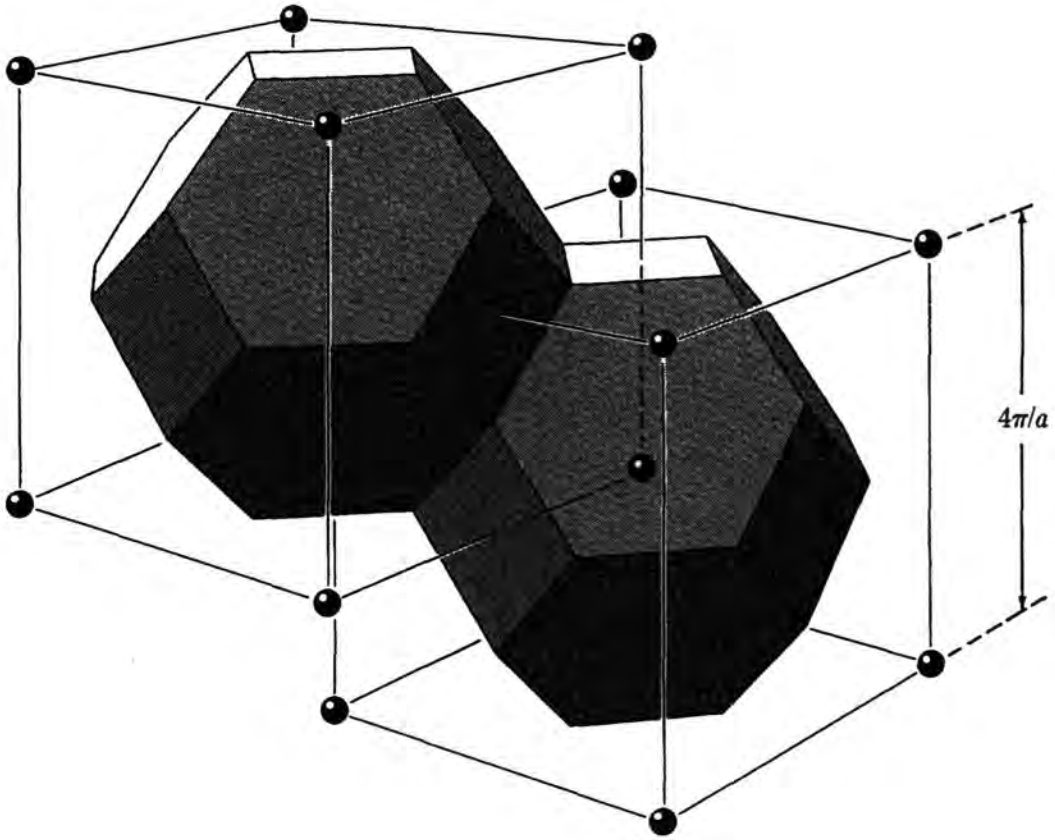

Figure 2: The 1st Brillouin Zone for a zinc blende semiconductor (having a body centred cubic reciprocal lattice)[3]

The majority of the materials mentioned in this thesis have a zinc blende structure. The zinc blende structure (shown in Figure 1) is an fcc lattice with 2 atom basis; the reciprocal lattice for this structure is a bcc lattice. Figure 2 shows the first Brillouin Zone for that lattice. Figure 3 shows a wire frame view one of these octahedrons with important points in *k*-space marked on.

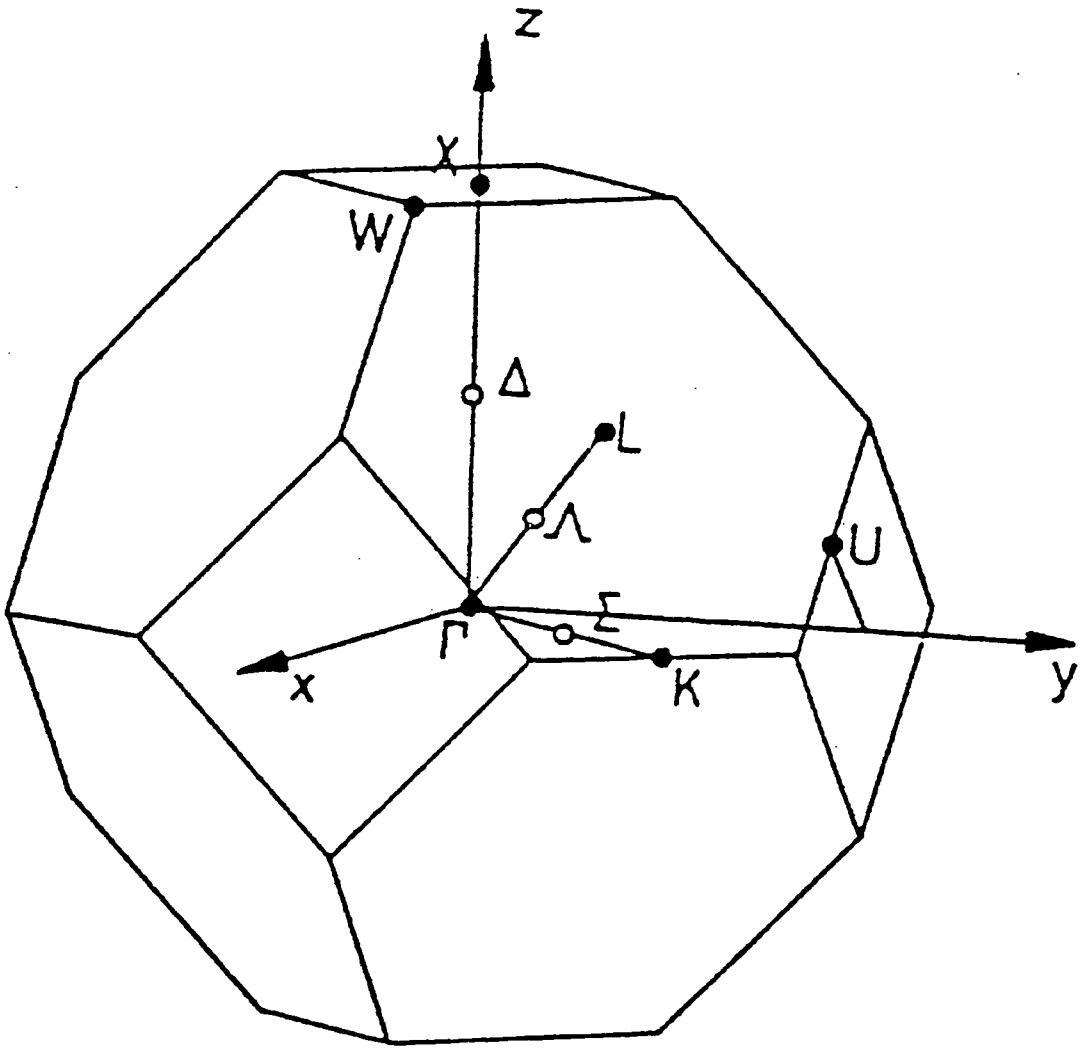

Figure 3: Locations of points in reciprocal space used in band structure diagrams

These are:

- the Γ point: the zone centre
- the X points: located along the (100) directions at the edge of the first Brillouin Zone, i.e. at the intersections of the *x*, *y* and *z* axes with the first Brillouin Zone
- the L points: located along the (111) directions at the zone boundary

- the K points: located along the (110) directions at the zone boundary
- the Δ points: midway between the Γ and X points
- the Λ points: midway between the Γ and L points
- the Σ points: midway between the Γ and K points

An *E-k* diagram shows the energy wavevector relationship for different energy bands in crystals. Generally it begins at one of the important points of symmetry and moves along an axis connecting this to other points of important symmetry. Diagrams for the materials used in the work described in this thesis can be seen at the end of section 2.2. In the style used there, the $\underline{k}$ values are plotted along the x-axis starting from one of the L points and moving to the zone centre (the Γ point) then moving along either the x, y or z axes to the X point then to the U point, which is coincident with the K point. The next part shows the behaviour of the energy along $\underline{k}$ values between the K point back to the Γ point.

2.2. Band Theory of Solids

2.2.1. Solution of the Schrödinger Wave Equation in any Periodic Lattice

Let us consider the wave equation for an electron in *any* general periodic potential for *any* value of wavevector $\underline{k}$. We will consider the one dimensional case for any wavenumber k since the mathematics is less complicated but the physics of interest is still present in the solution. To solve the problem we must find ψ, the electron wavefunction, and we start with the Schrödinger Wave Equation, $H\psi=E\psi$, for the

system, with E being the energy of the electron with associated wavefunction, ψ.

The Hamiltonian is the sum of kinetic and potential energies for the electron and so can be written as:

$$H = \frac{p^2}{2m} + U(x)$$

where p is the momentum of the electron and $U(x)$ is the potential of an electron in the lattice. Since $U(x)$ will have the same periodic property as the lattice, i.e. $U(x)=U(x+a)$, it will be possible to express it as a Fourier Series. Hence:

$$U(x) = \sum_g U_g e^{igx}$$

where g is the wavenumber of that Fourier component and U_g are the Fourier coefficients, given by:

$$U_g = \frac{1}{a}\int_{-a}^{a} U(x)e^{ngx}dx$$

The momentum operator, p, in Quantum Mechanics is $-i\hbar\partial/\partial x$ so we write $p^2 = -\hbar^2\,\partial^2/\partial x^2$ and the Schrödinger Wave Equation above becomes:

$$\left(\frac{-\hbar^2}{2m}\frac{\partial^2}{\partial x^2} + \sum_g U_g e^{igx}\right)\psi(x) = E\psi(x)$$

Assuming that $\psi(x)$ can be described as a Fourier Series (so $\psi(x) = \sum_k C_k e^{ikx}$, with $|C_k|^2$ being the probability of finding the wave in that eigenstate) lets us write this as:

$$\sum_k \frac{\hbar^2 k^2}{2m} C_k e^{ikx} + \sum_g \sum_k U_g C_k e^{i(g+k)x} = E\sum_k C_k e^{ikx}$$

Subtracting the energy term from the right hand side and factoring the equation to

take the $\sum_k e^{ikx}$ terms together:

$$\sum_k e^{ikx}\left\{\left(\frac{\hbar^2 k^2}{2m} - E\right)C_k + \sum_g U_g C_{k-g}\right\} = 0$$

Now it is clear that solutions to the wave equation can be found if:

$$\boxed{(\lambda_k - E)C_k + \sum_g U_g C_{k-g} = 0}$$

(writing $\lambda_k = \frac{\hbar^2 k^2}{2m}$, which is the energy a free electron with wavenumber, k, would have).

This is known as the *Central Equation.* It provides a set of coupled equations which connect the Fourier coefficients, U_g, of the potential $U(x)$ to the energy, E, of the solution wavefunction $\psi(x)$ and the energies,λ_k, and probabilities, C_k, of its eigenstates.

The Central Equation provides a way of determining the wavefunction of an electron, $\psi(x)$, for any $U(x)$ by providing a set of simultaneous linear equations for the coefficients in the Fourier expansion of the wavefunction. There will be as many equations as there are coefficients and the set of equations will provide a solution for ψ if the determinant for these coefficients vanishes.

2.2.2. Origin of the Band Gap at the Zone Boundaries

Let us suppose that the Fourier coefficients of the potential are small in comparison with the electron's kinetic energy at the zone boundary. We consider a wavenumber

exactly at the zone boundary and derive the energy of a wavefunction with such a wavenumber.

The two possible wavenumbers for such a situation are $k_+ = ½G$ and $k_- = -½G$, and as the kinetic energy is related to the square of the wavenumber ($k_\pm^2 = ¼G^2$ for both cases), the two will have the *same* kinetic energy so we can write $\lambda = \lambda_{k_+} = \lambda_{k_-}$.

It is clear that $C_{½G}$ and $C_{-½G}$ will be by far the most important coefficients as they have the same periodicity as the desired wavefunction so we retain only these in the two expansions of the central equation:

$$(\lambda - E)C_{½G} + UC_{-½G} = 0$$
$$(\lambda - E)C_{-½G} + UC_{½G} = 0$$

which can be written using matrices as:

$$\begin{pmatrix} (\lambda - E) & U \\ U & (\lambda - E) \end{pmatrix} \begin{pmatrix} C_{½G} \\ C_{-½G} \end{pmatrix} = \begin{pmatrix} 0 \\ 0 \end{pmatrix}$$

So there will be a non-trivial solution if

$$\begin{vmatrix} (\lambda - E) & U \\ U & (\lambda - E) \end{vmatrix} = 0$$

$$\Rightarrow (\lambda - E)^2 - U^2 = 0$$

Solving this gives two solutions denoted E_+ and E_- with $E_\pm = \lambda \pm U$. This tells us that at $k = \pm ½G$ the total energy of the solution, ψ, can take either of two values, one higher than the free electron kinetic energy by U and one lower than the free electron kinetic energy by U. The physical origin of this energy difference can be seen by considering the wavefunctions that the two solutions are associated with.

The ratio of these two coefficients $C_{½G}$ and $C_{-½G}$ gives the proportion of the wavefunction which is associated with each. Rearranging the first of the two expansions of the Central Equation above to give:

$$C_{½G} = \frac{UC_{-½G}}{(\lambda - E)}$$

lets us calculate the ratio as:

$$\frac{C_{½G}}{C_{-½G}} = \left(\frac{UC_{-½G}}{(\lambda - E)C_{-½G}} \right) = \pm 1$$

by substitution into the second central equation. So the Fourier expansion of $\psi(x)$ as:

$$\psi(x) = \sum_{k=½G,-½G} C_k e^{ikx} = \left(C_{½G} e^{\frac{iGx}{2}} + C_{-½G} e^{\frac{-iGx}{2}} \right)$$

gives two equal magnitude components ($|C_{½G}| = |C_{-½G}|$) at the zone boundaries although ratio between them may be either positive or negative($C_{½G} = \pm C_{-½G}$). Hence two versions of ψ are possible:

$$\psi_1(x) = (\exp(ikx) + \exp(-ikx)) = 2\cos(kx)$$

$$\psi_2(x) = \exp(ikx) - \exp(-ikx) = 2i\sin(kx)$$

(note that they are not normalised). It can be seen that ψ_1 represents a cosine wave and ψ_2 a sine wave. Remembering that the spatial variation of the electron depends upon the modulus of the square of the wavefunction, we get:

$$|\psi_1^2| = |(2\cos(kx))^2| = |4\cos^2(kx)| = 4\cos^2(kx)$$

$$|\psi_2^2| = |(2i\sin(kx))^2| = |-4\sin^2(kx)| = 4\sin^2(kx)$$

Figure 4 shows where the electronic charge will build up for the two possible wavefunctions:

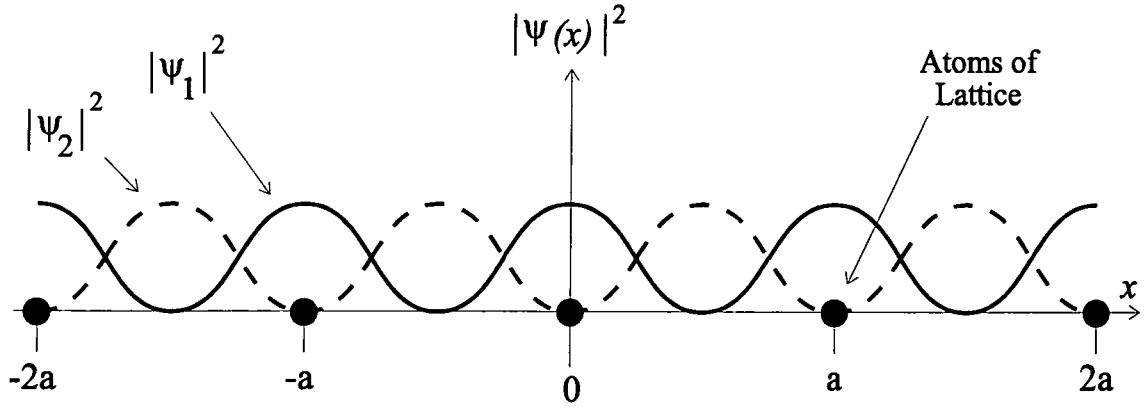

Figure 4: Distribution of electronic charge for ψ at the zone boundaries

For ψ_1, the electron will spend most of the time at the lattice sites, where the potential is lower than the average potential, giving these electrons a lower energy than a travelling electron sampling an average potential. Conversely, ψ_2 piles the electrons between the lattice sites where the potential of the electrons is higher and they will therefore have a higher energy than would a wave which sampled an average potential. That is the ψ_1 wavefunction will have an lower energy E_- associated with it and ψ_2 will have a higher energy E_+ associated with it. We have a situation at the zone boundaries where the electrons can have either of two allowed energies, but not an energy from the region between these two, which includes the energy that electron would have if it were moving freely.

2.2.3. Band Structure near the Zone Boundaries

To examine the behaviour of the energy momentum relationship *near* the zone boundary, we assume the two eigenstates related to $C_{½G}$ and $C_{-½G}$ are the still major components of ψ and solve the Central Equation for non-zone edge conditions. So we write:

$$\psi(x) = C_k e^{ikx} + C_{k-G} e^{-i(k-G)x}$$

which gives two versions of the Central Equation:

$$(\lambda_k - E)C_k + UC_{k-G} = 0$$

$$(\lambda_{k-G} - E)C_{k-G} + UC_k = 0$$

Again, these can be written as a matrix equation:

$$\begin{pmatrix} (\lambda_k - E) & U \\ U & (\lambda_{k-G} - E) \end{pmatrix} \begin{pmatrix} C_k \\ C_{k-G} \end{pmatrix} = \begin{pmatrix} 0 \\ 0 \end{pmatrix}$$

which has non-trivial solutions for:

$$\begin{vmatrix} (\lambda_k - E) & U \\ U & (\lambda_{k-G} - E) \end{vmatrix} = 0$$

so:

$$E^2 - (\lambda_k + \lambda_{k-G})E + (\lambda_k \lambda_{k-G} - U^2) = 0$$

This can be solved easily as it is quadratic in E and its solutions are:

$$E = \frac{\lambda_k + \lambda_{k-G}}{2} \pm \sqrt{¼(\lambda_k - \lambda_{k-G})^2 + U^2}$$

It is easier to consider the behaviour near the zone boundary by making the substitution $K = k - \frac{1}{2}G$, so K represents the distance (in reciprocal space) away from the zone edge. Replacing k with K (by substituting $k = K + \frac{1}{2}G$) simplifies the expression for the energy to:

$$E = \frac{\hbar^2}{2m}\left(K^2 + \tfrac{1}{4}G^2\right) \pm U\left(1 + \frac{4\lambda}{U^2}.\frac{\hbar^2 K^2}{2m}\right)^{\frac{1}{2}}$$

As K is the wavevector difference from the zone boundary thus will be small for the regions we are considering, the last term can be expanded using the Binomial Expansion of $(1+x)^{\frac{1}{2}}$ for small x ($(1+x)^{1/2} = 1 + \frac{1}{2}x + \frac{1/2.-1/2}{2}x^2 + ...$) and the terms in x that are quadratic or above neglected. So:

$$E = \left\{\frac{\hbar^2}{2m}\left(\tfrac{1}{4}G^2\right) \pm U\right\} + \left\{\frac{\hbar^2 K^2}{2m} \pm \frac{2\lambda}{U}.\frac{\hbar^2 K^2}{2m}\right\}$$

where we recognise the terms in the first bracket as being the energy at the zone boundary determined earlier as E_+ and E_-. Therefore, the energy varies for wavenumbers near the zone boundaries as:

$$E = E_{\pm} \pm \left(1 + \frac{2\lambda}{U}\right)\frac{\hbar^2 K^2}{2m}$$

From section 2.2.2 we know that at the zone edge, the solution to the Central Equation provides two solutions with different energies. The energy near the zone edge has now been seen to vary quadratically with K, the distance from zone edge. The upper energy solution, E_+ has a positive coefficient for the k^2 term and so curves upwards while the lower energy solution curves downwards meaning that there are no k values which give a value of E in between E_+ and E_-. Remembering that away

from the zone edge we would expect the solution to follow the free electron solution allows us to sketch Figure 5 as an approximation for the *E-k* diagram for the electrons in a solid.

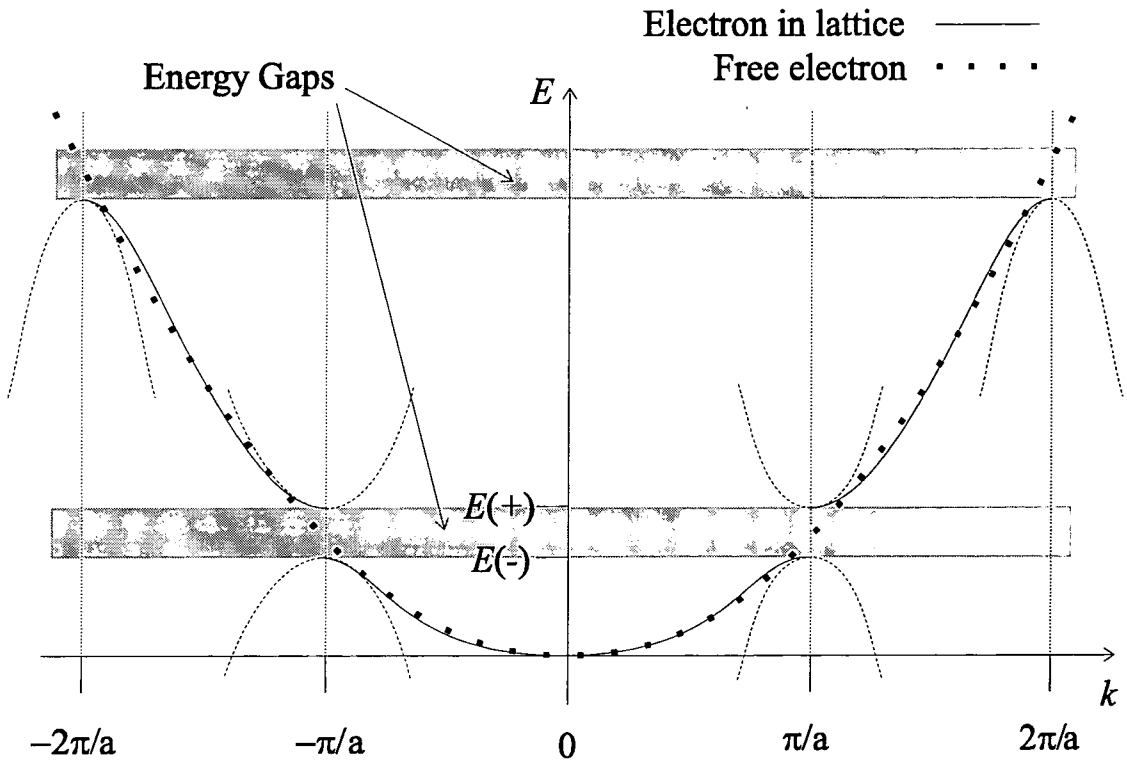

Figure 5: Electronic band structure for the Nearly Free Electron Model

2.2.4. The Kronig - Penney Model

In order to fully appreciate the nature of the bands at any general k value it is necessary to use the Kronig - Penney model[4], which uses a square well type function for the periodic potential with a being the potential well width and b being the width of the barriers, as in Figure 6. The approach adopted uses the Central Equation and is attributed to Singh[5]. We will look at the model with the limit of the potential barriers becoming spikes as $b \to 0$, $U_0 \to \infty$ whilst $U_0 b = \text{constant}$ and so are described using delta functions.

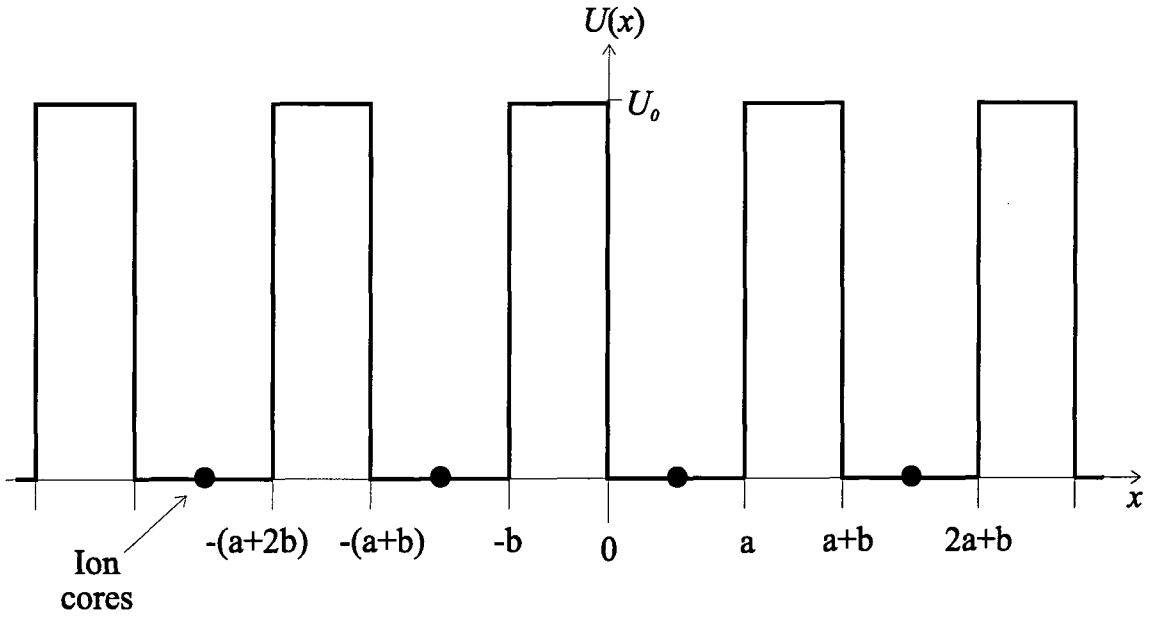

Figure 6: The Kronig - Penney model lattice potential

The potential $U(x)$ is constructed from these delta functions as:

$$U(x) = A\sum_{s=-\infty}^{\infty}\delta(x - sa)$$

As it is periodic it can described using the Fourier Series approach, with the Fourier coefficients U_g given by the integral over the period of $U(x)$ by:

$$U_g = \frac{2}{(a+b)}\int_{-b}^{a} U(x)\cos(gx)dx$$

Substituting the above expression for $U(x)$ gives:

$$U_g = Aa\sum_{s=-\infty}^{\infty}\int_{-b}^{a}\delta(x - sa)\cos(gx)dx$$

It can be seen that since the delta function behaves as $\delta(x)=0$ everywhere between the limits of the integral except at $x=0$, the integral reduces to:

$$U_g = A\sum_{s=0}\cos(gsa) = A\cos(0) = A$$

All the U_g's are equal to A, a constant. There is no decrease in the magnitude of the higher orders due to the abruptness of the delta function (i.e. to obtain an accurate Fourier expansion of the delta function it is necessary to include far more terms of the expansion than for a smoother function).

The Central Equation is now:

$$(\lambda_k - E)C_k + A\sum_n C_{k-\frac{2n\pi}{a}} = 0$$

which we need to solve for E.

First define $f_k = \sum_n C_{k-\frac{2n\pi}{a}}$ and remembering that $\lambda_k = \frac{\hbar^2 k^2}{2m}$ the above version of the Central Equation above can be rewritten with C_k as the subject:

$$C_k = \frac{-\left(\frac{2mA}{\hbar^2}\right)f_k}{\left(k^2 - \frac{2mE}{\hbar^2}\right)}$$

Obviously $f_k = f_{k-\frac{2n\pi}{a}}$ since both involve a sum over all n. It can be seen that:

$$C_{k-\frac{2n\pi}{a}} = -\frac{\frac{2mA}{\hbar^2}f_k}{\left(k - \frac{2n\pi}{a}\right)^2 - \frac{2mE}{\hbar^2}}$$

which would be the definition of C_k with $k = k - \frac{2n\pi}{a}$ and with $f_{k-\frac{2n\pi}{a}} = f_k$.

Now, summing over both sides over n gives us:

$$\sum_n C_{k-\frac{2n\pi}{a}} = \sum_n -\frac{2mA}{\hbar^2} f_k \left(\left(k - \frac{2n\pi}{a} \right)^2 - \frac{2mE}{\hbar^2} \right)^{-1}$$

The left hand side is equal to the definition of f_k and it will cancel the f_k in the sum on the right hand side.

Re-arranging the remainder and writing $K^2 = \frac{2mE}{\hbar^2}$ gives:

$$\frac{\hbar^2}{2mA} = -\sum_n \frac{1}{\left(k - \frac{2n\pi}{a} \right)^2 - K^2}$$

Now the expression on the right hand side can be expanded by using partial fractions to give:

$$\frac{\hbar^2}{2mA} = -\frac{1}{2K} \sum_n \frac{1}{\left(k - \frac{2n\pi}{a} - K \right)} - \frac{1}{\left(k - \frac{2n\pi}{a} + K \right)}$$

or:

$$\frac{\hbar^2}{2mA} = -\frac{a}{4K} \sum_n \frac{-1}{\left(n\pi - \frac{a}{2}(k - K) \right)} - \frac{-1}{\left(n\pi - \frac{a}{2}(k + K) \right)}$$

Remembering that $\cot(x) = \sum_{n=-\infty}^{\infty} \left(\frac{1}{n\pi + x} \right)$ [6] and that cot(x)=-cot(-x) we can write:

$$\frac{\hbar^2}{2mA} = \frac{-a}{4K} \left\{ \cot\left(\frac{ka}{2} - \frac{Ka}{2} \right) - \cot\left(\frac{ka}{2} + \frac{Ka}{2} \right) \right\}$$

We can then use a trigonometric definition for the difference of two cotangents,

$$\cot(x) - \cot(y) = \frac{-2\sin(x - y)}{\cos(x - y) - \cos(x + y)}$$

we can write:

$$\frac{\hbar^2}{2mA} = \frac{-a}{4K}\left\{\frac{-2\sin(Ka)}{(\cos(ka)-\cos(Ka))}\right\}$$

so:

$$\boxed{\cos(ka) = \left(\frac{mAa^2}{2\hbar^2}\right)\left(\frac{1}{Ka}\right)\sin(Ka) + \cos(Ka)}$$

The function dependant on Ka on the right hand side of the equation above is plotted in Figure 7 and shows that for some regions of Ka (shown in grey) the value of the expression will be either greater than 1 or less than -1. As $\cos(ka)$ can only vary between ±1 no real value of k exists which can provide a solution to the equation.

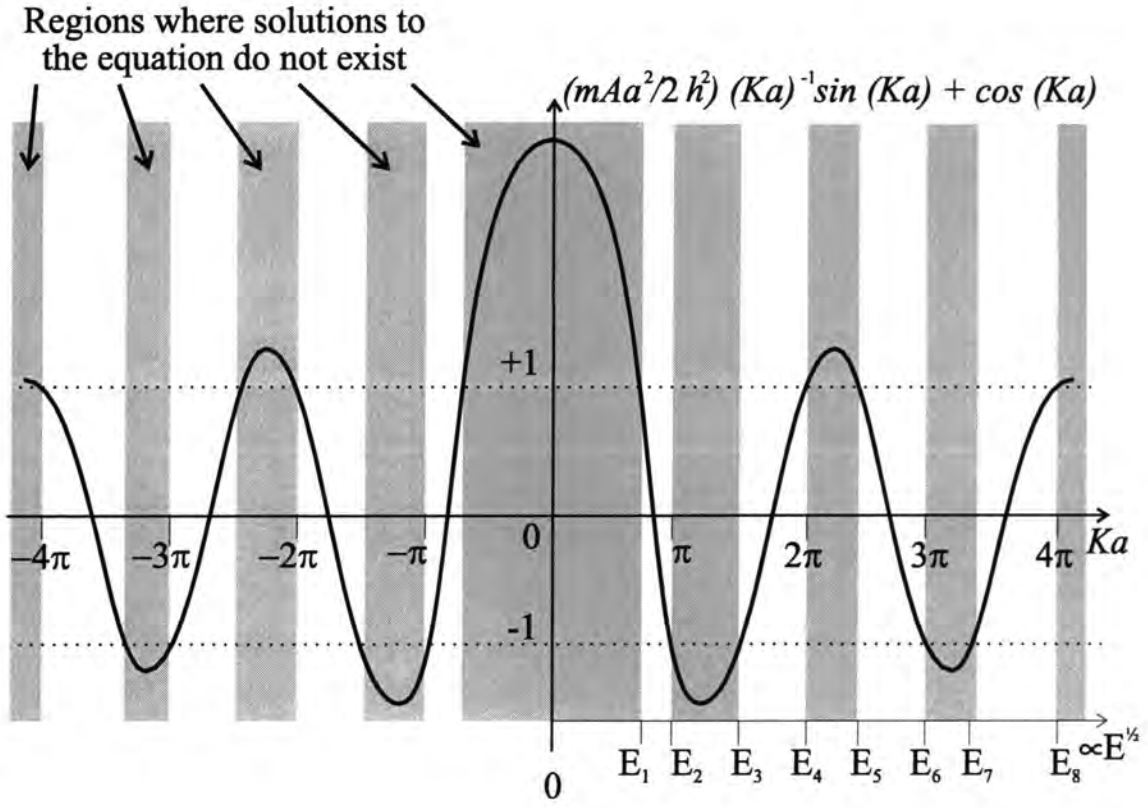

Figure 7: Plot showing the inability of certain total energy solutions to exist.

Remembering that $K^2 = \frac{2mE}{\hbar^2}$, so that the x-axis could equally be proportional to the square root of energy, reveals that not all values of energy are allowed as solutions to the Kronig - Penney Model.

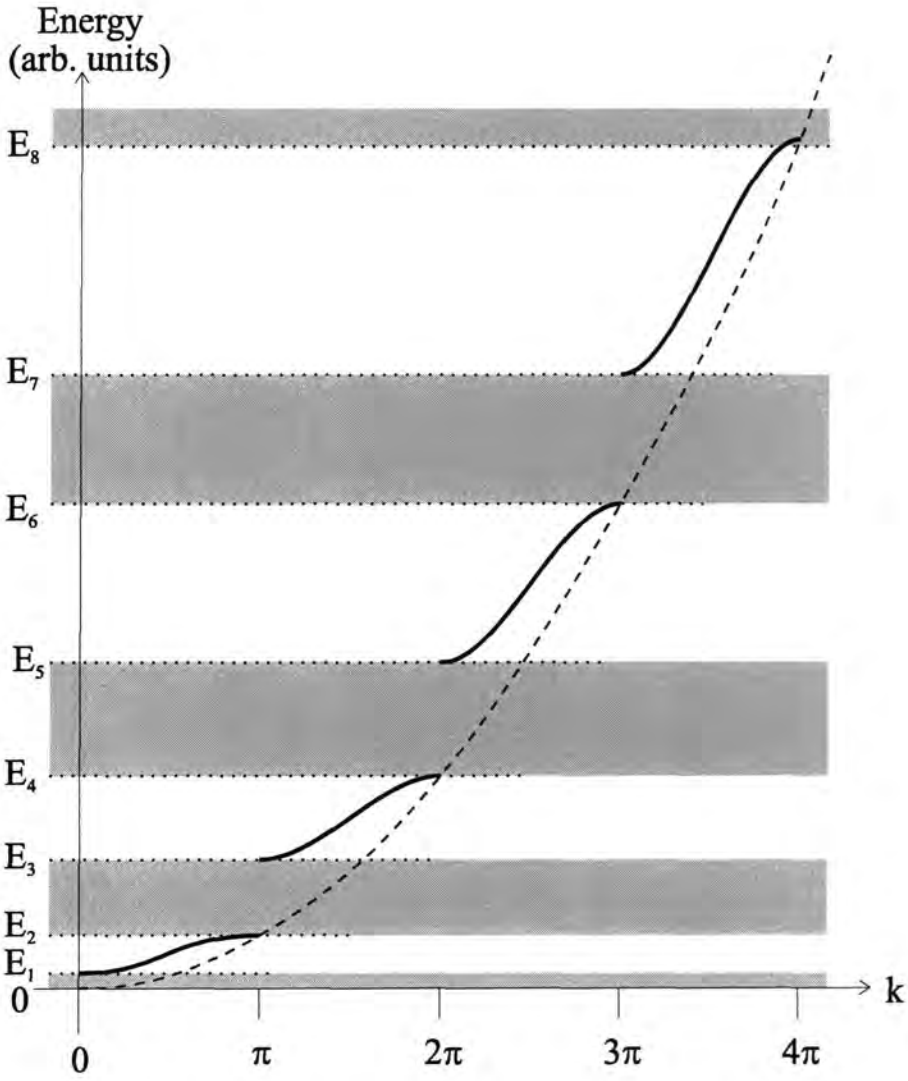

Figure 8: Band gaps in the Kronig - Penney Model

Figure 8 shows how the energy varies with wavevector k, and the lack of certain energy states in the crystal.

2.3. Real Bandstructures

We have seen how even simple models in one dimension lead us to the conclusion that for any material in the solid state, bands of allowed energies will exist separated by regions of forbidden energies. In real materials electrons can move in three dimensions and as explained at the end of section 2.1, we show the possibilities on an *E-k* bandstructure diagram displaying the energy variation along a path passing through the three dimensions along important symmetry directions.

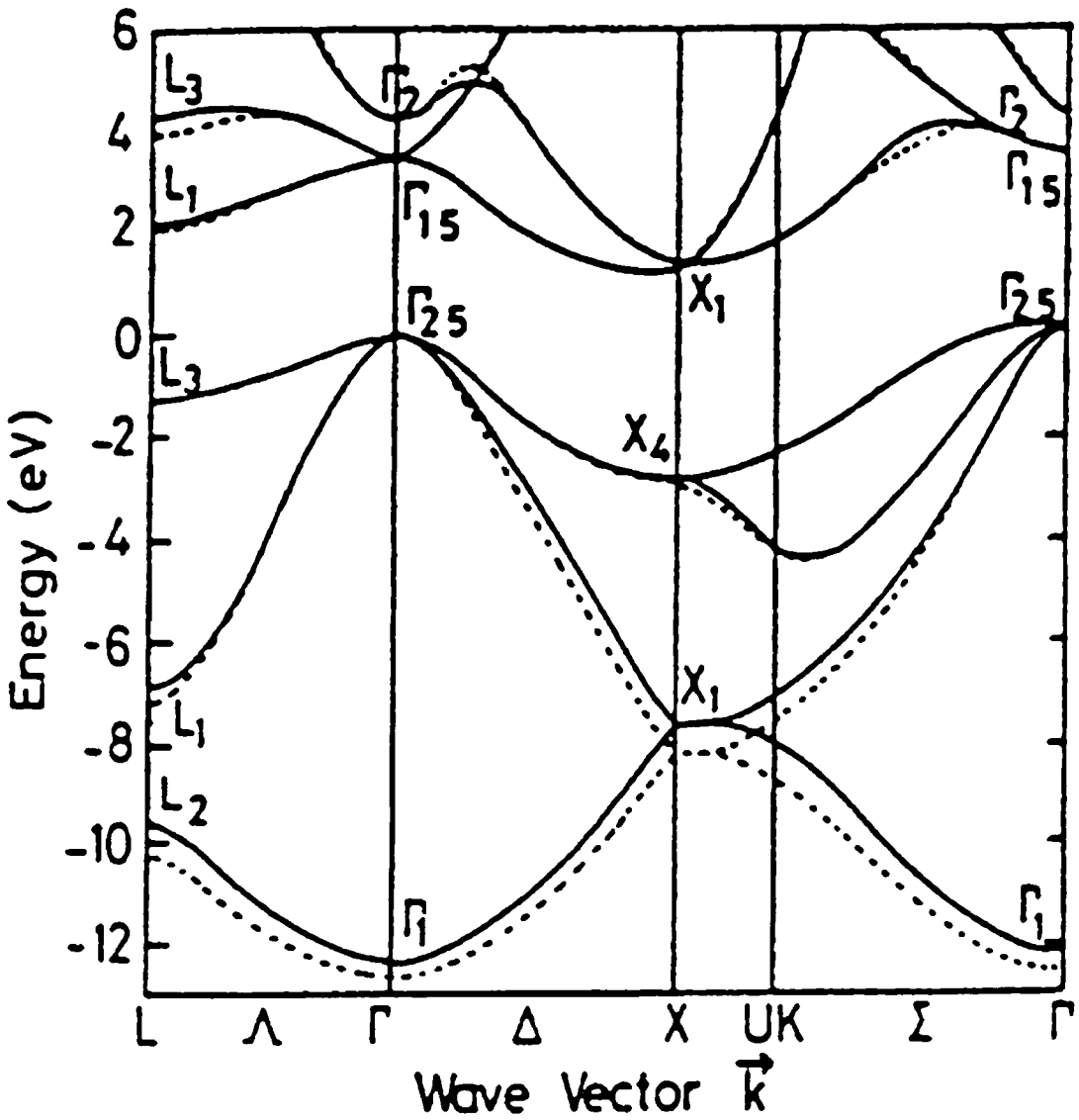

Figure 9: *E-k* Bandstructure diagram for silicon[7]

We can see from Figure 9 that it is not necessary for the minima of a higher energy band to lie directly above the maxima of the band below it as is the case in the one dimensional mathematical models presented earlier in this section. The energy scale is set to 0 eV for the highest filled energy band at absolute zero (see section 2.4), with the zone centre ($\underline{k}$=0) being defined at the topmost point of this band.

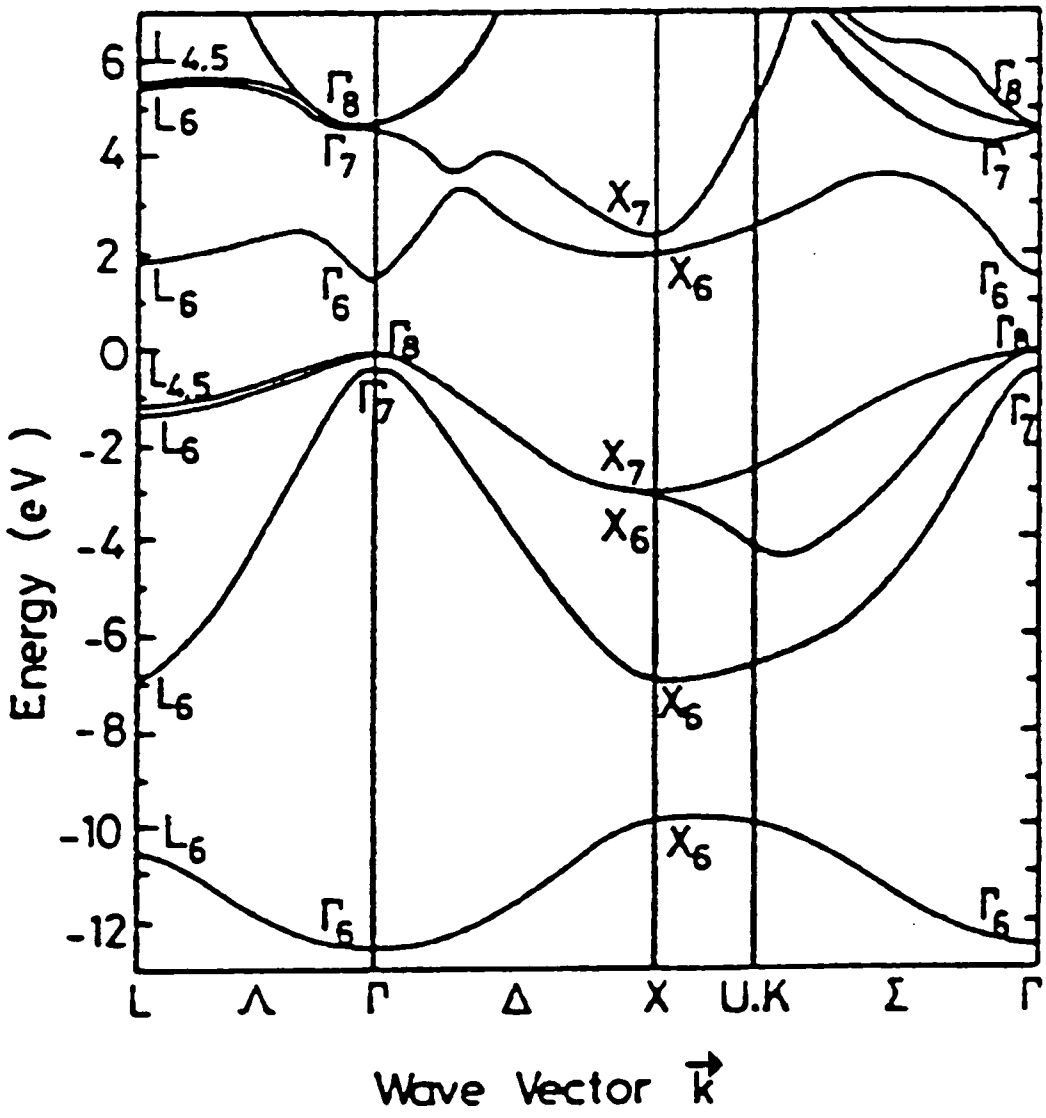

Figure 10: *E-k* Bandstructure diagram for gallium arsenide[8]

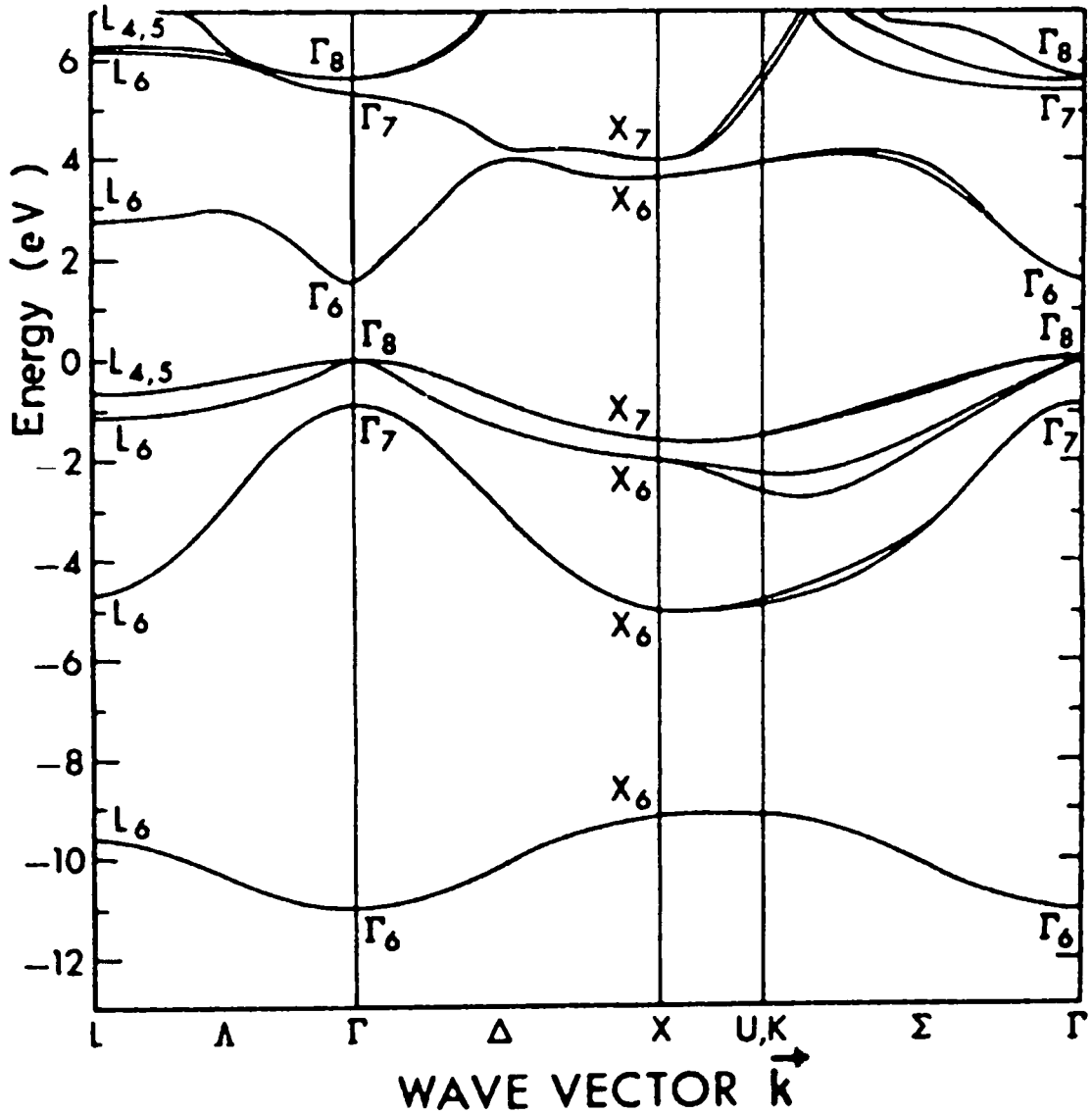

Figure 11: *E-k* bandstructure diagram for cadmium telluride[9]

2.4. Filling Bands with Electrons

2.4.1. Insulators and Conductors

Each of the bands mentioned previously consist of a quasi-continuous (the energy difference between them is $\approx 10^{-15}$ eV) series of states in which an electron can reside. Electrons, being fermions as they have spin ½, are subject to the *Pauli Exclusion Principle* which dictates that no two electrons can be in the same quantum state and

so cannot, unlike bosons, occupy or change to any state that is already occupied by an electron.

For conduction to occur, electrons must be free to move in a material. Firstly, this clearly means that if a band is to be capable of taking part in the conduction mechanism then it must possess electrons. If an electron is in a particular state and a potential difference is applied across the lattice then the electron will be subject to a force which will make it move. However, the electron can only change from the original state if there is another (final) state for it to move into which is vacant. So as a band becomes more highly populated, the probability of the final state being occupied becomes higher and the electron is less likely to be able to undergo the transition.

An insulator is a then material whose energy bands are either completely empty or completely filled. That is, we find that we have *exactly* the number of electrons required to *exactly* fill a band. This means that there are no adjacent empty states anywhere in the band for an electron to jump into so all the electrons are fixed into their current state. The application of a potential difference will have no effect on the electron distribution.

A conductor is a material which has a band which is not entirely filled. This means there are empty states for electrons to jump into and the application of a potential will result in the movement of electrons or current flow. We say a material is a metal if more than around 10% of the states in its highest occupied band are empty or occupied.

It can be demonstrated[10] that the number of electron states that can fit into a band is equal to twice the number of primitive cells in the lattice That is, each primitive cell

will contribute one k value to each energy band, which is allowed to be occupied by two electrons of differing spin. If we consider filling the bands of a material with all the electrons from atoms in the lattice according to the Pauli Exclusion Principle, we see that any lattice constructed with a primitive cell with an odd number of electrons will have a half-filled top band and any system with a base primitive cell having an even number of electrons will have a completely filled top band. Given that conduction requires empty electronic states for electrons to move into it might be assumed that all even valency atom lattices form insulators and all odd valency atom lattices form conductors.

The real situation is more complicated than this because in three dimensions bands can cross and become degenerate, allowing a fully filled band to cross an empty band and give free states for electrons to move into and conduction then to occur.

2.4.2. Semiconductors

Take a series of bands filled with electrons such that the highest occupied band is completely full (the material will be an insulator as defined above). Consider this topmost filled band and the next band above it, which has no states occupied. The energy gap separating the two bands is E_g (see Figure 12). The lower band is known as the *Valence Band (VB)* and electrons in this band cannot conduct due to the lack of free states as discussed previously. It is named the valence band because it is filled by the valence electrons of the atoms in the lattice.

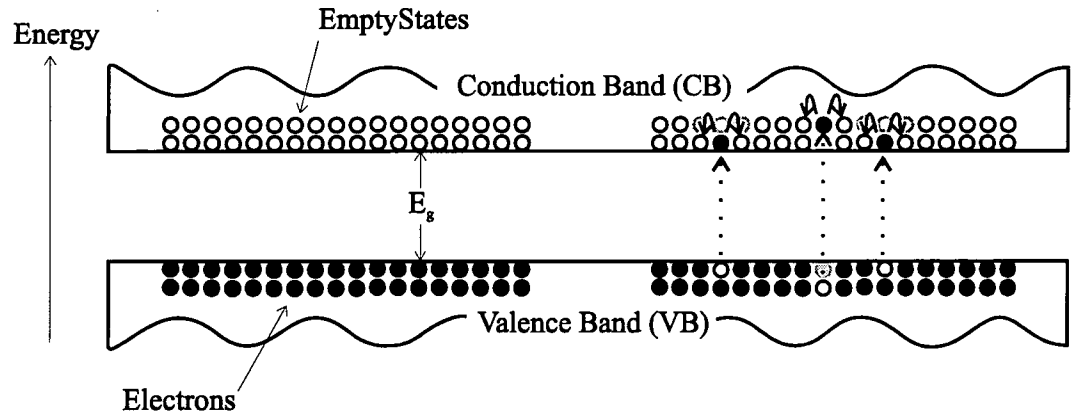

Figure 12: Occupation of bands by electrons and holes in a semiconductor

If the bands themselves are narrow compared to the energy gap then we can consider bands as having all of their states at an average energy (this is the Narrow Band model[11]). The probability, P, of an electron in the lower band gaining enough energy to promote itself into the upper band is given by Fermi - Dirac statistics:

$$P = \frac{1}{e^{\frac{E_g}{kT}} + 1}$$

Once the electrons have jumped into the higher energy band, they are then free to move as there are many empty states available with similar energies. We call the upper band the *Conduction Band (CB)*, as any electron in a state in this band will be able to conduct. In the valence band electrons are also able to move once some electrons have been promoted to the conduction band, although there are fewer of the empty states so this process is less likely.

It can also be shown that the electronic states that form the conduction band are the *s* orbitals of the atoms and the valence band states are related to the *p* orbitals. The *p* orbitals are attractive in nature and have the electron wavefunction concentrated in the space between the atoms, whilst the *s* orbitals conduct because they are repulsive in nature and are centred on the atoms.

At absolute zero the probability of any electron gaining enough energy to jump the gap is zero, but as the temperature increases, so will the chance of the electrons being promoted. All insulators then have the potential to become more conductive with increasing temperature. However if the energy gap is larger than a few electron volts the temperature needed to promote enough electrons to call the material conductive becomes high enough to melt the crystal and it is usual to call any material with an energy gap higher than around 3.5 eV an insulator.

Crystal Material	Energy Gap at Absolute Zero (eV)
Germanium	0.744
Silicon	1.17
Gallium Arsenide	1.52
Cadmium Telluride	1.607
Cadmium Sulphide	2.582

Table 2.1: Energy gaps for some semiconductors[12]

Electrons can also get the energy required to cross the gap from electromagnetic radiation passing through the crystal. Photons with an energy greater than or equal to the band gap energy can be absorbed and the energy is used to promote an electron from a valence band state into a conduction band state. The optical processes associated with these semiconductors states and more importantly with states created in the band gap by imperfections in the crystal structure are discussed later in section 2.6.

The majority of semiconductors have a *direct* energy gap with the bottom of the conduction band lying above the valence band maximum in k-space, though this is

not always observed. Silicon for example has an *indirect* energy gap, with the conduction band minima lying approximately at 0.85 of the way from the Γ point to the X point.

Figure 13 shows the two different possibilities for the energy gap.

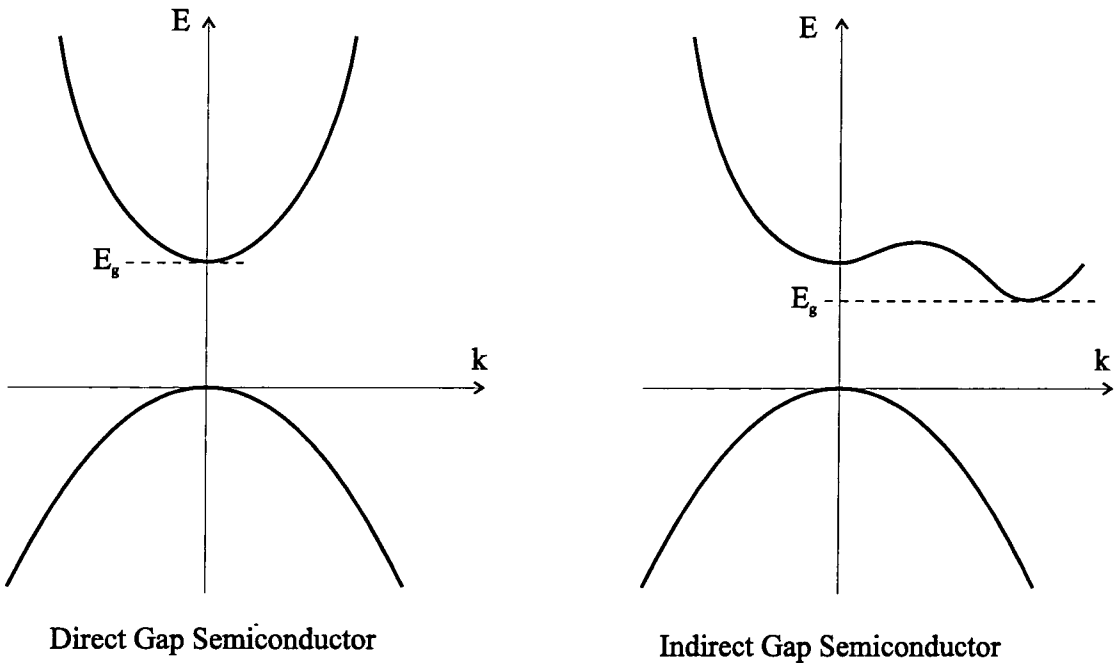

Figure 13: Direct and indirect energy gaps

2.4.3. Behaviour of Electrons in a Band

It can be shown[13], that the electrons behave as is they possess an effective mass, m^*, different from their free electron mass given by:

$$\frac{1}{m^*} = \frac{1}{\hbar^2}\frac{\partial^2 E}{\partial k^2}$$

This means that that the effective mass is inversely proportional to the second derivative of the *E-k* relationship. For *k* values equal or close to the Γ point the electrons have a well defined and constant mass, though not necessarily the free

electron mass, as the *E-k* relationship is parabolic in this region. Away from the zone centre where the bands are no longer parabolic, m^* varies with k and hence the electrons at those points respond to perturbations as if they possess a different mass, which could possibly be negative or even infinite. Bands can generally be considered parabolic for energies up to about 15 meV above the conduction band edge.

The relationship also applies for holes. Looking at the bandstructure diagrams for semiconductors, we can see that it is possible for two varieties of hole to exist, each possessing a different *E-k* relation. For instance in Figure 10, the Γ_8 point has two energy bands passing through it. As the different bands will possess different curvatures it is said that two different holes exist, a *heavy hole* and a *light hole*. The band with the higher curvature corresponds to the light hole. There is a third hole band in this case with a lower energy passing through the Γ_7 point. This is the *split-off hole* band and is lowered in energy as a result of the spin-orbit interaction of the electrons in this band.

2.5. Impurities in Semiconductors

Two major classes of impurities exist. Those which only slightly perturb the lattice are known as *shallow* impurities because the impurity state is weakly bound and its wavefunction can be constructed from a combination of conduction and valence band Bloch wavefunctions. A shallow impurity can either be a donor, which can easily donate an electron to the conduction band, or an acceptor, which can accept an electron from (or promote a hole into) the valence band. Binding energies can be calculated by using the effective mass approximation.

Conversely *deep* impurities produce a large perturbation to the lattice. They have large binding energies and typically are associated with electronic states in the middle of the energy gap. Deep level impurities can be caused by defects in the lattice, such as vacancies or dislocations, or by certain impurities such as transition metals.

One of the main attractions of semiconductors as materials is that other elements can be deliberately introduced into the lattice to change the electrical and optical properties. This process is called doping. Often the dopant is picked so as to have a valency one more or less than the atom it replaces, but it could be any atom depending on the effect required. Very small concentrations of dopants, even as low as one part in a million, can drastically alter the properties of a material.

2.5.1. Shallow Impurities

Donors

Imagine we have a lattice constructed from a particular unit cell and the bands are filled such that the material behaves as a semiconductor with energy gap, E_g. If an atom in one of the unit cells is replaced with a new atom that has a valency of one more than the original atom, then there is an extra electron in the lattice and this electron cannot fit into the same energy band as this band has already been completely filled. It must go into the next highest energy band, which is the conduction band. This replacement atom is called a *donor*, as it donates an electron to the conduction band.

However, the electron will not be completely free to move around in the conduction band until it has overcome the Coulomb attraction of the donor site (which will have unit positive charge as the atom has one proton more than the atom it replaced). The

electron is trapped in a state slightly below the conduction band edge and orbits the donor site in a system which can be considered analogous to the Bohr model of the hydrogen atom. The atom possesses one more electron than can fit into the lattice bonds and this is then bound to the site at an average distance r_d. This state is shown in Figure 14 for phosphorus replacing a germanium atom.

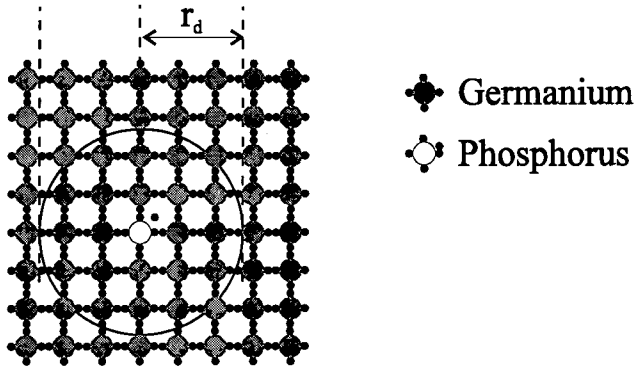

Figure 14: Phosphorus donor atom in germanium

Acceptors

It is also possible for the replacement atom to originate from a group with a valency of one less than the target site atom. There is now one electron less than the number required by the lattice to completely fill the valence band. Electrons can now move through the lattice by occupying the empty state associated with the acceptor. It can equally be said that the empty state has moved into the site previously occupied by the electron. This empty state is a *hole* and the atom which donates a hole to the valence band is an *acceptor*. Figure 15 shows the outer (valence) electrons of germanium with a boron acceptor.

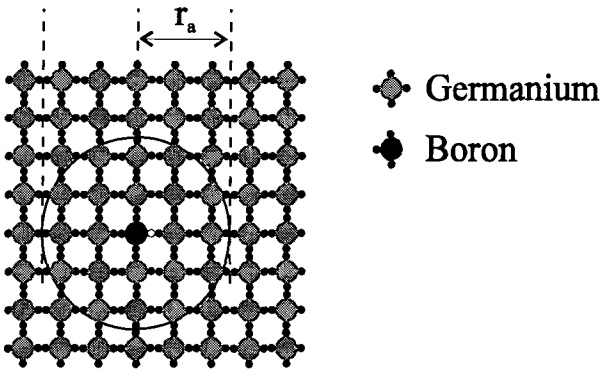

Figure 15: Boron acceptor atom in germanium

Binding Energies for Donors and Acceptors

As mentioned previously, these systems can be considered analogous to the Bohr model of the hydrogen atom, and this leads to the following expressions[14] for the binding energy of the electron or hole:

$$E_{binding} = \frac{e^4 m^*}{2\left(4\pi\varepsilon_{rel}\varepsilon_0\hbar\right)^2} = \frac{m^*}{m_e}\frac{1}{\varepsilon_{rel}^2}\left(13.6\ eV\right)$$

and radius of orbit:

$$r = \frac{4\pi\varepsilon_{rel}\varepsilon_0\hbar^2}{m_e e^2} = \frac{m_e}{m^*}\varepsilon_{rel}\left(0.53\text{Å}\right)$$

Here m^* is the effective mass of the electron or hole in the lattice and ε_{rel} is the relative permittivity of the semiconductor medium which will be of order 10. This means the binding energy of the ground state of an electron bound to a single positive charge will be of order 10^{-2} eV and the radius of order 100 Å. Note that excited states are allowed and the n^{th} of these states will have a binding energy of $(E_{binding})/n^2$ (see Figure 16) as for the Bohr Model:

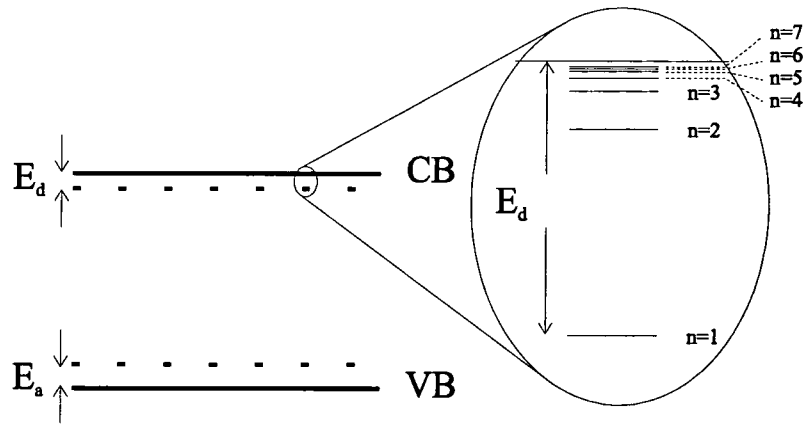

Figure 16: Diagram of donor and acceptor energies

Central Cell Correction

It is apparent from the equations that all donor impurities in any given semiconductor are predicted to have exactly the same binding energies since this depends only on the relative permittivity and effective mass of an electron (similarly for all types of acceptors). This is not the case though and different impurity atoms give varying binding energies (see Table 2.2. The effective masses are taken from published values[15]).

Impurity and type	$E_{binding}$ (meV)	
Donors	**Si**	**Ge**
Bohr Model	19 (using $\varepsilon_{rel} = 11.7$, $m^*_e=0.19m_e$)	4.3 (using $\varepsilon_{rel}=15.8$, $m^*_e=0.08m_e$)
P	45	12.0
As	49	12.7
Sb	39	9.6
Acceptors		
Bohr Model	52 (using $\varepsilon_{rel} = 11.7$, $m^*_{hh}=0.53m_e$)	20 (using $\varepsilon_{rel}=15.8$, $m^*_{hh}=0.36m_e$)
B	45	10.4
Al	57	10.2
Ga	65	10.8
In	157	11.2

Table 2.2: Binding energies of some common impurities in silicon and germanuim

The differences arise because the electron or hole will be sensitive to its local conditions which are assumed to be identical for all impurities in the hydrogenic model. In reality though different impurities will affect the lattice by causing distortions in lattice by the inclusion of an atom with a different size, by the effects of the difference in the shielding provided by inner core electrons of the impurity and by effects of the host lattice itself. The more the electron or hole state is localised around the impurity site, the larger the effect of the different atom.

These terms are grouped together into the *central cell correction*, which alters the simple hydrogenic theory of shallow impurities to give varying binding energies. The correction is usually positive, which indicates extra binding, but can sometimes

be negative.

2.5.2. Deep Levels

The effective mass theory above only holds for shallow donors and acceptors. If an impurity perturbs the lattice to a large degree, then the hydrogenic model breaks down and a highly localised state exists, said to be a *deep level* impurity. An example of such an impurity would be the insertion of a transition metal into a lattice, or an atomic vacancy where the material has been grown badly and the lattice is imperfect. These impurities can act as donors or acceptors but have binding energies of order 100 meV. These states can give the material a very low conductivity because electrons and holes becoming trapped at these sites have very little chance of being thermally excited back to the conduction or valence bands.

2.6. Optical Transitions in Semiconductors

As mentioned in section 2.4.2 it is possible for carriers to be excited across the band gap by either thermal or optical excitation. Doping the material with impurities creates new energy states in the band gap and these alter the electrical and optical properties of the material. This thesis is concerned with the study and analysis of the optical response of various semiconductors, through the use of absorption and photoluminescence.

2.6.1. Optical Absorption

An electromagnetic (EM) wave consists of oscillating electric and magnetic fields perpendicular to each other and the direction of the Poynting vector (direction of energy flow). When an EM wave interacts with a material, absorption of the photon can occur as the electric field component will perturb electrons in the system. The electric dipole operator will induce a transition between two states if the initial and final states of the electron and the energy of the wave are suitable. We ignore effects of the magnetic field and higher order terms.

Consider a semiconductor that has a band gap E_g and the two cases for a photon of energy hυ incident on it. The photon can be absorbed by an electron if its energy is such that it allows the electron jump from a lower (filled) state to a higher empty state. Hence, two possibilities exist as shown in Figure 17.

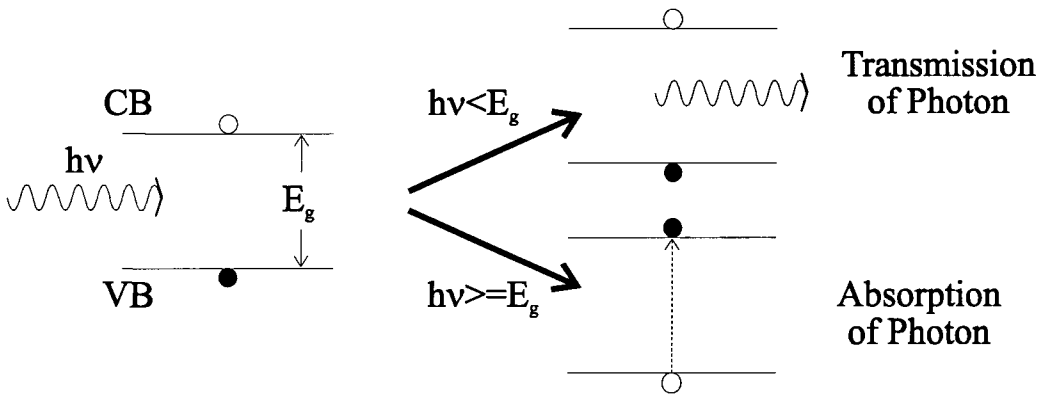

Figure 17: Absorption process in a semiconductor

If the energy of the photon is smaller than the energy gap of the semiconductor then the photon cannot be absorbed since there are no states in the band gap for the electron to move into. However if the photon energy matches the band gap then the photons energy is used to promote the electron from the lower to upper state, as long as that upper state is not already occupied by an electron. The absorption coefficient,

$\alpha(\omega)$, can be calculated from Fermi's Golden Rule, and for a simple two band semiconductor this gives:

$$\alpha(\omega) = \frac{1}{2\pi} \frac{|e|^2 \left| -i\hbar \int \psi_c^*(\underline{r}) \hat{e}.\underline{\nabla} \psi_v(\underline{r}) dr \right|^2}{m_0^2 \varepsilon_0 \omega c n_r \hbar^3} (2\mu)^{3/2} \left(\hbar\omega - E_g\right)^{1/2} \left(f_v - f_c\right)$$

where μ is the reduced mass of the electron in the conduction and valence bands, the integral term gives the overlap of the initial and final states under the electric dipole operator and f_c and f_v are the electron distribution functions for the conduction and valence bands respectively. Under normal circumstances the population of the valence band is higher than the population of the conduction band and the absorption coefficient is positive. In semiconductor lasers however, the population inversion that exists means f_c is greater than f_v and the absorption coefficient is negative, corresponding to a gain in the energy of the electromagnetic wave.

Note that the bands in Figure 17 are shown as in the Narrow Band Model at a single energy. This is not the case in a real semiconductor where the energy density of states at an energy E increases as $E^{1/2}$ and this is reflected in the $(\hbar\omega - E_g)^{1/2}$ term. This means the absorption in a semiconductor should follow a straight line of slope ½ on a log-log plot of absorption coefficient against energy.

Absorption is measured experimentally from the amount of light transmitted. If a large quantity of light is transmitted through a material then the absorption must be small and correspondingly a small transmittance indicates a large absorbance.

Absorption, $\alpha(E)$ is measured on a logarithmic scale as:

$$\alpha(E) = -\ln(\tau(E))$$

where τ is the transmittance and is defined using Φ_t, the transmitted flux, and Φ_0, the incident flux as:

$$\tau = \frac{\Phi_t(E)}{\Phi_0(E)}$$

2.6.2. Photoluminescence

Photoluminescence differs from absorption in that the light incident on the semiconductor is constant in energy. The energy of the photons is chosen by such that it is larger than the band gap of the semiconductor and ideally the semiconductor will be very strongly absorbing at that particular energy so electrons will be excited from the valence band to somewhere above the conduction band edge. The absorption of the photon creates an electron and a hole in the semiconductor. Within a few picoseconds, thermalisation of the electrons will occur where the electrons will rapidly drop to the bottom of the conduction band and hole will rise to the top of the valence band. Eventually the electron will recombine will the hole emitting a photon with an energy equal to the energy difference between the two states occupied by the electron and hole when the recombination took place.

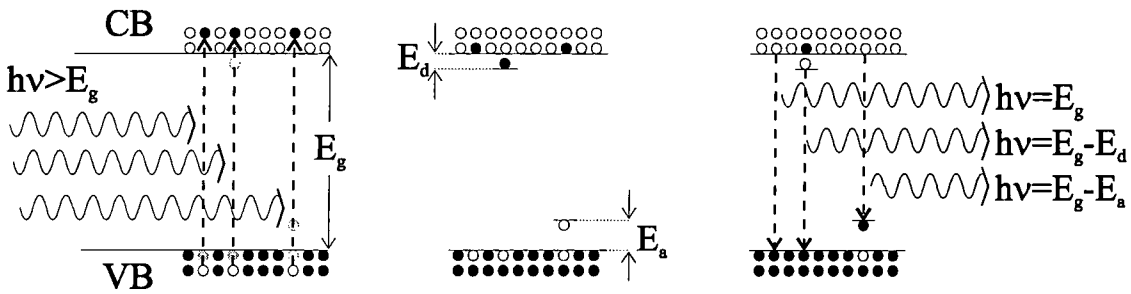

Figure 18: Some photoluminescence process in a semiconductor

It is also possible to detect states in the energy gap created either deliberately or accidentally by defects or impurities. Once the electron and hole have reached the

band edges they may proceed into the band gap if a suitable empty state is present and a suitable mechanism allows them to loose energy. The electron and hole lose the energy required by the emission of phonons or by Auger-type processes. Recombination from these states will produce photons of a lower energy and the difference in energy between these photons and the band edge photons is the related to the position in the band gap of these states.

Other possible emission processes occur and can be explained:

Excitons

An exciton is a bound state of an electron and a hole. Denoted by the symbol X, they normally only form in semiconductors at low temperatures which are relatively free of defects. They can be thought of as a variant of a hydrogen atom with the hole replacing the positive nucleus. The binding energy of such a system is given as:

$$E_{binding} = \frac{\mu}{\varepsilon_{rel}^2}(13.6eV)$$

where μ is the reduced mass of the system given by:

$$\frac{1}{\mu} = \frac{1}{m_e^*} + \frac{1}{m_h^*}$$

This means an exciton will have a binding energy less than a donor or acceptor system as the mass of both particles involved is approximately of order m^*_e, whereas a donor or acceptor has one near infinite mass.

Excitons themselves can be localised at any centre which perturbs the lattice and gives a localised change to the crystal potential, or to a charge centre. For instance excitons can bind to shallow impurities. An exciton bound to a neutral donor is called a *donor bound exciton*, denoted by D^0X and an exciton bound to a neutral

acceptor is called an *acceptor bound exciton*, denoted A^0X. Because the binding energy of the exciton is so small perturbation to the crystal lattice caused by deep level impurities overcome the coulombic attraction that binds the electron and holes and the exciton is dissociated. This is why excitonic recombination is generally only seen in good quality semiconductors at low temperatures.

Haynes' Rule[16] tells us that the binding energy of an exciton to an impurity will depend on the binding energy of an electron or hole to that impurity, which helps us identify impurities in materials as excitonic recombination at impurity sites gives a characteristic binding energy of the exciton.

It is also possible to get (D^+X) and (A^-X) bound excitons, where the binding centre is an ionised donor or acceptor.

Free to Bound Transitions

Here free particle recombines with a particle bound at an impurity centre. Either a free electron in the conduction band recombines with a hole bound to an acceptor, or a free hole in the valence band recombines with an electron bound at a donor.

Donor-Acceptor Pair Transitions (or Bound to Bound Transitions)

If a donor is located near an acceptor in the lattice, it is clearly possible for the electron of the donor to drop in to the hole created by the acceptor. This is known as a *Donor-Acceptor Pair* transition.

The photons emitted from the sample need to be analysed, usually using a monochromator and light sensitive detector. A plot showing a spectrum of the emitted light can be generated. This leads to information about the nature of

impurities in the lattice.

2.6.3. Emission Line Shapes

Consider a quantum system with two states which is initially in a state with energy E_a. It can change to the other state, with a lower energy E_b, emitting a photon so conservation of energy is satisfied, after an average time τ.

Any emission process governed by the normal time dependant probability of a photon being emitted can be shown[17] to emit radiation with a Lorentzian intensity distribution $L(\omega)$::

$$L(\omega) = \frac{\Gamma/(4\hbar^2)}{(\omega - \omega_c)^2 + \Gamma/(4\hbar^2)}$$

where $\omega_c = \frac{E_b - E_a}{\hbar}$ and $\Gamma = \frac{\hbar}{\tau}$. This is known as homogeneous broadening. It is intrinsic to the emission process, and is the sharpest line that could be measured by a "perfect" instrument.

However, perturbations external to the recombination process such as impurities or crystal fluctuations, give another form of broadening which produces a Gaussian intensity distribution $G(\omega)$:

$$G(\omega) = \exp\left(-\alpha(\omega - \omega_c)^2\right)$$

This is known as inhomogeneous broadening. It is found that usually the Gaussian distribution is the major broadening process, and most lines are therefore Gaussian in shape. Emission processes which involve bound particles are broader than those which involve free particles, as they are more affected by the sources of binding. Conversely, free excitons have very narrow line widths and any observed broadening

can be used as a measure of defects in the crystal.

The two types of broadening are shown in Figure 19.

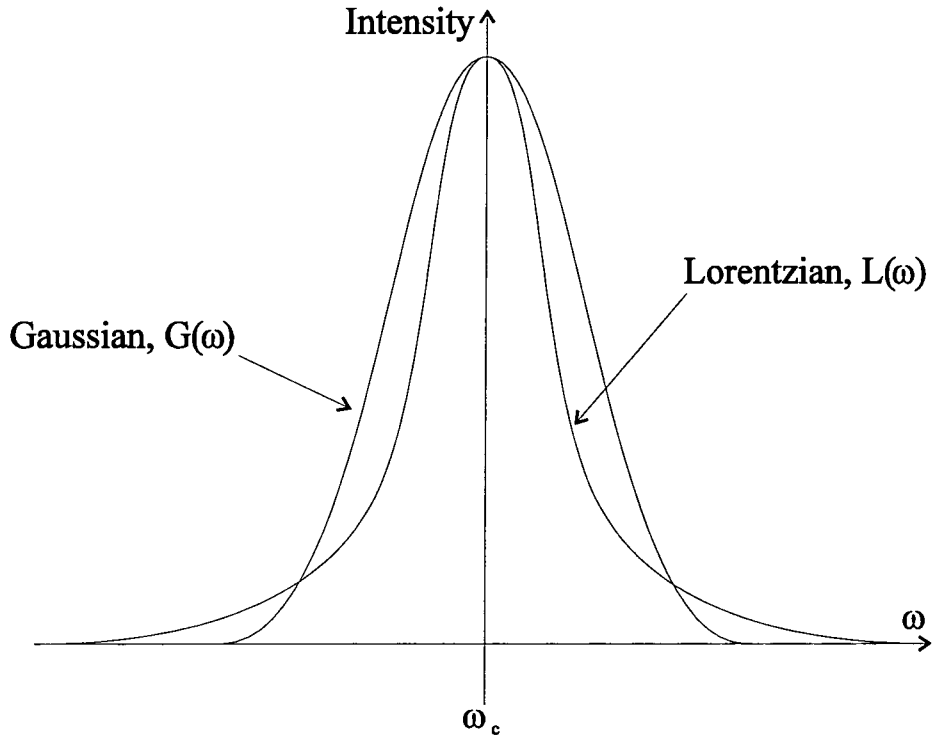

Figure 19: Comparison of Lorentzian and Gaussian line shapes

2.7. Phonons

Phonons are the quantum units of the normal modes of vibration of a crystal lattice and are akin to a sound wave passing through the material. That is, the vibrations of the atoms in the lattice can be thought of in terms of a unit of vibration passing from one atom to the next. A phonon carries momentum and energy with it.

In the zinc blende crystal structure, a diatomic system, (shown in Figure 1) there are two different atoms in the atomic basis on a face centred cubic unit cell. The dispersion relationship for a phonon in a diatomic chain of atoms of masses M_1 and M_2 :with a restoring force constant of C is[18]:

$$M_1 M_2 \omega^4 - 2C(M_1 + M_2)\omega^2 + 2C^2(1 - \cos(Ka)) = 0$$

This can be solved to give the phonon dispersion curve shown in Figure 20:

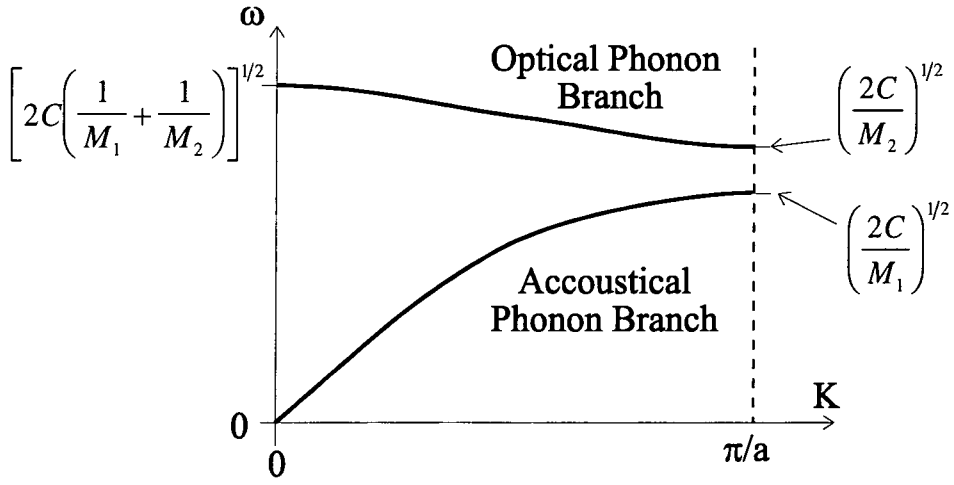

Figure 20: Phonon dispersion relationship for a diatomic lattice

The two variants of phonons which arise are optical and acoustic phonons. Acoustic phonons have the two atoms in the unit cell vibrating in phase and optical phonons have the two atoms in the unit cell vibrating out of phase. For both phonon types, the atoms can either vibrate in the direction of motion or perpendicular to it, giving rise to *Longitudinal Optical* (LO), *Transverse Optical* (TO), *Transverse Acoustic* (TA) and *Longitudinal Acoustic* (LA) Phonons. These have different energy- wavevector relations in real materials.

Phonons can be absorbed or emitted by the lattice and can take part in optical processes. Phonons play a vital part in optical processes in indirect semiconductors as there must be a transfer of momentum when the electron falls from the bottom of the conduction band to the top of the valence band.

The *Huang - Rees* parameter, S, sets the strength of the coupling between the electrons and the lattice. One can also say it is the average number of phonons emitted to allow the system to reach the lowest energy state after either the

absorption or emission of a photon. To see this, consider the Franck-Condon[19] approximation as shown in Figure 21. The absorption of a photon of energy E_{abs} excites the system from the ground state A to the excited state of a different configuration B. By emitting phonons the excited state rapidly relaxes to the excited configuration's ground state C. Then the system emits a photon with energy E_{em} and returns to the original configuration at point D where emission of more phonons allows the state to return to the original position A.

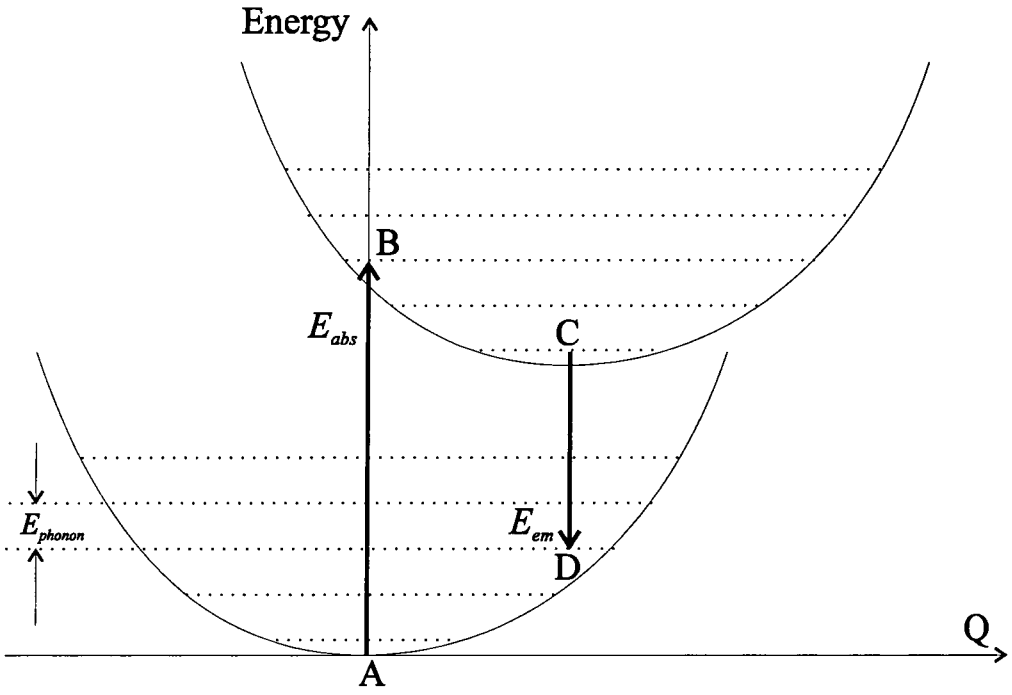

Figure 21: Configuration co-ordinate diagram for Franck - Condon approximation

By consideration of the energies involved it is clear that:

$$E_{abs} = E_{em} + 2E_{phonon}S$$

where S is the Huang - Rees parameter, the average number of phonons emitted by an excited state in returning to its ground state in the same configuration.

3. EXPERIMENTAL

This chapter gives the details of the of the equipment used and the setting up procedures involved in undertaking the experiments described in the following four chapters. Several pieces of experimental apparatus were interfaced to a computer which had been programmed so it could automatically collect data. Calibrations had to be made so as to ensure accurate measurements were being taken.

3.1. Apparatus

The techniques described in this thesis probe the energy levels of the system being studied by using electromagnetic radiation. In order that the spectrum either emitted from or transmitted through the material can be analysed, it is necessary to first disperse the various energy components of the light so that the separate energies can be distinguished. The apparatus to do this is a monochromator. A photosensitive detector can be used to quantify the amount of light in the particular spectral region selected by the monochromator. Both a diode array and a photomultiplier tube were used in these experiments.

Often extra information can be obtained by varying the temperature of the sample as this will alter the population of the energy levels in the material. The samples are mounted in a cryostat with sapphire windows to allow light access to the sample to facilitate spectral measurements at varying temperatures.

3.1.1. Monochromator

Monochromators are an essential part of the experiments covered here. They are designed such that light entering the system is split by a dispersing element and the energy range to be studied can be selected accordingly. We used a Bentham 0.25 m monochromator and the layout is shown in Figure 22.

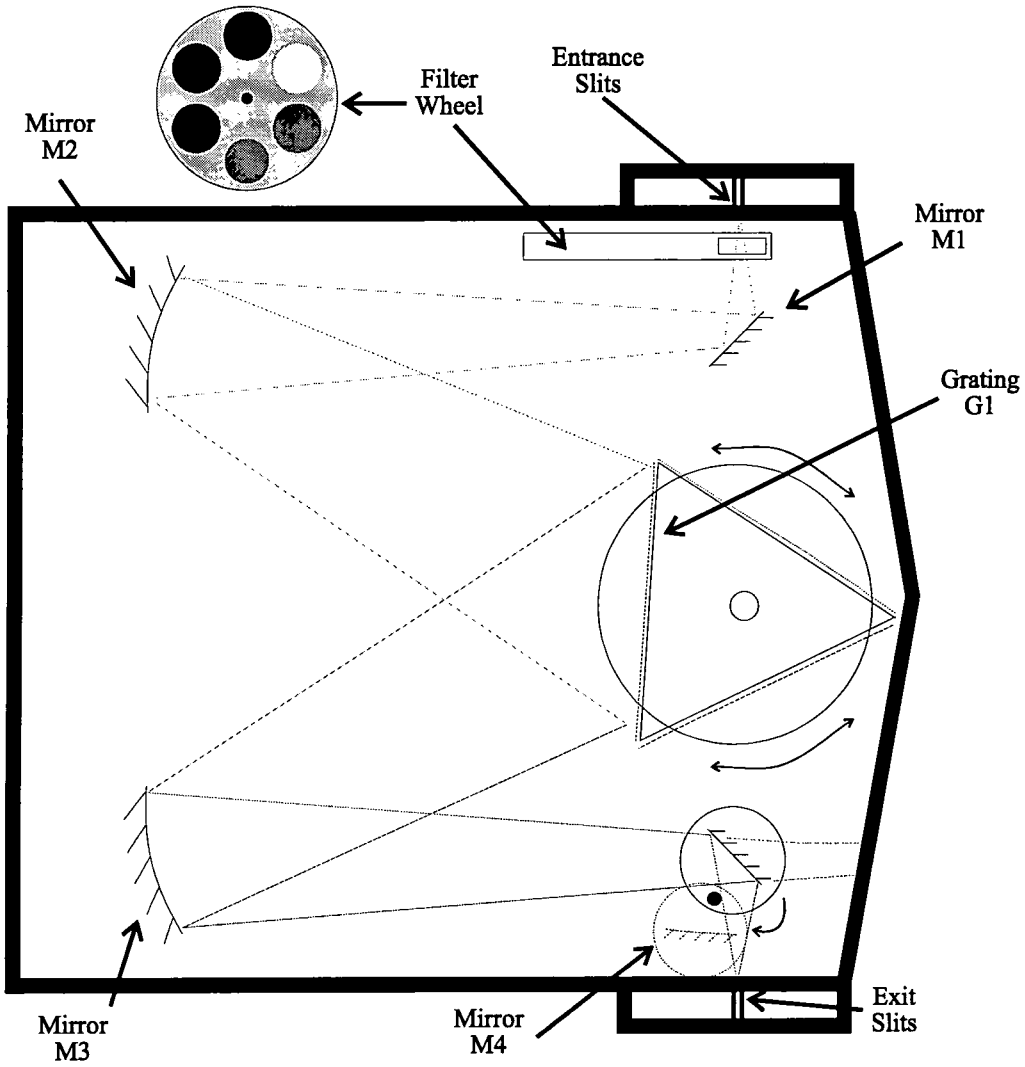

Figure 22: The Bentham monochromator

Having passed through the entrance slit and suitable filter the light is directed by the planar mirror M1 onto the curved mirror M2, which produces even illumination across the grating, G1. The light reflected off the grating is subject to constructive and destructive interference, subject to the equation[20]:

$$d(\sin(i) - \sin(\vartheta)) = m\lambda$$

where d is the spacing of the diffraction grating, i is the angle the incoming beam makes with the normal to the grating, θ is the angle the outgoing beam makes with the normal to the grating and m is the diffraction order.

The mirror M3 then refocuses the divergent light from the grating onto M4 which redirects the beam out of the exit slit. Alternatively mirror M4 can be swung out of the way to allow the light to be focused on to a diode array detection system.

The filter wheel was designed to allow the removal of any higher order diffraction from the signal and consisted of six slots each capable of holding one filter. One of the slots was left empty and one was filled with a metal blank for use as a shutter. Two of the four remaining slots were filled by OS400 and OS700 high band pass filters.

Three gratings were available:

Grating	Lines/mm	Dispersion (nm/mm)	Blaze Wavelength (nm)
1	1200	2.7	550
2	400	8.1	850
3	150	21.6	800

Table 3.1: Gratings present in monochromator

3.1.2. Diode Array

The majority of the measurements presented here were taken using an EG&G Diode Array model 1453A under the control of a Model 1471A Interface Unit which communicated with a computer to set parameters and send data.

The diode array was a silicon based detector which consists of 1024 pixels, each of which could measure the number of photons incident on it. A spectrum can be taken if the dispersion of the grating is known. This was be measured by using spectral bulbs which emit light at known wavelengths.

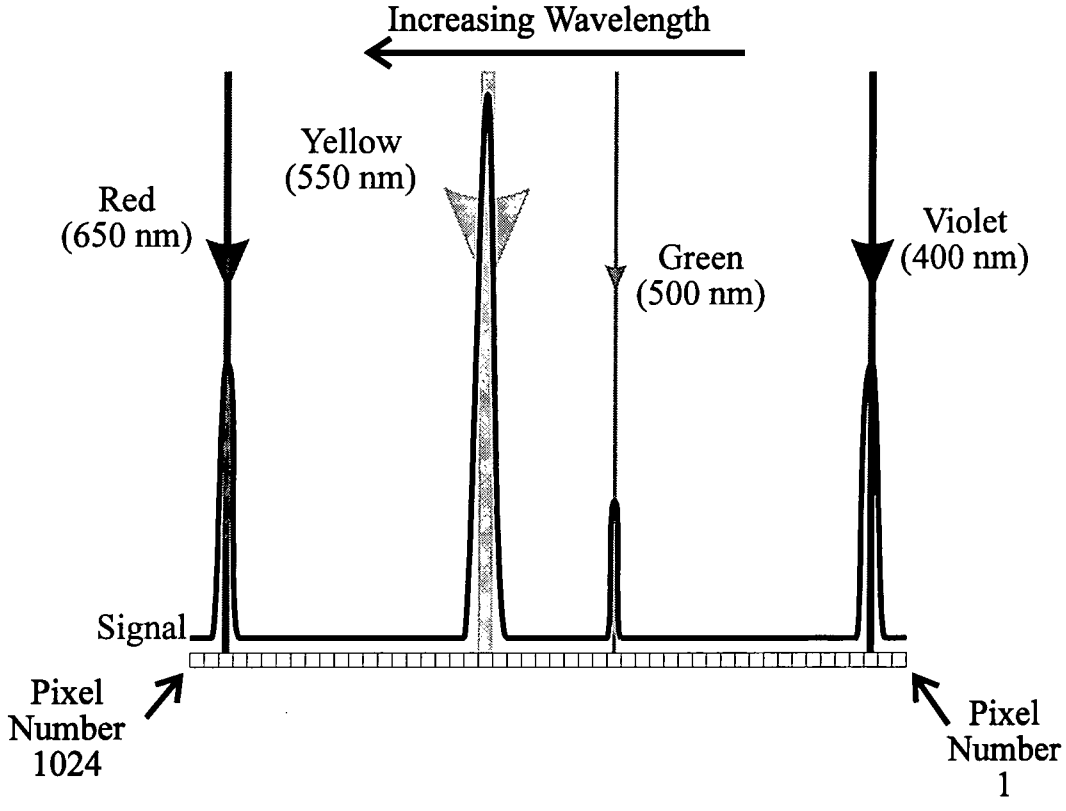

Figure 23: Spectral dispersion across the diode array

Figure 23 shows the expected signal from an imaginary source of light emitting equal numbers of photons at 400 nm and 650 nm, twice as many at 550 nm and half as many at 500 nm. The signal is proportional to the number of photons incident on a pixel multiplied by the efficiency of the silicon photodiodes at that wavelength. The diode array has a count range from 0 to 32,767.

The diode array has a built in Peltier cooling system which allowed the temperature of the array to dropped to about 0 °C under a dry nitrogen atmosphere and -25 °C if a supply of cooling water was provided. This was necessary as the dark (thermally excited) counting rate was high enough to cause the signal to reach the maximum

level before sufficient signal counts could be recorded to give a reasonable spectrum. With cooling, an exposure time of 600 seconds could be attained, compared to 10 seconds without.

3.1.3. Photomultiplier Tube

For the absorption measurements discussed later, a different experimental layout was employed and a photomultiplier tube (PMT) was used as the detection system. This was a Hamamatsu R3896 model, and was powered from a Brandenburg High Voltage power supply.

Light entering the photomultiplier strikes a suitable compound and photoelectric effect causes electrons to be ejected from the material. These primary electrons are swept into an electron multiplier by the high voltage resulting in a measurable current pulse.

When using the PMT it was necessary to make use of an optical chopper and Lock-In amplifier because of the level of background noise that the detector was measuring. Due to the nature of the experimental layout the PMT was particularly prone to stray room light affecting the measurement.

A lock-in amplifier looks for oscillations in the input signal of a certain frequency. By using the chopper to modulate the light incident on the sample and feeding the frequency of that modulation into the lock-in amplifier, information originating from the sample can be discriminated from the background noise. The lock-in output, which was proportional to the number of photons, was fed into a digital voltmeter interfaced to the computer so readings could be taken automatically at any wavelength.

3.1.4. Cryostat

Two different cryostats were used for the work presented. An Oxford Instruments Liquid Nitrogen Gas Transfer cryostat, in which the sample is mounted on the end of a long thin finger. The space surrounding the sample is filled with a dry gas, either nitrogen or helium. The outer wall of this chamber is cooled by a supply of liquid nitrogen whilst a resistive heater can used to increase its temperature. The gas cools the sample by transferring heat from the finger and sample to the wall. By varying the supply of coolant to the cold wall and the current passing through the heater, the equilibrium temperature of the system can be altered from 77K to about 350K.

For reaching even lower temperatures, a Helium Refrigerator cryostat was used where the sample is mounted on a cold finger attached to a helium refrigerator which can cool the sample to 8K. A resistive heater can provide a temperature range up to room temperature. The space surrounding the sample is completely evacuated to remove gases which may solidify on the sample surface when cryo-pumping occurs.

3.2. Computer Interfacing

The equipment discussed above was all under the control of a standard IBM PC compatible with an additional I/0 card to give the computer IEEE capabilities.

Control programs were written under Windows 3.1. using Turbo Pascal for Windows 1.5 (TPW 1.5) which allowed a multitasking approach to be used. However, many of the difficulties encountered during development were as a result of the stricter programming controls enforced by the Windows system.

Originally a 'master control' program was envisaged which would take a request from the user to take a spectrum of a particular size and resolution. The program

would set the monochromator to the correct wavelength and filter, take data from the diode array or lock-in amplifier then repeat the procedure until the requested spectrum had been obtained. A graph showing the spectrum would be displayed to the user with options available to save the data to the hard disc of the computer or print a copy of the graph to paper.

This program became unmanageable towards the end of its development (with a compiled size of over 7100 lines) and the functions required had to split into the more manageable programs shown below. Each program relies on the **"TWindow"** TPW 1.5 object type, which itself consists of some 2000 lines which provide the standard functions of a basic window such as minimise, maximise, resize, automatic redrawing and closure.

Device Controlled	Controller Program Name	Size of Program		Communications Protocol Used:
		Bytes	Complied Lines	
EG&G Diode Array	EGGWIND.EXE	178K	5370	IEEE
Bentham Monochromator	BENTWIND.EXE	142K	3100	RS-232
Keithley Digital Voltmeter	DMMWIND.EXE	114K	2290	IEEE
EuroTherm 900 Temperature Sensor and Controller	E900WIND.EXE	113K	2410	RS-232

Table 3.2: The equipment control programs

Generally, the data was taken from the diode array control program to a data analysis package such as EasyPlot, Excel or SigmaPlot for display and storage on the hard disk.

Each program had the ability to communicate with the others though so it was possible to program one device controller to vary an experimental parameter under the command of another device.

The following brief summaries describe each programs functions and controlled parameters.

The EG&G Diode Array program controlled the acquisition of data from the diode array (incorporating an ability to allow for the effect of room lights), included a system for optimising the alignment of the optical components in the experiment and let the user set the detector temperature and pixel exposure time.

The Bentham Monochromator control program allowed a wavelength to be selected for light either leaving the exit slit or falling on to the diode array from any of the three installed gratings with any of the different filters inserted into the beam.

The Eurotherm 900 Temperature Controller program provided the ability to set and read the cryostat temperature from the computer.

The Keithley Voltmeter program simply allowed the voltage being read by the meter to be recorded by the PC.

3.3. Calibration

The largest problem with the system developed was that of calibration. Initially, a system which used built in calibrations was envisaged, allowing data to be taken without routinely having to make a calibrating measurement. It was apparent though that the simple first order approximation for a linear dispersion along the diode array was incorrect and as such could not be relied upon to give highly accurate wavelength information. More problematic though was the effect of moving the grating so that the diode array could take spectra by sampling portions which were then to be combined to give a larger wavelength coverage. The efficiency of

throughput of light was affected by the particular angle at which the grating was set and it proved unreasonable to measure the effect for all possibilities.

The solution was to calibrate each setting as and when the system was to be used with that setting. A selection of vapour bulbs was available, each with certain emission lines that could be measured and used as calibration points for the spectrometer in that configuration.

Intensity calibration could easily be corrected for by using a 12 Volt 100 Watt light bulb powered by a car battery which was known to have a filament temperature of 3400 K. Knowing the temperature made it possible to predict the black body spectrum I(λ,T)of the bulb using[21]:

$$I(\lambda,T)=\frac{8\pi hc}{\lambda^5}\frac{1}{\exp\left(\frac{hc}{\lambda kT}\right)-1}$$

where T is the bulb temperature, k is Boltzmann's constant, c is the speed of light and $\hbar$ is Planck's Constant. Knowing I(λ,T) allowed the data to be calibrated for intensity so differences in the spectral efficiency of the detector, monochromator and external optics could be allowed for.

4. OPTICAL PROPERTIES OF ULTRA THIN 50 NM GaAs MEMBRANES

4.1. Summary

Ultra thin free standing films of single crystal GaAs have been fabricated by selective etching of epitaxial layers grown by Molecular Beam Epitaxy. The resulting membranes are 50 nm thick. The results of optical absorption measurements are presented. These demonstrate features which are not normally observed in thicker GaAs layers. Higher energy transitions from the valence to conduction band at the L point in the Brillouin zone are observed in the optical absorption spectra of these structures at 2.7 eV. The temperature dependence of this energy gap is measured and compared with previous data.

4.2. Introduction

Ultra thin substrates are of increasing technological interest. There is considerable advantage in using them for fabrication of high speed field effect transistor (FET) devices when using electron beam lithography. The effect of damage from backscattered electrons is greatly reduced as is shown in Figure 24 and this permits much higher resolution to be achieved[22,23]due to the reduction in etch spot size. This allows much smaller and hence faster devices to be designed and manufactured.

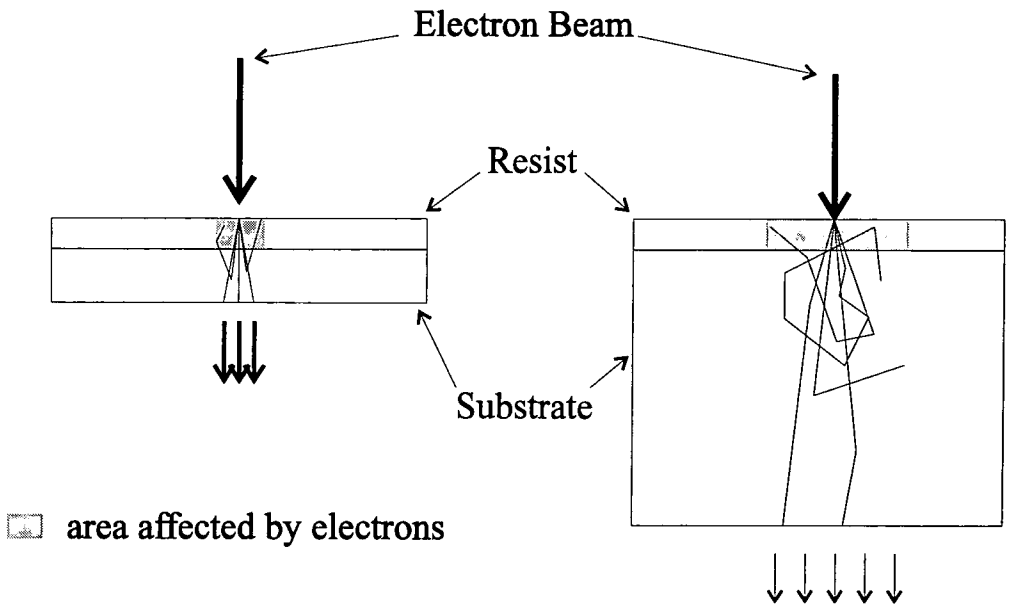

Figure 24: Effect of back-scattered electrons in lowering resolution

It has also been observed that gain can be increased in the high frequency response of Schottky barrier diodes fabricated on GaAs membranes enabling devices to operate in the sub-millimetre wavelength regime. It has been determined through theoretical analysis by Seidal and Crowe that for a 1μm GaAs membrane the series substrate resistance will decrease by 60% at 3 THz[24]. This is accomplished through reducing the current path between the ohmic and Schottky contacts and so lowering the skin-effect contribution to the total resistance.

More recently, it has been shown that ultra-thin layers may be used to produce photonic band gap structures which are active in the optical region of the EM spectrum[25]. These structures consist of a periodic dielectric structure built up from square cross-hatch patterns of material.

Other sub-micron membranes have been produced using an electrochemical anodic oxidation process to etch films after ion implantation. This has produced layers of GaAs 320 nm thick[26]. However, this process requires ion implantation into the GaAs causing damage to the crystalline structure which is detrimental to device performance.

It is also difficult to accurately control the layer thickness by this method.

The membranes used in the work reported here were fabricated by etching epitaxial layers grown by Molecular Beam Epitaxy (MBE) which allows very accurate control of the layer thickness, as this is predetermined during the growth of the layers.

4.3. Sample Fabrication

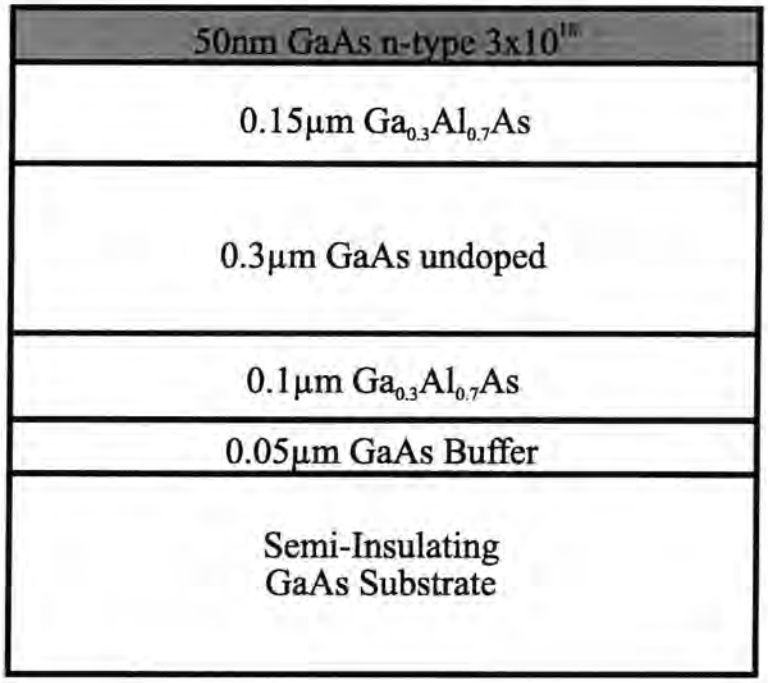

Figure 25: Diagram of the membrane sample

The procedure for fabricating the membranes has been described in detail previously[27,28]. The layers were grown by MBE on a semi-insulating (100) GaAs substrate. The structure, shown in Figure 25, consisted of a GaAs buffer layer, 100 nm AlGaAs, 300 nm GaAs, 150 nm AlGaAs and 50 nm Si doped GaAs (n = 3 x 10^{18} cm^{-3}). The 150 nm AlGaAs layer acted as an etch stop layer. The samples were etched from the substrate leaving the top 50 nm layer. In these samples the etched area was

500 μm x 500 μm.

4.4. Measurements

Optical absorption measurements were performed on the membranes in the wavelength range 350 nm to 550 nm. The light source was a 12 Volt 100 Watt OSRAM halogen bulb powered by a car battery, which was "trickle-charged" by a battery charger to eliminate any reduction in the power provided to the bulb as one run could take 20 minutes. Lenses were used to focus the light from the bulb into a monochromator and again to refocus the light emerging from the exit slits onto the sample which was mounted in a liquid nitrogen gas flow cryostat. A high power lens was used to create a large image of the membrane on a screen with the photomultiplier tube placed behind a small aperture in the screen. This ensured only light passing through the membrane was being measured. The light was modulated using a Bentham chopper placed at the entrance to the monochromator. This layout is shown in Figure 26. The monochromator used a 1200 lines/mm grating giving the measurements a resolution of better than 0.5 nm.

Quartz lenses and cryostat windows were used as normal glass absorbs light at the lower end of the wavelength range being studied.

The signal from the PMT was fed into a trans-impedance amplifier and then to a EG&G model 9501 lock-in using the chopper as a reference signal. To enable spectra to be recorded on a computer, the PC was connected to a Keithley model 195 digital voltmeter which read the output of the lock-in.

The absorption was determined from the ratio of the spectra taken with and without the sample in place. Due to their extremely small size the absorption in the membrane

produced a change of only a few percent in the signal level.

The samples were cooled down and warmed up slowly over a period of several hours to avoid any thermal stress which might rupture the membranes. The measurements were performed at a range of temperatures from 77K to 300K.

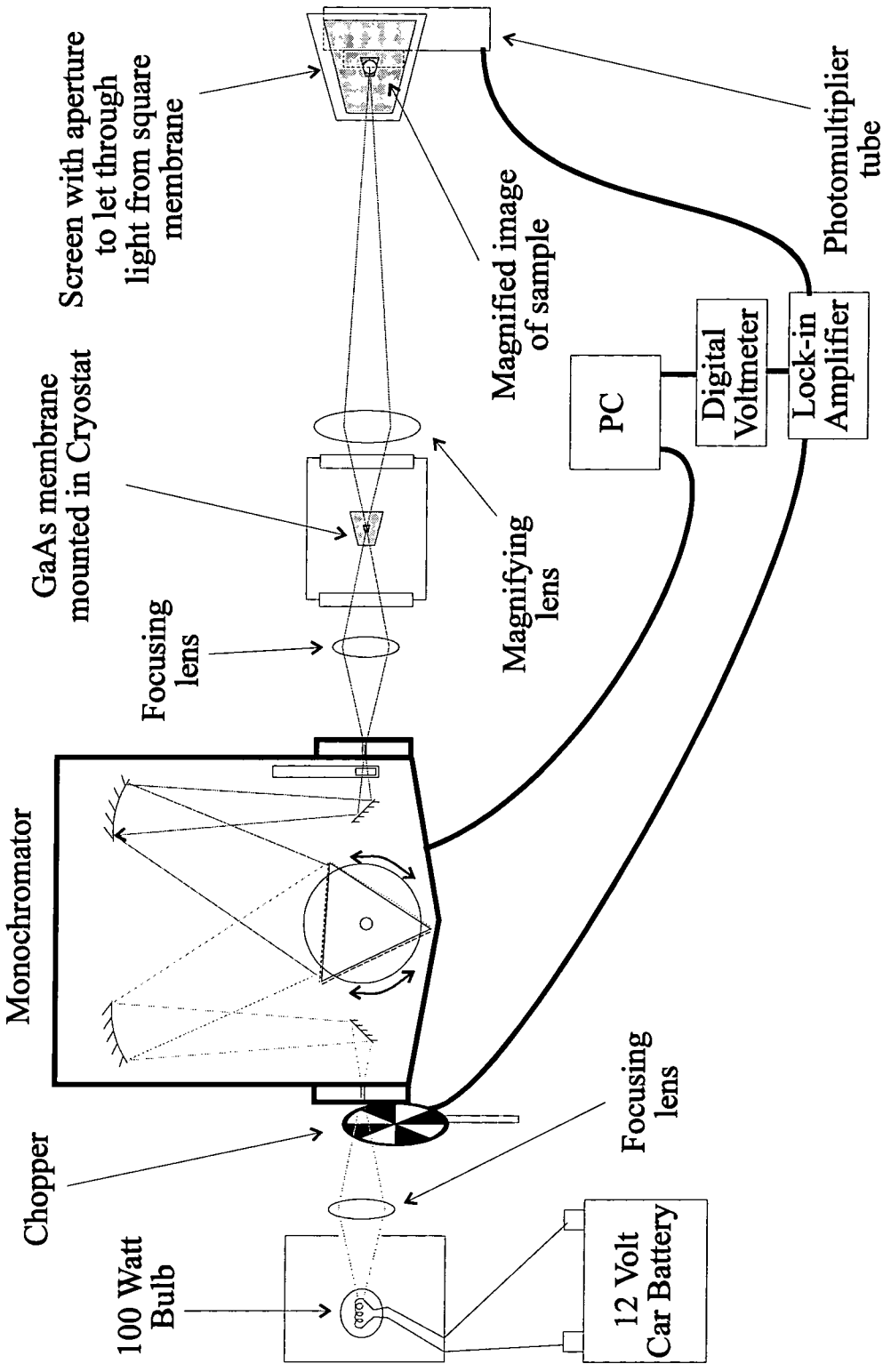

Figure 26: Experimental layout

4.5. Results and Discussions

4.5.1. Γ-Point Transition

Earlier measurements using the same technique gave the absorption spectra of the 50 nm GaAs membranes at 300K and 4K between 1.4 and 1.7 eV as shown in Figure 27.

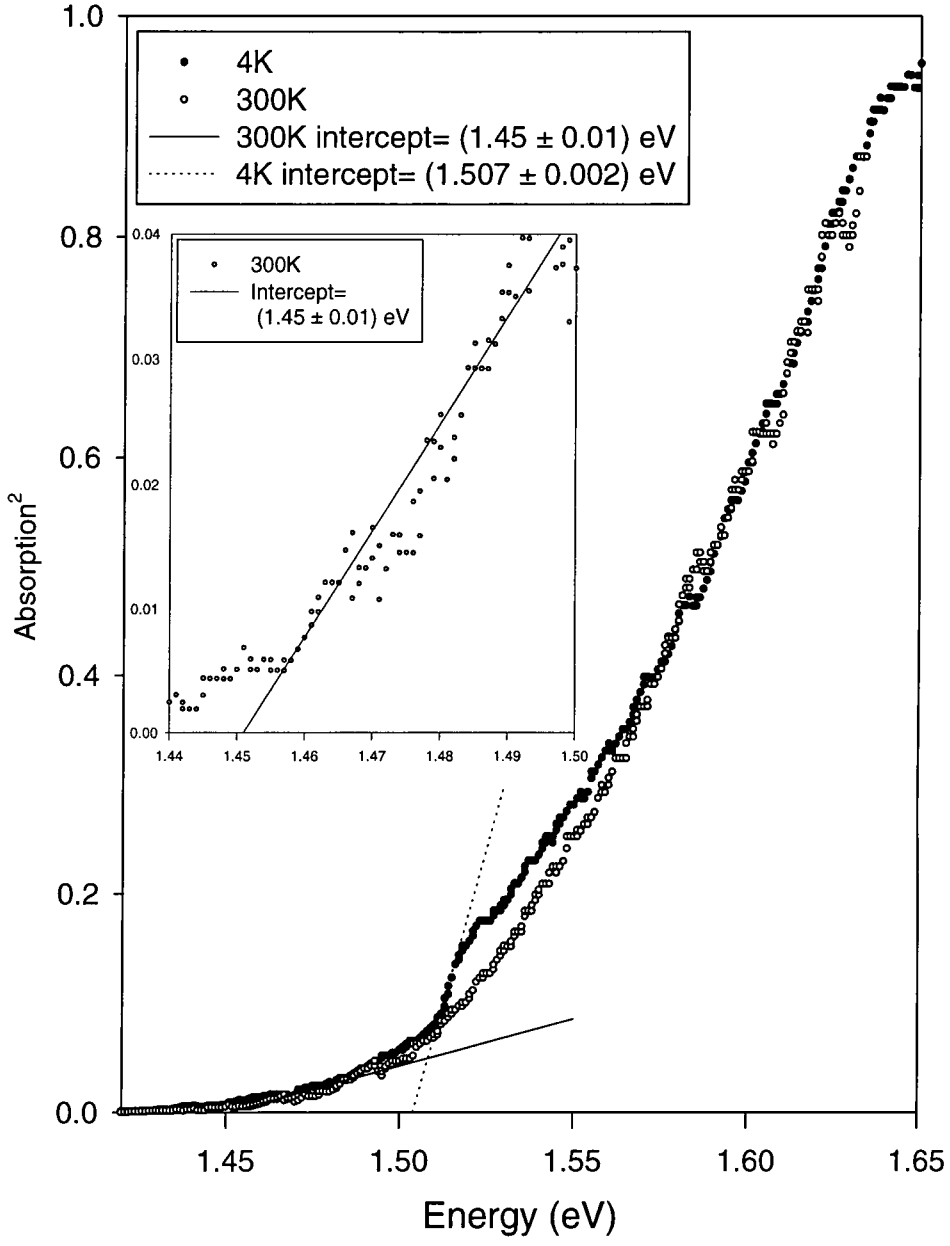

Figure 27: The temperature dependence of absorption due to the Γ-point transition

The absorption edge at 300K is not well defined due to thermal broadening. However, it is estimated that the fundamental absorption edge occurs around (1.45 ± 0.01) eV. In bulk GaAs the room temperature absorption edge occurs at 1.435 eV[29] which is a

difference of 15 meV. This can be explained by the use of the Moss-Burstein (section 4.5.3) and Franz-Kelysh (section 4.5.4) Effects which generate respectively an increase (blue shift) and decrease (red shift) in the value of the band gap measured by optical absorption.

4.5.2. The GaAs surface

It is known that the free surface of GaAs does not cause energy states to arise between the top of the valence band and the lowest conduction band. This is because the atoms making up the surface of the GaAs revert to their atomic configurations, namely gallium with three bonds and arsenic with five. The spare electron from a Gallium atom on the surface fills the empty bond of the neighbouring Arsenic atom. The surface then undergoes a rearrangement to minimize the sum of the bond energies and the strain energy associated with the lattice mismatch between the re-organised surface and the bulk lattice. There is now a dangling bond associated with the surface Arsenic atoms but the related electron states have energies below 0 eV (which is in the valence band) and similarly the empty states provided by gallium atoms generate states in the conduction band so neither of these new electronic states associated with the surface lie in the energy gap of the material. It should be noted that without the rearrangement of the atoms theoretical calculations show that states *would* appear in the band gap.

The presence of an oxygen atom bonded to an arsenic atom in the surface causes the local atoms to return to the bulk ordering system. This "un-rearrangement" increases the total amount of strain experienced by the GaAs surface. It is thought that only a small number of the exterior Arsenic atoms ($\approx$1.5%) need to react with oxygen for the strain increase to precipitate a "disordering phase change" which creates extrinsic

surface defect sites associated with states in the energy gap. This disordering of the surface creates enough defects to cause the Fermi level to become pinned at the semiconductor surface near the middle of the energy gap.

A region at each edge of the membrane will be depleted due to band bending caused by this pinning effect. Electrons near the surface will become trapped at the defect sites on the surface.

If we assume the Fermi level is pinned at 0.6 eV below the conduction band due to surface states[30], we can calculate the thickness of the surface depletion layers at both sides of the membrane from the doping level[31,32].

Using the expression for the depletion region width, W, at the surfaces of the membrane:

$$W = \sqrt{\frac{2\varepsilon_0 \varepsilon_{rel} V_b}{eN_d}}$$

with $V_b = 0.6$ eV, $N_d = 3\times10^{18}$ cm^{-3} and $\varepsilon_{rel} = 13.1$ gives $W = (17 \pm 1)$ nm. Because of the uncertainty in the estimations of V_b and N_d this calculation is only approximate. However, we deduce that there will be a region of about 17 nm at each edge of the membrane which is depleted of carriers.

If the electric field across the depletion layer is considered as being uniform it will have a value of 3.5×10^5 Vcm^{-1} with the peak surface electric field of 7×10^5 Vcm^{-1}.

4.5.3. The Moss-Burstein Effect

The Moss-Burstein shift[33,34,35,36] which occurs in heavily doped semiconductors is due to the filling of states at the bottom of the band minima as the doping level is increased. This filling of phase space leads to transitions from the valence to conduction band

occurring at higher energies and at *k*-vectors away from the zone centre, increasing the onset of absorption by an amount approximately equal to the Fermi energy (see Figure 28), although allowance must also be made for non-parabolicity.

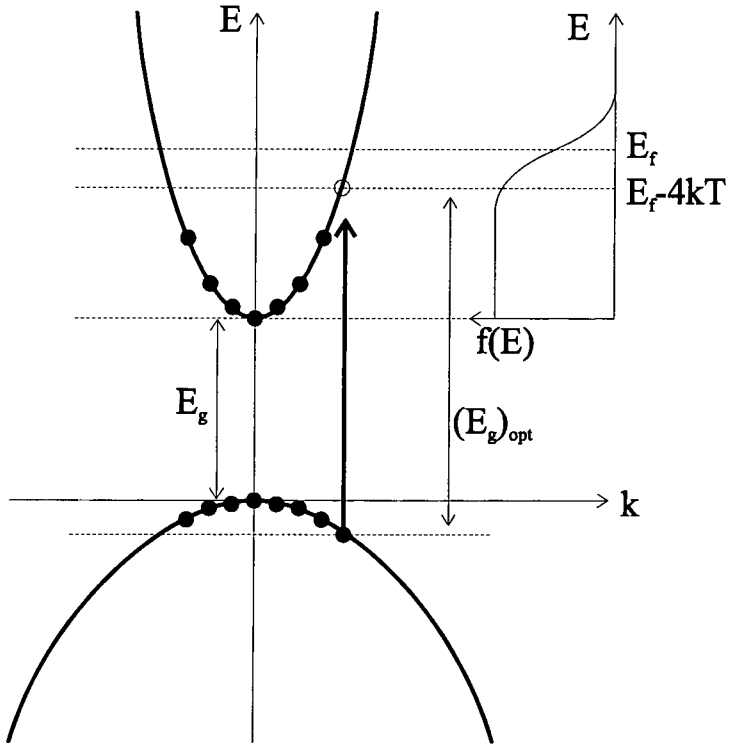

Figure 28: The Moss-Burstein Shift

Raymond et al[37] derive the following equation for the Fermi energy:

$$E_F = (3\pi^2)^{2/3}\left(\frac{\hbar^2}{2m_d^*}\right)n^{2/3}$$

where m_d^* being the effective mass of the electron at the k-value of the transition, given by:

$$\frac{1}{m_d^*} = \left(\frac{1}{m_0^*}\right)\left(1-\frac{\phi}{E_g}\right)$$

where

$$\phi = 0.8156(3\pi^2)^{2/3}\left(\frac{\hbar^2}{2m_0^*}\right)n^{2/3}$$

allowing for the non-parabolicity of the conduction bands.

These samples have a doping level of $n = 3\times10^{18}$ cm^{-3}. Taking $E_g = 1.52$ eV (at 4 K) and $m_0^* = 0.0665m_0$ gives a Fermi energy of 107 meV.

4.5.4. The Franz-Keldysh Effect

The Franz-Keldysh effect[38,39] or electroabsorption effectively lowers the measured band gap. It occurs when an electron makes a transition in the presence of an electric field (Figure 29) and can be thought of as photon assisted tunnelling across the band gap.

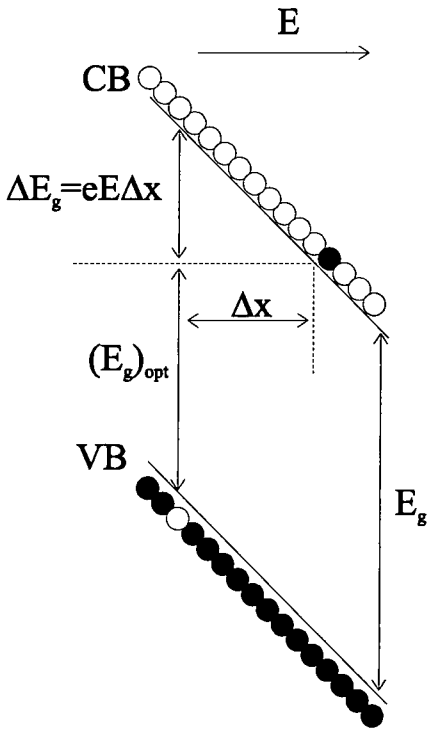

Figure 29: Optical transition in an electric field for a semiconductor

The result is that at a given photon energy the absorption increases with electric field intensity. The absorption coefficient, α, is proportional to:

$$\alpha \propto \exp\left(\frac{-4\sqrt{2m_e^*}(E_g - \hbar\omega)^{\frac{3}{2}}}{3|e|\underline{E}\hbar}\right)$$

for photon frequencies below the band gap. This can be interpreted by using a shift of the absorption edge to lower photon energies. This shift of the absorption edge depends on the electric field strength and the electron effective mass. The apparent shift of the band gap, ΔE_g, is given by:

$$\Delta E_g = \left(\frac{3|e|\underline{E}\hbar}{4\sqrt{2m_e^*}}\right)^{\frac{2}{3}}.$$

For the samples here, assuming an uniform field through the depletion regions, using $\underline{E} = 3.5\times10^5$ Vcm^{-1} and $m^*_0 = 0.0665m_0$ gives an expected shift of around 73 meV. However, the edges of the region will experience higher fields of $\underline{E} = 7\times10^5$ Vcm^{-1} and the shift will be larger: 116 meV.

This is a red shift and will compensate partly for the Moss-Burstein blue shift calculated above. As a result it is difficult to calculate the expected energy of the onset of absorption. It would be possible to reduce the doping level slightly in different samples and hence the Moss-Burstein shift. However, the membranes will become completely depleted if the carrier concentration were less than $1.4\text{x}10^{18}$ cm^{-3}.

The absorption spectrum at 4 K shows more structure than at room temperature. There is a sharper absorption edge at 1.507 eV, compared to 1.52 eV for bulk GaAs[40]. There is also an increasing absorption below the band gap beginning around 1.4 eV. This absorption below the band edge has been seen in thicker bulk GaAs samples which have been heavily doped and has been attributed to band gap narrowing and many body effects[41]. In comparing the absorption spectrum at 4K with thicker bulk GaAs

layers[42] the most notable differences are the prominent absorption occurring below the band edge, the absence of excitonic absorption and the shift to lower energy of the absorption edge.

The absence of excitonic absorption peaks is due to two factors. In the depletion region any exciton formed will have a very short lifetime due to the high electric field and so any transitions will be broadened out in energy. In the central region of the membrane screening effects due to the high doping density will reduce the exciton binding energy and hence the probability of exciton formation.

The increased absorption below the band edge is due to absorption in the two depletion regions being shifted by the Franz Keldysh effect as described above. This effect will also occur in thicker GaAs layers but here the depletion region constitutes 72% of the sample thickness and so it is not surprising that this is a dominant feature in the absorption spectrum. With a peak electric field at the surface of $7x10^5$ Vcm^{-1}, this will give a red shift of 116 meV[43]. This could explain the onset of absorption below the band gap.

In calculating the strength of the absorption coefficient it is necessary to assume a certain thickness of sample. If it is assumed that the band edge feature is due to a uniform absorption throughout the membrane this gives $\alpha = 7500$ cm^{-1}. This compares with $\alpha = 9400$ cm^{-1} in bulk GaAs layers[44]. However, it is unlikely that the feature is due to absorption throughout the entire membrane. If instead it is assumed that this feature is due to absorption only in the undepleted central region a value of $\alpha = 26800$ cm^{-1} is obtained. Clearly the absorption coefficient will lie somewhere between these two limits. To obtain a value for the absorption coefficient comparable with the bulk

GaAs value the transition would have to occur over a region 46 nm wide.

4.5.5. L Point Transition

The absorption in the range 2.2 eV to 3.6 eV measured at temperatures ranging from 77 K to 300 K is shown in Figure 30. This absorption is due to a transition across the band gap at the L point in the Brillouin zone. The increased noise at the higher energies is due to the low number of photons emitted by the source at those energies. The slight jump in the absorption values around 2.75 eV is caused by a filter change in the monochromator at 450 nm. This was attributed to errors caused by the experimental apparatus.

To determine the energy gap from the absorption data we used a plot of the absorption squared versus energy. This reflects the energy dependence of the density of states at the valence and conduction band extrema as is explained in Section 2.6.1 and gives the most accurate means of evaluating the energy gap from our data. The temperature dependence of this transition is shown in Figure 31.

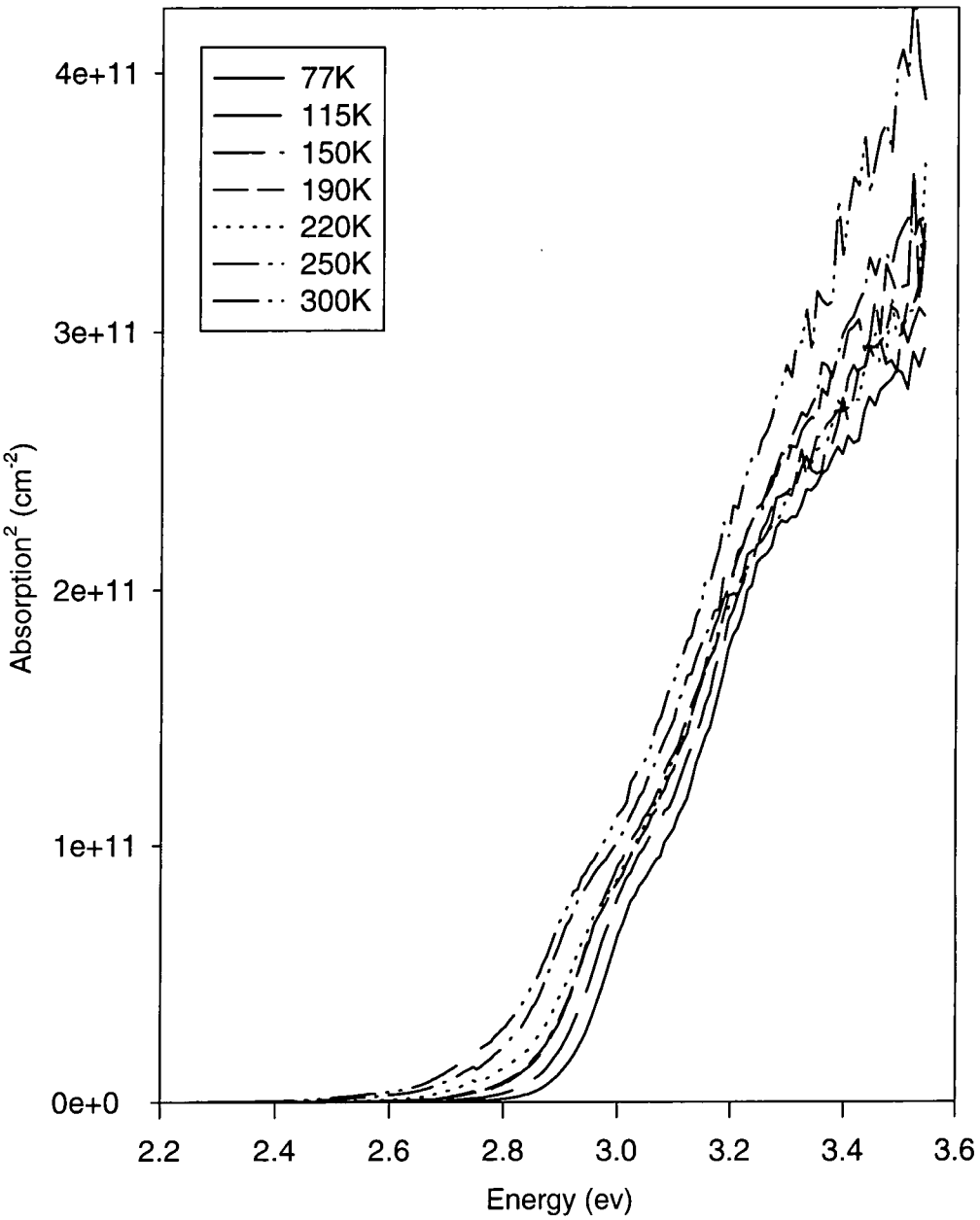

Figure 30: The temperature dependency of absorption due to the L-point transition

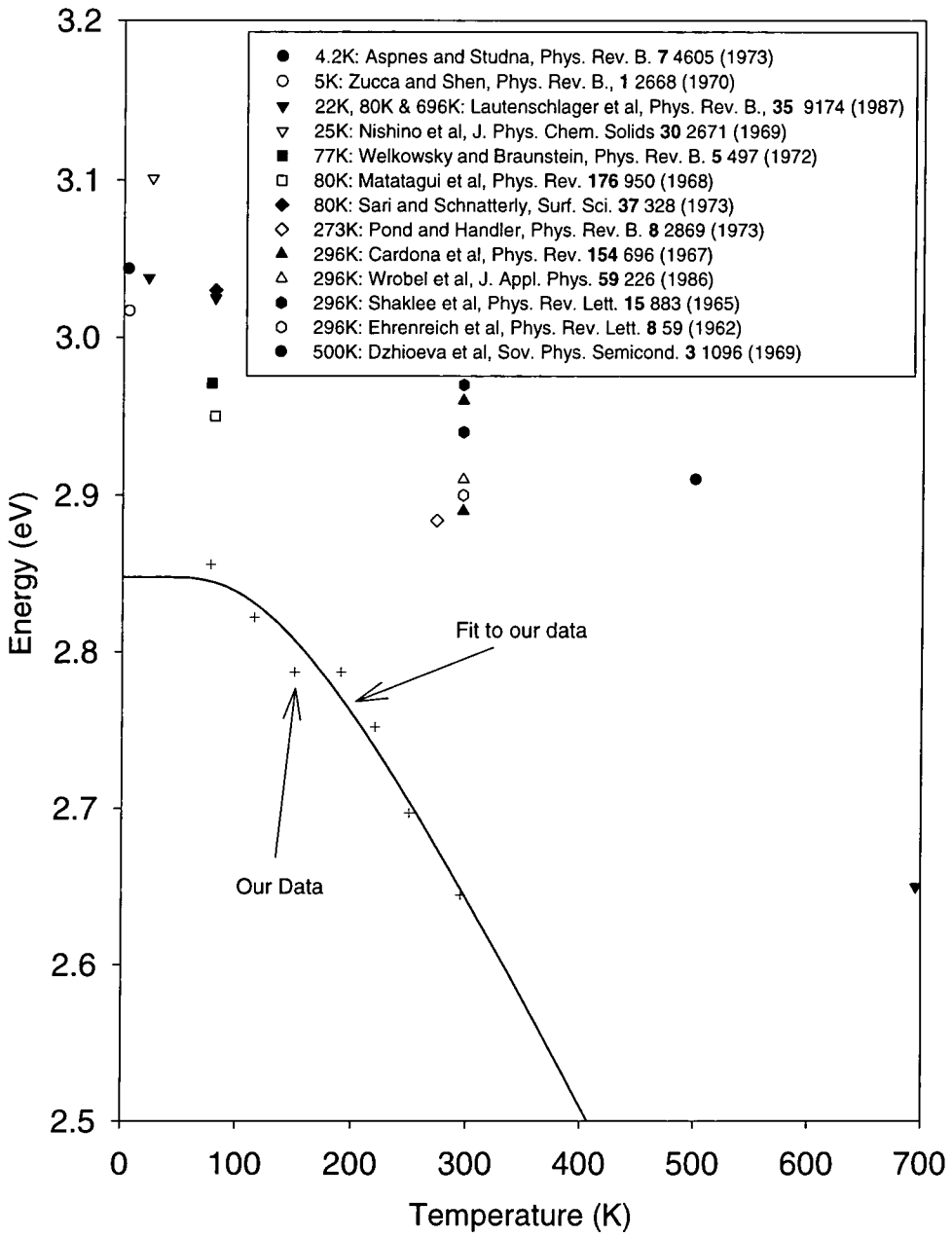

Figure 31: Temperature dependence of the L-point band gap and other data

Also in Figure 31, other data taken from Lautenschlager et al[45] is plotted for a comparison. This was obtained from undoped samples using reflectivity measurements. Our data shows that the energy gap decreases as the temperature increases, as expected. This results mainly from the electron-phonon interaction[46] but

also from the thermal expansion of the lattice. The traditional method of describing the temperature dependence of a band to band transition has been using the Varshni equation given by the relation[47]:

$$E(T) = E(0) - \frac{\alpha T^2}{T+\beta}$$

This is an empirical relationship which gives a T^2 energy dependence below the Debye temperature and a T energy dependence above the Debye temperature though this is known to have difficulty in describing the observed temperature dependence of some semiconductors.

Vina et al have developed a more theoretical description given by[48]:

$$E(T) = E_B - a_B\left(1+\frac{2}{\exp\left(\frac{\Theta}{T}\right)-1}\right)$$

This is based on the fact that the electron-phonon interaction is the dominant mechanism in determining the change of energy gap with temperature. The equation results from the change of the electron-phonon interaction and is based on a Bose-Einstein occupation factor for an average phonon energy. Fitting our data to the Vina equation gives the values : $E_B = 3.165$eV, $a_B = 317$ meV and $\Theta = 422$K. This is consistent with the value of 360K for the Debye temperature in GaAs[49] although the number of points in the fit is not enough to derive a meaningful error. The fit is shown as a solid line in Figure 31. The data from other work plotted in Figure 31 is obtained from fits to reflectivity data[17]. Although there is a spread of ~0.1 eV in the reflectivity data, it is clear that our results are consistently below the reflectivity data by an average of 0.17 eV.

Other measurements of this energy gap have been made on thin evaporated non-crystalline films and give a value of 2.97 eV[18]. The reason for this shift between our

data and previous results is the Franz-Keldysh shift[11,13]. Under the influence of the large electric field resulting from the surface depletion an electron will be able to make the transition from valence to conduction bands at a lower energy as described in section 4.5.4. Given the size of the Franz-Keldysh shift is 122 meV it is possible to use the expression for the band gap shift given in section 4.5.4 to calculate the effective mass of electrons at the L-point conduction band minima. Using an electric field of $7x10^5$ Vcm^{-1} gives an electron effective mass of $0.057m_o$ which is close to that of the Γ minima and also to that found by Aspnes and Studna[50] for the transverse effective mass at the L point of $0.0754m_e$. The shift of the absorption edge is much more sensitive to the electric field ($E^{2/3}$) than the effective mass ($m_e^{*-1/3}$). The only means of determining the electric field present in our samples is by assuming a doping level of $3x10^{18}cm^{-3}$ and that the Fermi level is pinned in the middle of the band gap at the surface. As a consequence, the effective mass determined from our data is very approximate. The Moss-Burstein shift will not effect this transition as the Fermi level is well below the L minima in the conduction band. The effect of the Franz-Keldysh shift will be to alter the parameter E_B in the fit to the temperature dependence of the energy gap.

The magnitude of the absorption coefficient is determined by assuming the absorption occurs in the 14 nm undepleted region in the centre of the membrane. There are no other reported values of the absorption coefficient for this transition.

Another feature is visible in the absorption spectra at 0.2 eV above the absorption edge. This is most clearly resolved for the spectrum at 77K. This feature results from transitions to a different valence band at the L-point which originates from the spin-orbit splitting of the valence band levels. This has also been observed in other measurements[51]. This can be seen in Figure 10 as the L_{6v} - L_{6c} transition.

4.6. Strain Effects

As the temperature of the structure is reduced it is possible that the membrane will become strained. To allow us to estimate the effect of any strain introduced we assume that the device is unstrained at room temperature. We also assume that the membrane is attached to a substrate which has a thermal expansion coefficient of the $Al_{0.3}Ga_{0.7}As$ etch stop layer. In practise the difference in thermal expansion coefficients will be less than this because of the GaAs substrate and buffer layer. The thermal expansion coefficient of GaAs at 300K is $\alpha = 6.4 \times 10^{-6}\ K^{-1}$ and for $Al_{0.3}Ga_{0.7}As$ $\alpha = 6.0 \times 10^{-6}\ K^{-1}$ [52]. For GaAs α drops towards zero and tends to become negative at very low temperatures[53]. Our estimate of the lattice mismatch on the strain introduced into the membrane by cooling from 300K to 77K using the room temperature values for α is thus a maximum value. Changing the temperature from 300K to 77K will give a deformation of the film. The strain tensor, $[e]$ is given by:

$$[e] = [\alpha]T$$

where $[\alpha]$ is the thermal expansion tensor and T is the temperature change. In zinc blende cubic crystals this can be approximated by the scalar quantity α given above, where α is the linear expansion coefficient of the lattice given by the equation[54]:

$$\alpha = \frac{1}{a_0}\left(\frac{\partial a_0}{\partial T}\right)_P$$

For the membrane this will produce a strain of $e = 8.92 \times 10^{-5}$ on cooling. This will be a biaxial tensile strain in the plane of growth as the GaAs contracts more than the AlGaAs layer. This strain can be divided into two components : isotropic (hydrostatic) and anisotropic. The hydrostatic component gives a volume change in the crystal without perturbing the symmetry and so will only change the energy band gap. The

anisotropic component will reduce the symmetry and split the degeneracy of the valence bands. For the membrane this axial component will be will be perpendicular to the membrane. The change of band gap will be given by:

$$\Delta E = 2a_c\left(\frac{C_{11}-C_{12}}{C_{11}}\right)e$$

where e is the strain, C_{11} and C_{12} are the elastic constants and a_c is the absolute intraband hydrostatic deformation potential. At the L point in GaAs this has been measured as 19.6 eV[55]. The energy change introduced by the strain calculated above will be ~1.8 meV. This is much less than the observed difference. To produce a shift of 170 meV by strain alone would require a strain of 8×10^{-3} which is much larger than can be produced by a lattice mismatch in the GaAs/AlGaAs material system. It is then unlikely that strain plays a significant role in these structures.

4.7. Conclusions

A study using optical absorption has been made of the properties of 50 nm thick GaAs membranes. This has shown effects due to surface depletion and high doping levels. It is also possible to directly observe transitions across the band gap at the L-point of the Brillouin Zone and the effective mass of electrons at the L-point conduction band minima has been calculated to be similar to that at the Γ-point.

5. ELECTROLUMINESCENCE FROM POROUS SILICON USING A CONDUCTING POLYANILINE CONTACT

5.1. Summary

We have fabricated a p-n junction using a p-type conducting polyaniline layer deposited on an n-type porous silicon layer. This junction shows rectifying behaviour. The IV curves can be fitted to a Schottky barrier model with a barrier height of 0.8 eV. The porous silicon shows an orange photoluminescence band due to recombination in the silicon quantum structures both before and after coating with polyaniline. The junction emits visible electroluminescence when a forward bias is applied. The emission band is very broad extending from 500 - 1000 nm with a peak at 790 nm. Mechanisms for charge transfer between the porous silicon and polyaniline are discussed.

5.2. Introduction

Although porous silicon was first reported by Ulhir in 1956[56] and then Turner in 1958[57], as an unwanted by-product of the electrochemical etching of silicon, it was the discovery of above band gap visible photoluminescence first at 4.2 K in 1984 by Pickering et al[58] and more importantly at room temperature by Canham[59] in 1990 that has thrust the material into the scientific focus. Since 1990, numerous studies

have demonstrated that it is possible to achieve efficient visible luminescence from porous silicon layers[60]. Porous silicon can best be described as nanometre sized sponge like crystalline silicon[61] regions (mean diameter of ≈30Å) surrounded by empty space, as is shown schematically in Figure 32. See Collins et al[62] for a recent review article.

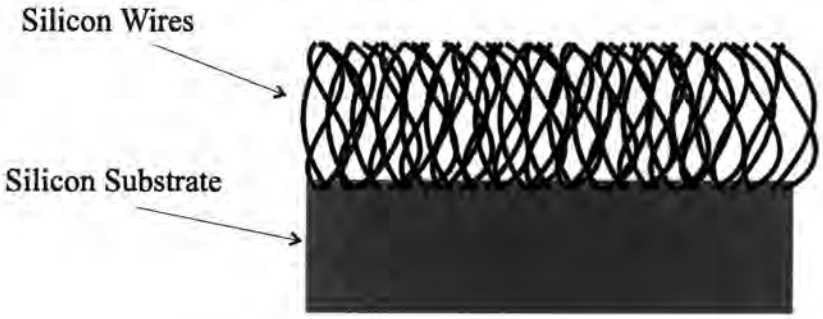

Figure 32: Structure of porous silicon.

5.2.1. Applications

The major area of interest for porous silicon use is as a material towards the technologically important goal of producing optoelectronic devices consisting entirely of silicon. Due to bulk silicon having an indirect band gap, efficient emission from it is inhibited by the necessary inclusion of a phonon in the electron-hole recombination which reduces the probability of photon emission by a factor of $\approx 10^5$. Yet silicon's ease of processing and good structural properties, together with 40 years of research and development into its technology make it attractive as a material for use in integrated optoelectronic devices. The future economic potential of porous silicon is significant in that efficient visible emitters could be fabricated on silicon wafers and incorporated with microelectronic devices using existing VLSI technologies.

Apart from optoelectronic applications, the large surface area to volume ratio of porous silicon makes it a good candidate for sensing applications such as moisture or chemical detection.

In addition, porous silicon can also be a bioactive material unlike bulk silicon which is bioinert and can not be used for invasive or biosensing applications. Porous silicon with low porosity (≈20%) has been shown[63] to interact with biological systems which implies biosensors could be fabricated on silicon, opening an important new research area. Bioactive materials respond when in vivo by allowing a bond to form to living material. This process involves the nucleation and growth of a layer constructed from a major constituent of bone, hydroxyapatite ($Ca_{10}(PO_4)_6(OH)_2$). Possible systems include invasive sensing, biosensing, intelligent drug delivery systems and many other prosthetic electronic devices such as the treatment of chronic pain[64] and cell fusion.[65].

5.2.2. Light from Silicon

Although III-V materials generally have direct energy gaps and improved electronic properties (such as higher mobilities) the technology is not as well developed for mass manufacture of VLSI III-V integrated chips. Therefore hybridisation of III-V devices with silicon based systems is the accepted production method for optoelectronic devices though two major problems exist with this, namely the lattice and polar / non-polar mismatches between the two systems.

Hence attempts have been made to find an all group IV based system by attempting to engineer a larger overlap between the electron and hole wavefunctions in both real

and reciprocal space therefore increasing the likelihood of luminescent recombination by removing the need to include a phonon. Methods include:

i) doping the silicon with an "isoelectronic" element[66] (such as sulphur[67]) or a rare-earth element[68] (such as erbium). Erbium has transitions between symmetry states which emit electromagnetic radiation at the technologically important wavelength of 1.55 μm.

ii) using pressure to modify the bandstructure to create a direct gap. The deformation potentials for the Γ and X points in silicon do have opposite signs, but negative pressure has to be applied to get them to move in the correct directions.

iii) alloying with other group IV elements or systems to create a direct gap band structure. However, Si-Ge and Si-C alloys do not increase the direct transition probability. Ge-Sn alloys can possess a direct gap for certain composition ranges[69], but E_g can only range between 0 and 0.5 eV and the lattice mismatch between the Ge-Sn system and the silicon substrate is large enough to cause problems with miscibility. Tin is a direct gap semi-metal but it has too large a lattice mismatch with silicon to be grown on it successfully.

iv) using a superlattice of silicon and germanium layers of the appropriate thickness' to "zone fold" the conduction band minima back above the valence band maxima[70] allowing a quasi-direct transition. However, the transition probability produced by this method is too weak to provide efficient recombination.

v) using quantum confinement (quantum wells, wires or dots) to confine the particles in a narrow region, and thus increase the probability of photon emission and also the energy of emission[71]

However all of the above systems are either to difficult to create in practice or do not improve the efficiency of light emission to an acceptable level.

Porous silicon is related closely to v) as it consists of an extremely fine sponge made from silicon wires; the practical difference is that quantum wells require high technology MBE growth reactors which cannot be used for cheap mass production.

5.2.3. Theory of light emission

Several theories have been suggested since 1990 to explain the observed luminescence. These include quantum confinement[72,73], contaminated amorphous silicon[74], hydrogen related polysilane surface centres[75,76], siloxene ($Si_6O_3H_6$) derivatives[77,78,79]. The presently accepted explanation unifies several of the older descriptions.

Porous silicon possesses two main emission bands; the F band around 2.75 eV (blue-green light) and the S band around 1.75 eV (orange-red light). The average recombination time of the S band is of the order of microseconds whereas the F band luminescence occurs on a much faster timescale of nanoseconds. The diameter of these wires is a few nanometres. Studies by Nash et al[80] have shown conclusively that the commonly observed visible luminescence band in the red-orange region is due to indirect radiative recombination of quantum confined excitons[81,82] in the crystalline silicon wire nanostructures, whereas the F band is currently attributed to the recombination of electrons and holes at sites in a surface layer on the porous silicon (probably consisting of SiO_2) as shown in Figure 33.

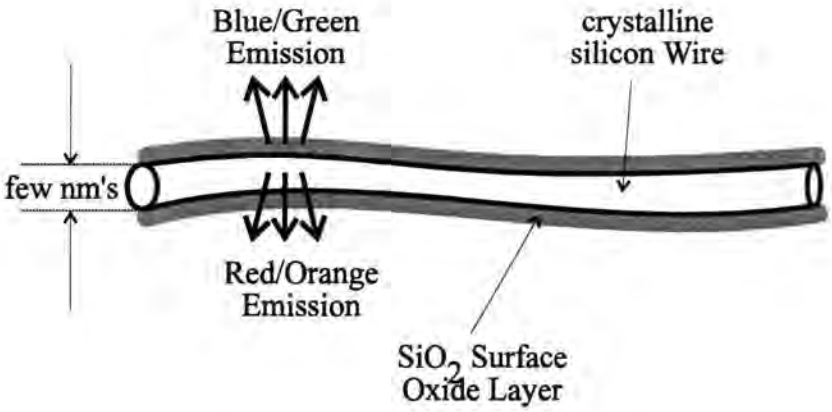

Figure 33: Light emission from porous silicon

The shift of the band gap into the visible is due to quantum confinement. The quantum structure also results in the formation of a pseudo-direct gap[83] which together with the decrease in non-radiative centres and the increase in the electron-hole concentration increases the efficiency of radiative recombination by over 10^5.

5.2.4. Problems with porous silicon devices

In order to fabricate a useful device out of porous silicon several issues must be addressed. In order to inject carriers under a low bias and get efficient electroluminescence, any system used to make electrical contact must be transparent to the optical emission, have a low resistivity but can not short circuit the porous silicon and must not react with the silicon which might destroy the luminescence through damaging the passivation of the surface. There have been investigations which have shown that the optical emission degrades slowly with time from porous silicon layers[84]. This is thought to be due to oxidation at the surface of the silicon wires . A number of different contacting schemes have been tried: semi-transparent metal layers, indium tin oxide, silicon carbide and conducting polymers[85].

Polyaniline is a good candidate for fabrication of a transparent conducting contact to porous silicon. It has several advantages over other possible contact materials: it has a transmission window over part of the visible spectrum so the thickness of material is not critical to device operation and in addition a device can be fabricated by two chemical based steps without requiring ion implantation to produce a p-n junction.

5.2.5. The PS-PANi Device

We report here the fabrication of a rectifying junction between conducting polyaniline and porous silicon. Previous studies incorporating polyaniline as a contact used a porous silicon p-n junction formed by ion implantation and annealing to create the junction[86]. Other work has demonstrated that it is possible to grow electrically active polyaniline films onto porous silicon by immersing the films in the monomer followed by electrochemical polymerisation. This method has been shown to start the polymerisation at the bottom of the pores and propagate towards the surface[87]. There has been a report of successful electroluminescence from a porous silicon/polyaniline device[88] using a structure involving the growth of the polyaniline using a layer by layer approach. We create a junction directly between the conducting polymer and the porous silicon using a single step process. A diagram of the completed device is given in Figure 34.

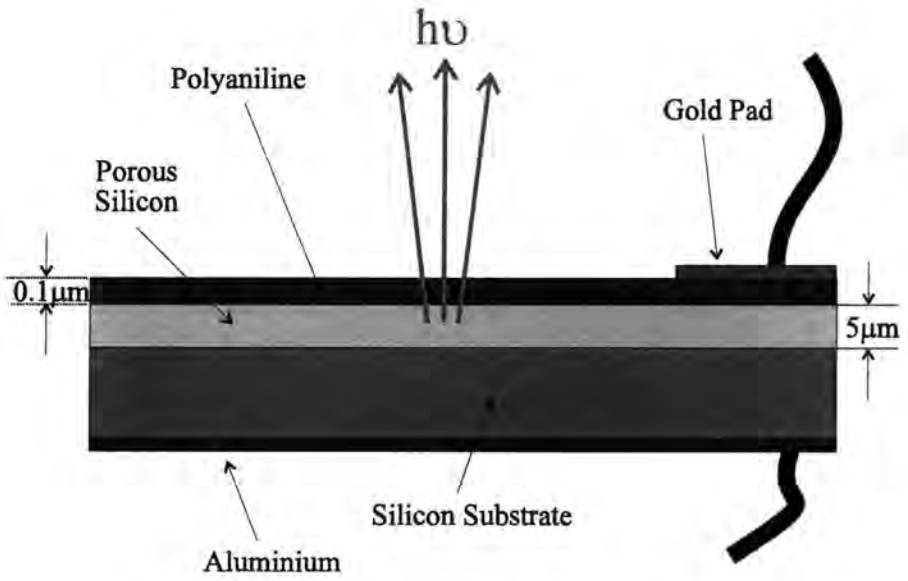

Figure 34: Porous silicon-polyaniline device

5.3. Production of porous silicon-polyaniline devices

5.3.1. Porous silicon

When silicon is electrochemically anodised in hydrofluoric acid the result is a skeletal structure consisting of monocrystalline wires as shown in Figure 32. The silicon wafers used were 1 inch diameter (111) oriented n-type substrates with resistivities between 5 - 10 Ωcm. A layer of aluminium was evaporated on the back of the substrate and annealed at 500 °C to produce an ohmic contact. The wafers were anodised in a solution of 17% HF in ethanol. The electrochemical anodization process requires holes for the dissolution of silicon from the surface so the wafers were illuminated by a 150W tungsten lamp during the etching process to produce holes. The samples were etched for up to five minutes at current densities between 10

and 60 mA cm^{-2}. The experimental arrangement is depicted in Figure 35. This will produce porous silicon layers of around 5 μm thickness.

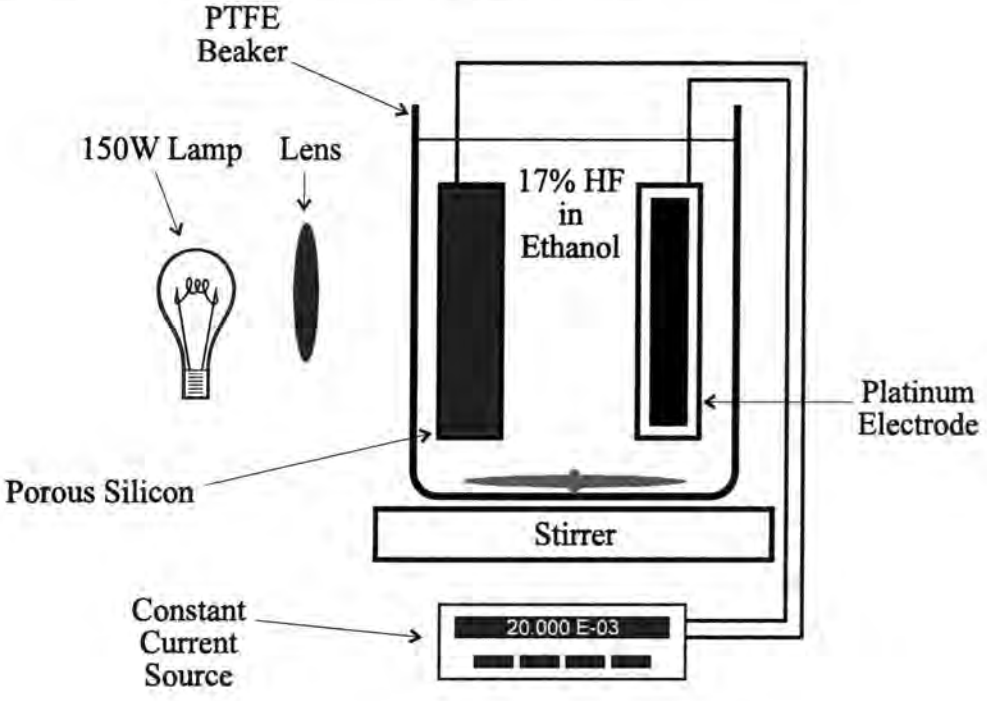

Figure 35: Etching of porous silicon

All wafers exhibited a visible luminescence band with a peak around 600 nm.

5.3.2. Deposition of polyaniline

Several methods of depositing polyaniline onto the porous silicon were tried:

i) Electrochemical growth from a solution of aniline hydrochloride. This method did not produce uniform coverage and the resulting films were of a very poor quality.

ii) Dip of the porous silicon in aniline hydrochloride solution followed by a dip in an oxidant (ammonium persulphate). This produced only very thin non uniform films which were very difficult to contact.

iii) Spin coating with a solution of polyaniline in meta creosole then post doping of the PANi with HCl.

iv) Solution of polyaniline/camphorsulphonic acid in meta creosole. The chemical structure of this material is shown in Figure 36. This produces doped films of high quality in one step and this method was preferred.

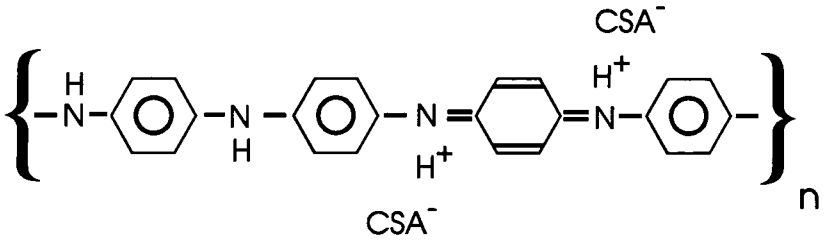

Figure 36: Polyaniline camphor sulfonic acid

A few drops of the polymer solution were placed on the surface of the porous silicon and the wafer was then spun to produce a thin uniform film across the surface of the wafer. The film thickness was 0.1 μm. This method gave the best films. Electrical contact was made to the polyaniline film by an evaporated gold pad and wires were attached using silver paint.

5.4. Experimental Details

Spectra were recorded using a 0.25m grating spectrometer and a silicon photodiode array. The photoluminescence spectrum was excited using the unfocused 488 nm line of an Argon ion laser or a mercury lamp. The layout of the optical experiments is shown in Figure 37. A 488.0 nm line filter was used to select the required laser emission, and an OG515 filter (515 nm high band pass) ensured none of the laser light entered the monochromator system.

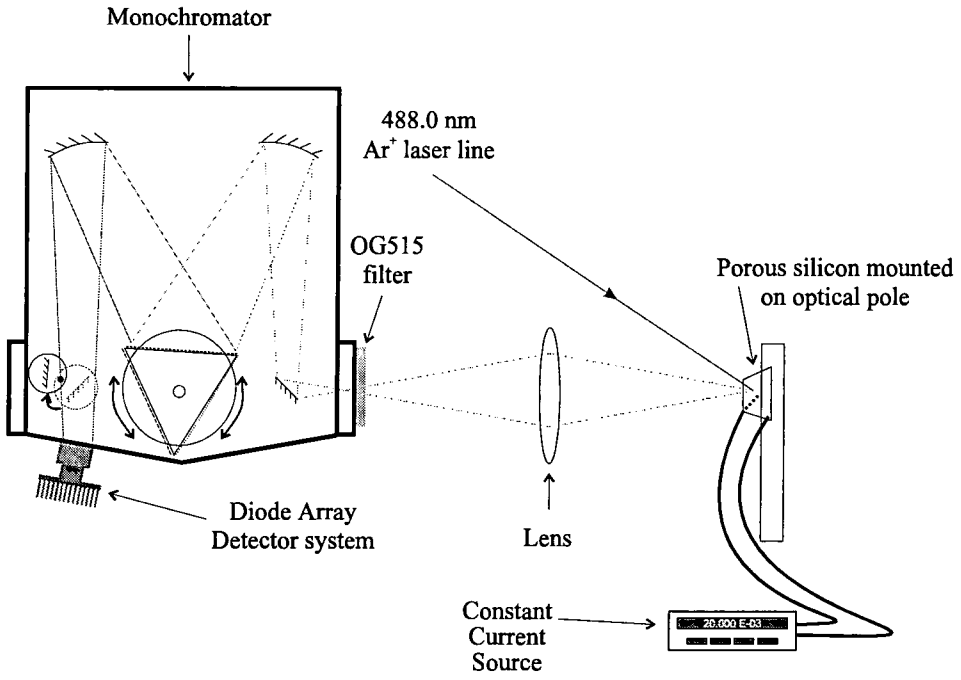

Figure 37: Experimental layout

The electroluminescence spectra were measured using exactly the same experimental layout with the sample connected to a current source and no laser excitation.

5.5. Results and Discussion

5.5.1. Optical Measurements

To ensure that the deposition of the polyaniline did not adversely affect the electrical and optical activity of the porous silicon, a series of measurements were performed. The photoluminescence spectra before and after coating with polyaniline are shown in Figure 38.

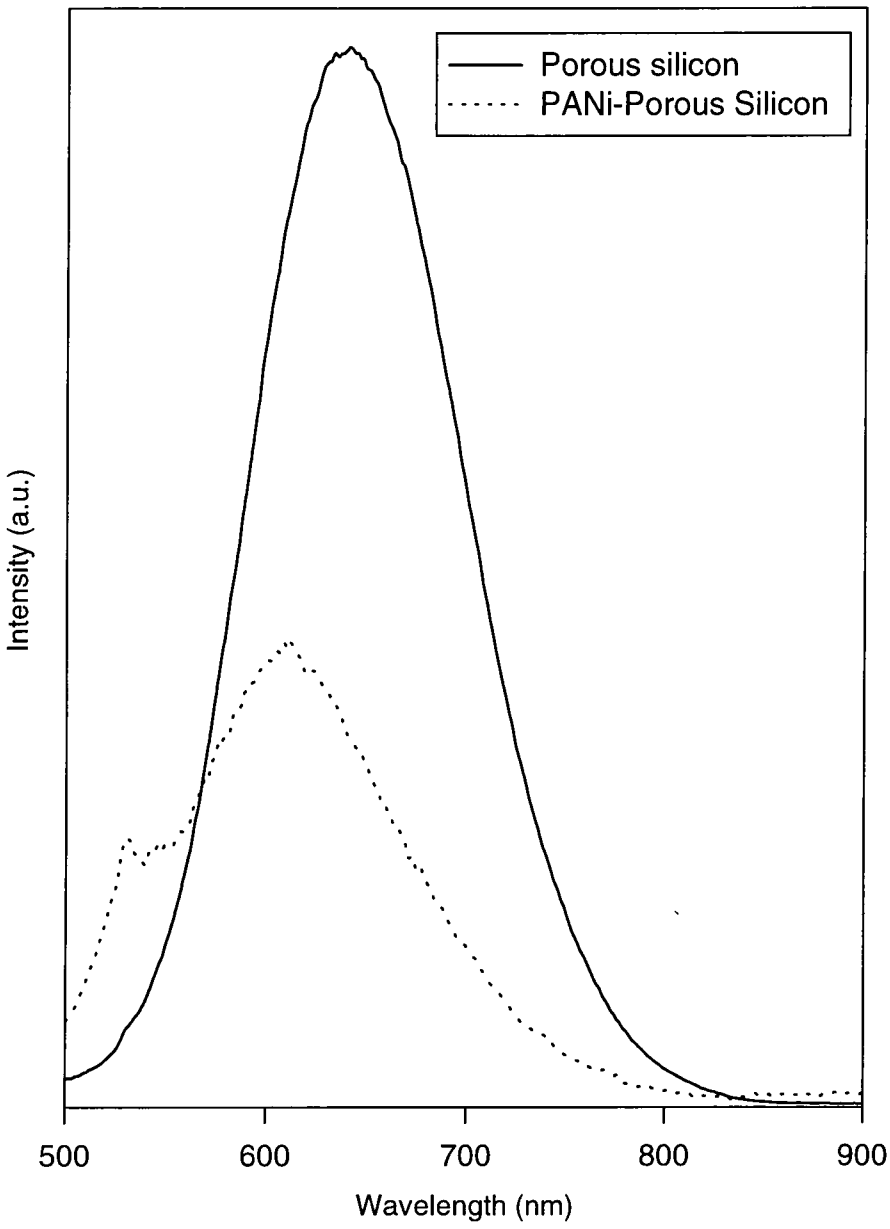

Figure 38: Photoluminescence spectrum of porous silicon

It is clear from this figure that there is a overall decrease in the total luminescence efficiency by 50%. This is primarily caused by absorption of the excitation and emission in the polyaniline film. Taking the absorption coefficient at the wavelength

of excitation and the absorption coefficient at the wavelength of photoluminescence emission into account, we arrive at an expected minimum decrease in the photoluminescence of around 25%. The fact that we can still observe luminescence on the coated porous silicon layer demonstrates that the polyaniline does not significantly alter the optical activity of the material. This gives support to the explanation for the origin of the red/orange luminescence band originating from recombination in the silicon crystal nanostructures. If the recombination were due to radiative channels in the surface of the nanocrystalline wires, we would expect coating the porous silicon with a conducting polymer to have a significant impact on the recombination mechanism.

The absorption spectrum of a doped polyaniline film deposited on glass is shown in Figure 39. This film was of a similar thickness to that on the porous silicon. It is clear from these measurements that the transmission window in our doped polyaniline film is close to the peak emission of the porous silicon making it an ideal candidate for a contacting material.

The excitation spectra of the porous silicon measured at 680 nm also shown in Figure 40 shows an increasing signal to shorter wavelengths. The excitation spectra has been shown to be related to the absorption coefficient of the porous silicon which is related to the density of states[89,90].

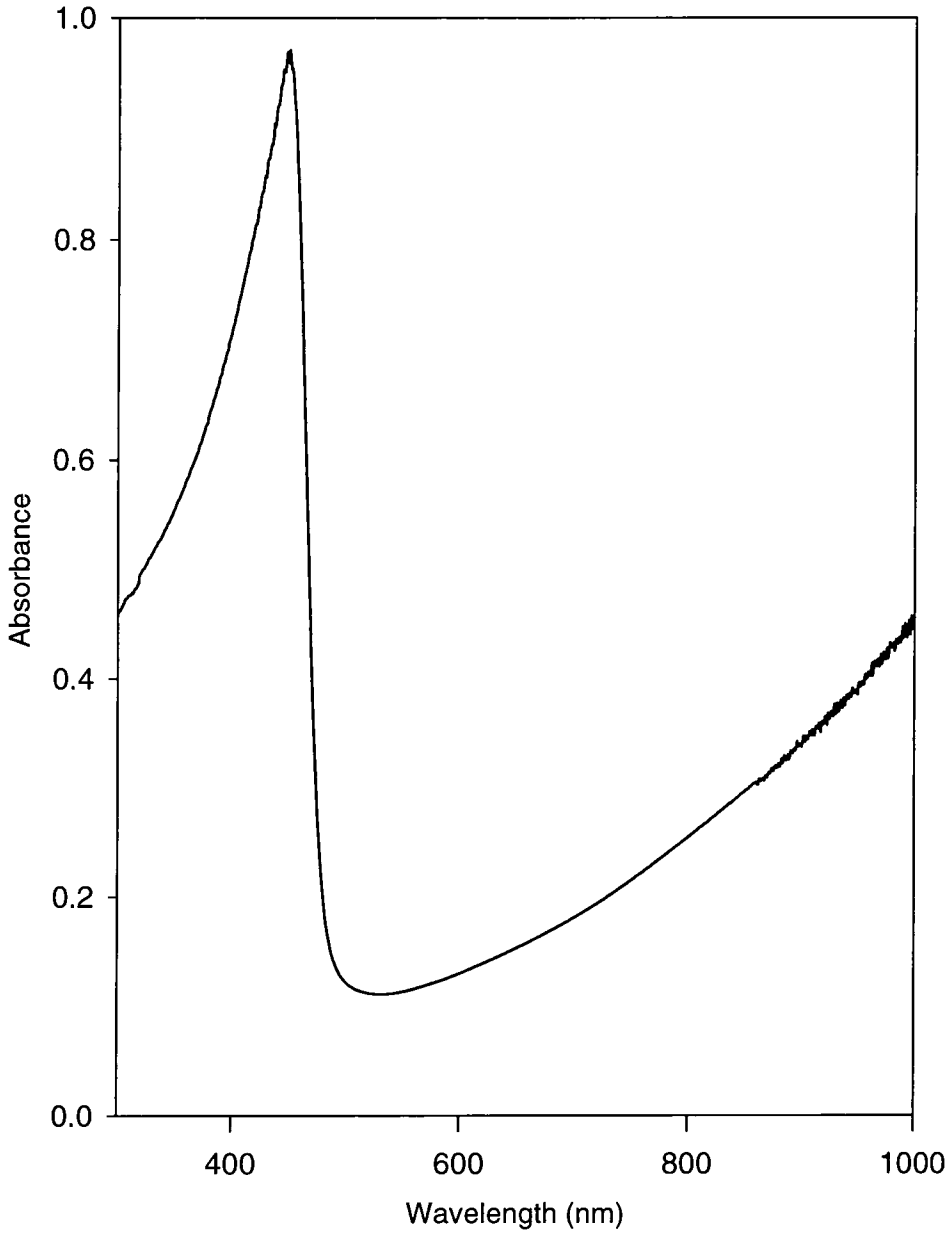

Figure 39: Absorption spectrum of a 0.1μm PANi film on glass

Figure 40: Excitation spectrum of porous silicon

5.5.2. Electrical Measurements

The IV characteristics of the polyaniline/porous silicon junction were measured using a constant current source and digital voltmeter. The IV curves are shown in Figure 41, Figure 42 and Figure 43.

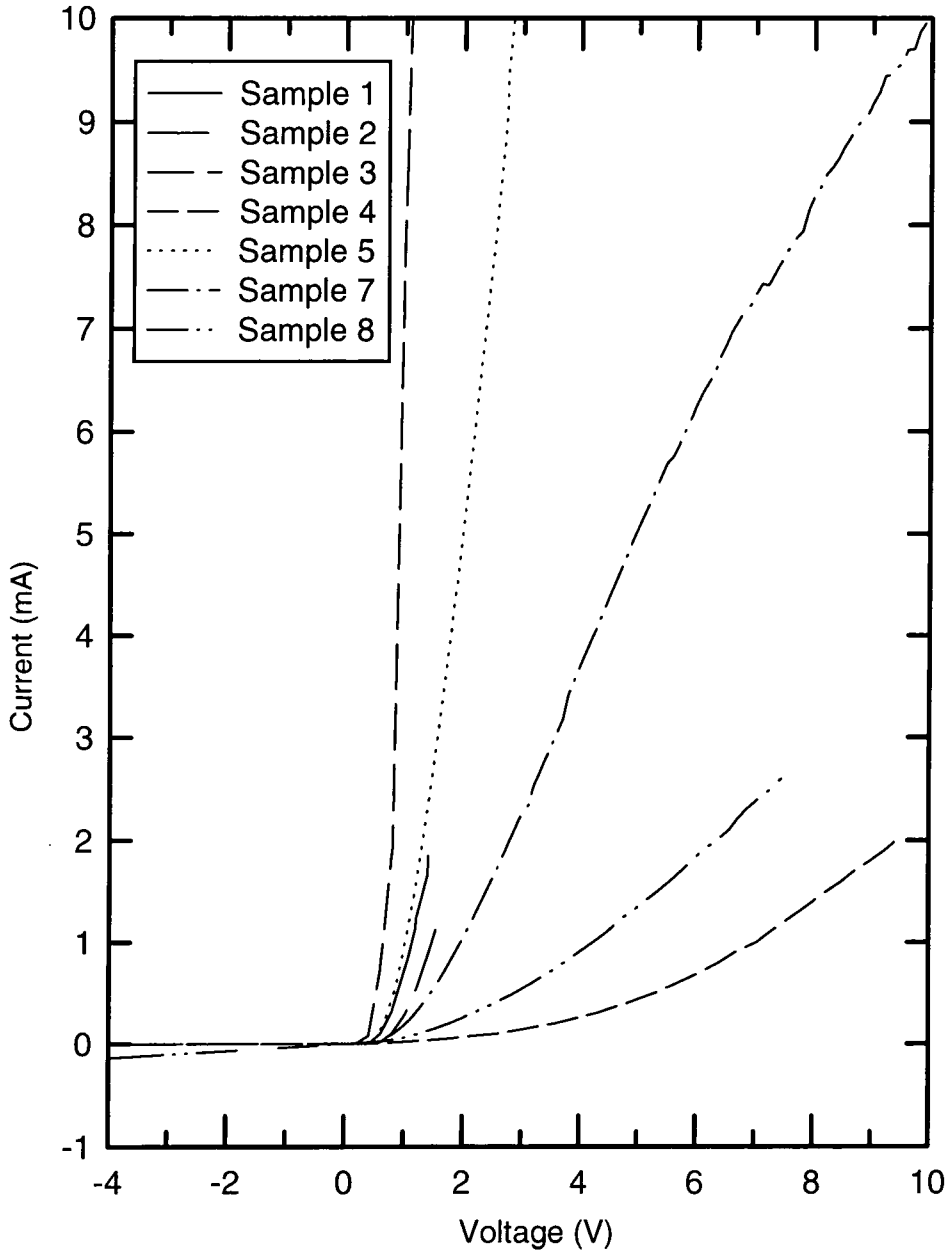

Figure 41: I-V data for samples

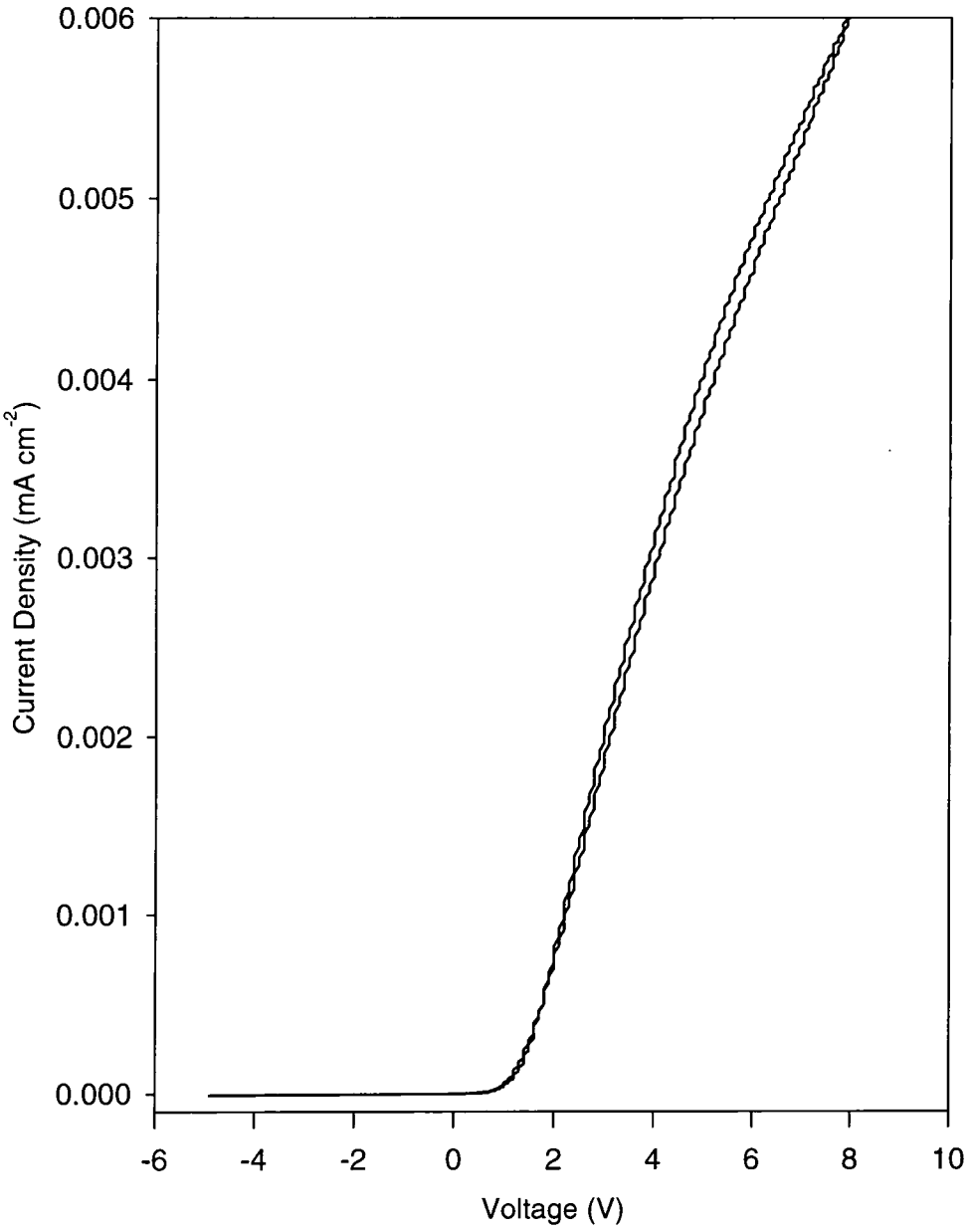

Figure 42: I-V characteristics of a porous silicon-polyaniline device

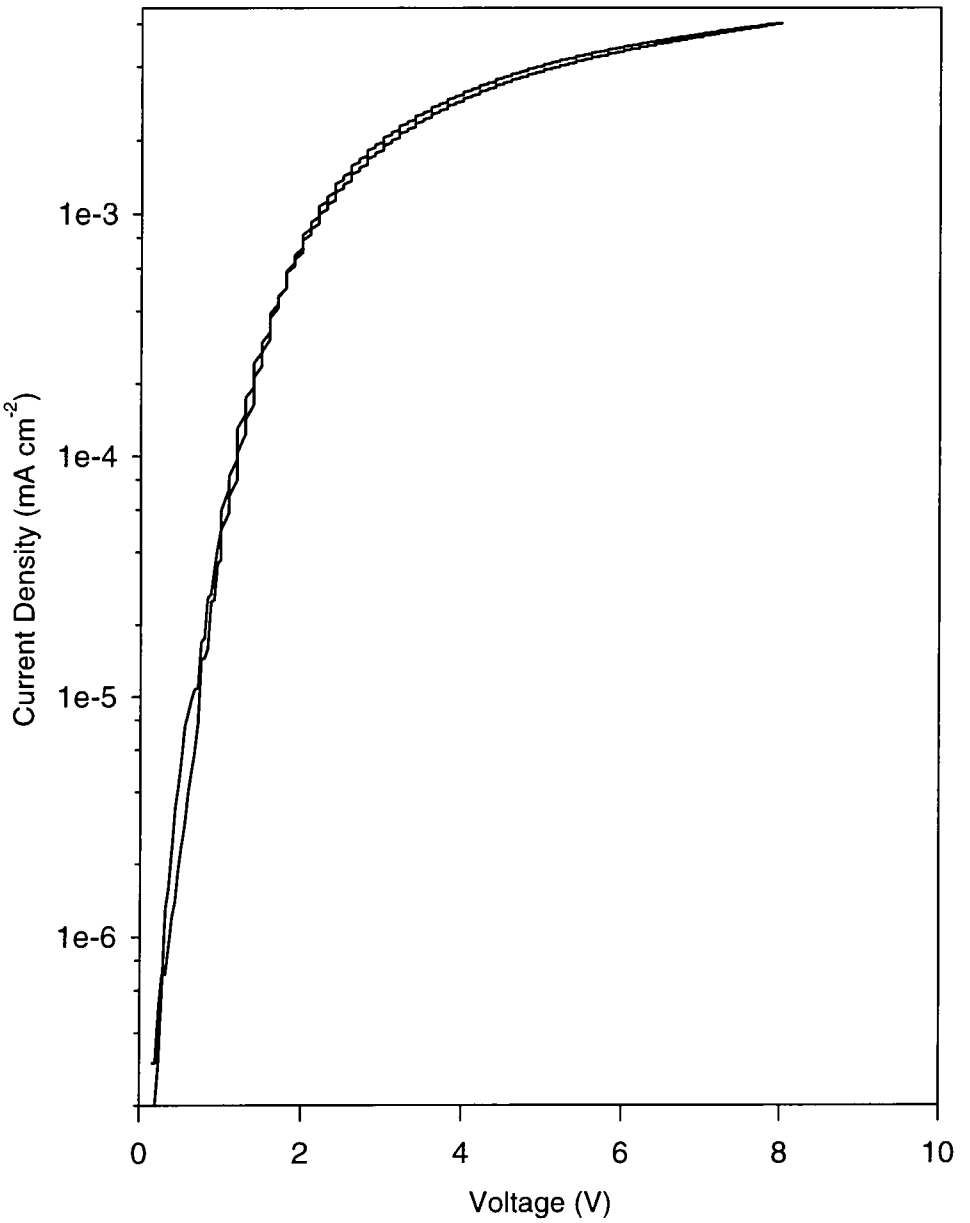

Figure 43: I-V characteristics of porous silicon-polyaniline device using a log scale

Polyaniline produced by the PANi-CSA route is p-type conducting. It is estimated that the hole concentration will be a maximum of 10^{20} cm^{-3}, this is assuming complete

dopant incorporation. Thermopower measurements on similar conducting polymer films do give a positive coefficient indicating p-type material[91]. Other measurements on polyaniline metal contacts have shown that the work function of polyaniline is between that of Au and Al, around 4.8 eV. We therefore expect that polyaniline deposited on a porous silicon substrate would behave as a p^+n junction and form a rectifying contact. The rectification ratio measured at ±5V is 490. The IV curves in Figure 41, Figure 42 and Figure 43 clearly demonstrate that we have formed a rectifying contact.

Illuminating the diodes with white light during the measurement increased the reverse bias current as expected from electron-hole pair generation in the depletion region. There is a hysteresis in the forward bias characteristics and this can be most clearly seen in Figure 42 and Figure 43. This may be due to charge transfer and trapping in the polyaniline film. The data shown in Figure 41 has been fitted to the standard expressions for an IV characteristic shown in the equations below:

$$J = J_s\left(\exp\left(\frac{eV}{nkT}\right) - 1\right)$$

with

$$J_s = A^* T^2 \exp\left(\frac{-e\phi_B}{kT}\right)$$

where V is the applied bias, n is the ideality factor, A^* is the effective Richardson constant and ϕ_B is the barrier height. The data from our fits is summarised in Table 5.1 below:

Sample Number	Series Resistance (Ω)	J_s (A cm^{-2})	Barrier Height (eV)	Ideality Factor n
1	307	2.14×10^{-7}	0.788	3.86
2	425	2.11×10^{-8}	0.846	3.84
3	393	5.55×10^{-8}	0.821	2.80
4	37	8.26×10^{-8}	0.812	2.40
5	828	3.70×10^{-8}	0.832	4.79
6	6309	3.12×10^{-7}	0.778	5.22
7	619	3.31×10^{-8}	0.834	3.49
8	1103	1.99×10^{-8}	0.847	3.42
9*	2008	5.67×10^{-6}	0.705	15.9

(* not used in obtaining the averaged numbers quoted in the text)

Table 5.1: Results of data fitting to IV curves

In our diodes $J_s = 9.7 \times 10^{-8}$ A cm^{-2}. The effective Richardson constant is 110 A cm^{-2} K^{-2} for n-type silicon [92], this gives a value of 0.8 eV for the barrier height. At larger bias voltages above +2 volts where the IV curve deviates from the normal behaviour, the data can be fitted by incorporating a series resistance of 1.6 kΩ into the model. For low forward biases of less than 2V fitting the curves gives a value of 3.7 for the ideality factor. Our polyaniline porous silicon junction behaves in a very similar fashion to a metal semiconductor contact.

5.5.3. Electroluminescence Measurements

When the device was forward biased (positive applied to the polyaniline) to give a current density of ~0.5 A cm^{-2} the junction emitted visible light. The electroluminescence spectrum is shown in Figure 44.

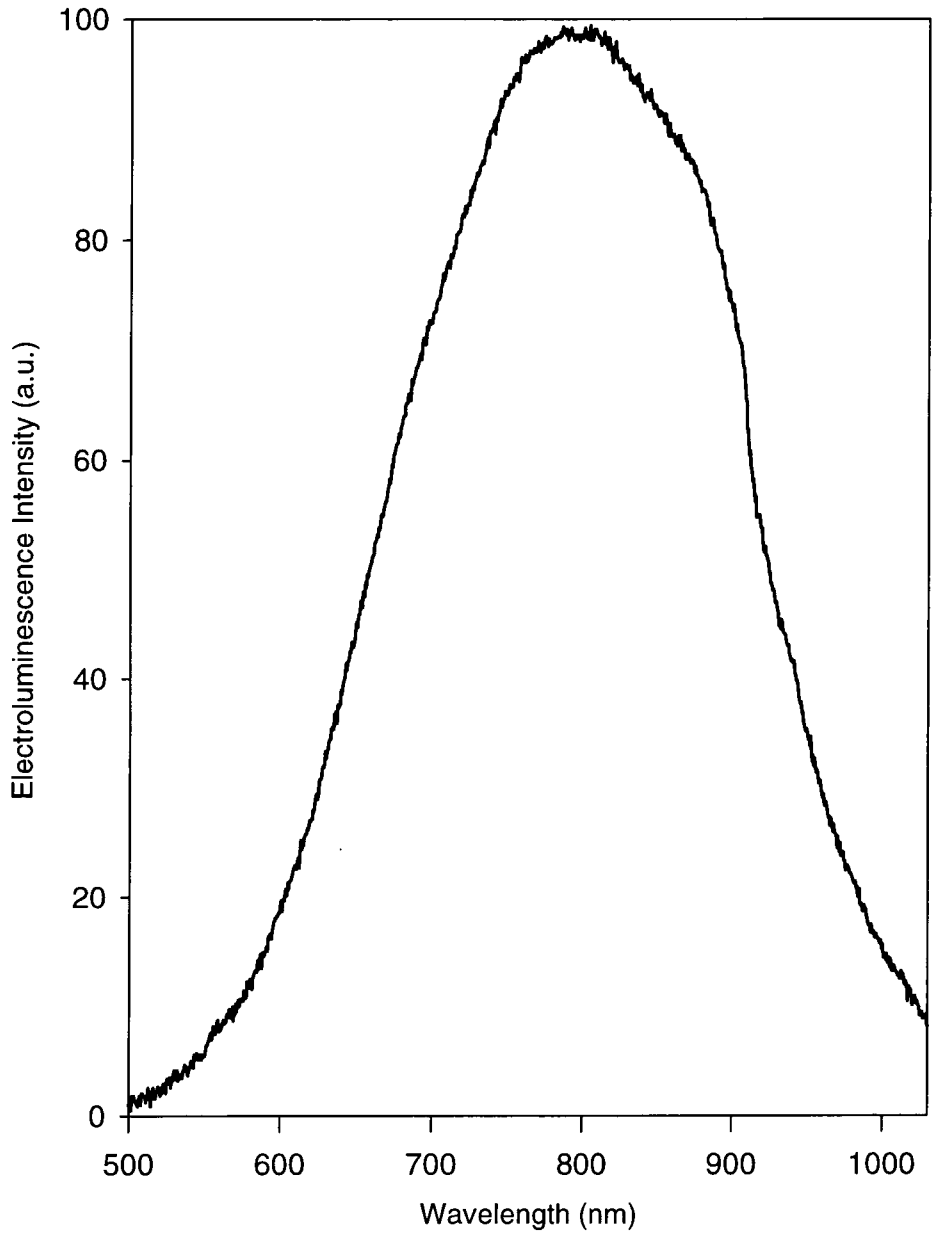

Figure 44: Electroluminescence spectrum measured from a PS-PANi junction with current density of 0.5 Acm^{-2}

Table 5.2 summarises the results for peak position and full width half maximum (FWHM) for all of the spectra from samples in this chapter.

Sample and spectral measurement	Peak		FWHM	
	nm	eV	nm	eV
PS PL	640	1.94	125	0.39
PS - PANi PL	610	2.04	150	0.44
PS - PANi EL	795	1.56	270	0.55

Table 5.2: Summary of spectral emissions from samples

The emission band has shifted much further into the infrared when compared with the photoluminescence spectrum in Figure 38. The band is also significantly broader than the photoluminescence band.

Comparable shifts are also observed in the porous silicon-polyaniline device fabricated using the layer by layer method[93]. This behaviour can be explained by considering the difference between the two excitation mechanisms. The photoluminescence will excite the material closest to the surface whereas the electroluminescence will be excited to a greater depth. The porous silicon wires will be much thinner closest to the surface. The red shift of the peak indicates the increase in the silicon wire thickness. The increase of the peak width shows that the electrical excitation is occurring over a larger range of silicon wire thickness than for the photoexcitation. This indicates that the polyaniline is making electrical contact to a significant fraction of the porous silicon layer. The electroluminescence originates from electron hole recombination in the porous silicon wires. The holes will be injected into the porous silicon valence band from the hole type polaron band in the polyaniline through a very thin silicon oxide layer. The Fermi level in the polyaniline will be at the polaron band, 1.3 eV above the bottom of the band gap[94]. The electrons will be injected from the n^+ silicon substrate through the silicon wires into

the porous silicon conduction band. This is scheme is shown in Figure 45: Diagram of junction energy levels. The exact mechanism of charge transfer between the polyaniline and porous silicon is not known.

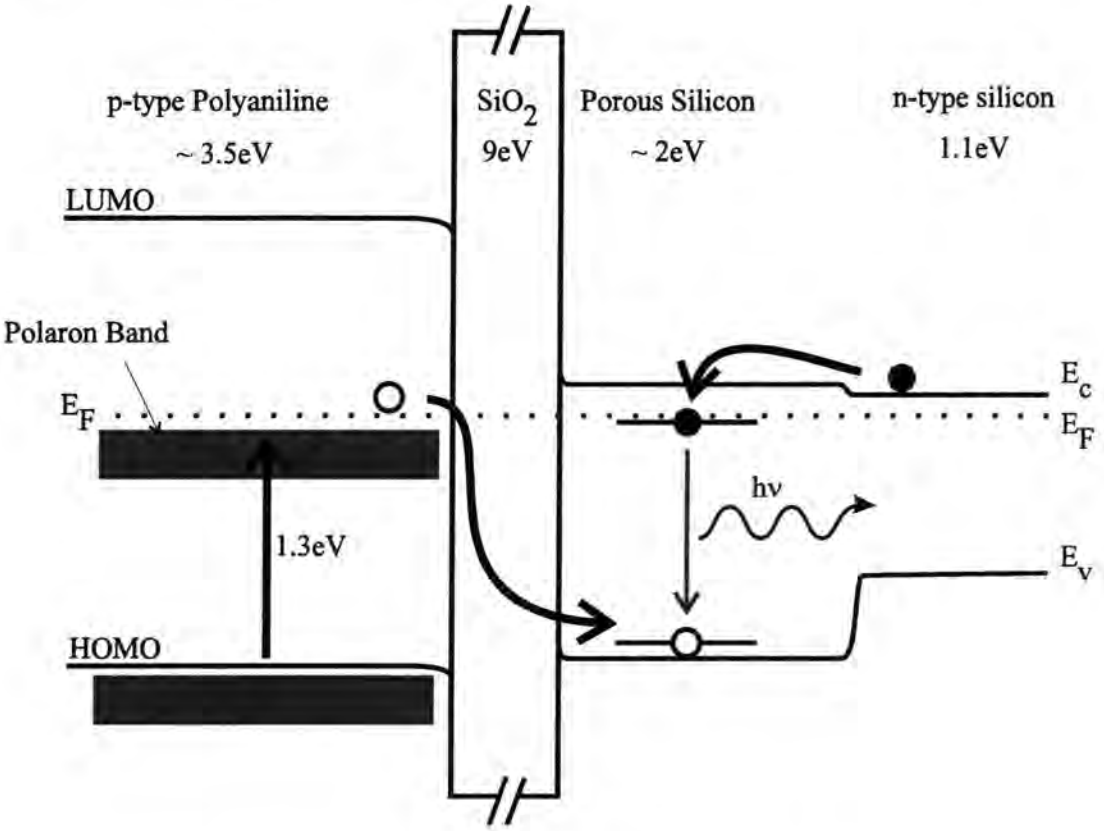

Figure 45: Diagram of junction energy levels

5.6. Conclusions

A contacting scheme has been developed for n-type porous silicon using p-type conducting polyaniline which has the I-V characteristics of a Schottky junction. The structure emits visible electroluminescence when forward biased.

Our fitting gives a barrier height of around 0.8 eV for the device. This is much less than the expected 1.3 eV in the diagram. This indicates tunnelling through states in the oxide layer is the current transport mechanism.

6. PHOTOLUMINESCENCE OF THE CdTe LAYER OF CdS/CdTe THIN FILM SOLAR CELLS

6.1. Summary

The structures we report here consist of indium tin oxide (ITO) coated glass and two subsequent layers; 500 nm of CdS and approximately 5 μm of CdTe. The as grown cells have a photovoltaic efficiency of η= 0.8%. Following deposition of $CdCl_2$ and annealing in air, the efficiency increases to around 10%. A study of the cells is made by examining the variation in the photoluminescence from the CdTe with laser power and sample temperature for an as grown cell, an air annealed cell and a cell which has undergone the $CdCl_2$ treatment. The observed emissions are analysed and the possible origins are discussed.

6.2. Introduction

6.2.1. The Potential for Power Generation

The sun provides approximately 1.35 kWm^{-2} of power in the form of electromagnetic radiation at the average distance of the Earth from the Sun. On Earth at the equator the figure is over 1kWm^{-2} in peak conditions. However, the average for the whole of the Earth's surface over a year is lowered to 340 Wm^{-2} due to absorption by the atmosphere and the rotation of the Earth. Over the total surface of the Earth, this is equivalent to the output of over 4 million 10 gigawatt power stations, and is about 20,000 times the estimated current power usage of the planet[95]. Obviously it is

impractical to cover the entire planet in solar cells, but one 170 metre by 170 metre "power plant", which could easily be built in remote areas, would produce an average over one year of approximately 1 MW if just 10% efficient.

A major difficulty with solar power as a mainstream source is continuity throughout day and night and seasonal changes. Possible solutions include electrolysing water to produce hydrogen and oxygen which could be stored for later use, or even using superconducting magnets to store energy in magnetic fields.

Although solar energy may not be a final solution to energy needs, it is a clean and safe method of generating power. It could form a significant source of power in the next century.

6.2.2. Economic Considerations of Cell Production

There are two basic routes towards the goal of harnessing solar energy as an economically viable power source, both of which are being developed at this time for use in different applications and conditions.

The first is "high cost" and uses the best materials and technology available to obtain the cells with very high efficiencies. Clearly the cells will be very expensive to produce. This type is vital for use in mass-critical situations, such as space vehicles. They can also be used in so called "concentrator" systems, where a collecting lens or mirror focuses light from a large area onto a smaller area solar cell.

The second is "low cost" and aims to produce large quantities of cheap, mass produced, solar energy systems. The main area of application is in large area flat panel solar cells for more general terrestrial use.

CdS/CdTe solar cells are of the low cost type and offer a realistic possibility of achieving the goal of viable photovoltaic energy production. Ultimately it is hoped that the most expensive part of a CdS/CdTe solar cell will be the glass substrate.

Currently, the best high cost cells have efficiencies are approaching 30%, whereas commercial CdS/CdTe solar cells of the low cost type are already available with efficiencies of around 7.5%.

6.2.3. Fundamentals of Photovoltaic Power Generation

A solar cell converts electromagnetic energy into electrical energy. It creates electrons and holes in a semiconductor by absorbing photons. The electrons and holes are separated by an internal electric field built into the semiconductor and the two particles are ejected from the material with a potential difference which can be used to do work in an external circuit.

The solar cell must have a region where "band bending" occurs, which gives rise to the internal electric field in the material. This can be caused by a Schottky barrier or by a p-n junction. Only the latter variety will be dealt with here.

When two semiconducting materials, one of n- type and one of p-type, are brought together, the electrons inside the material initially have two different Fermi energies (an energy state at the Fermi energy has a 50% chance of being occupied), measured with respect to the vacuum energy level (the energy at which the electron is free to leave the material altogether). On joining the materials together and letting them equilibrate, the Fermi level will eventually become a constant throughout the system. For this to happen, the conduction and valence bands must bend, as in Figure 46.

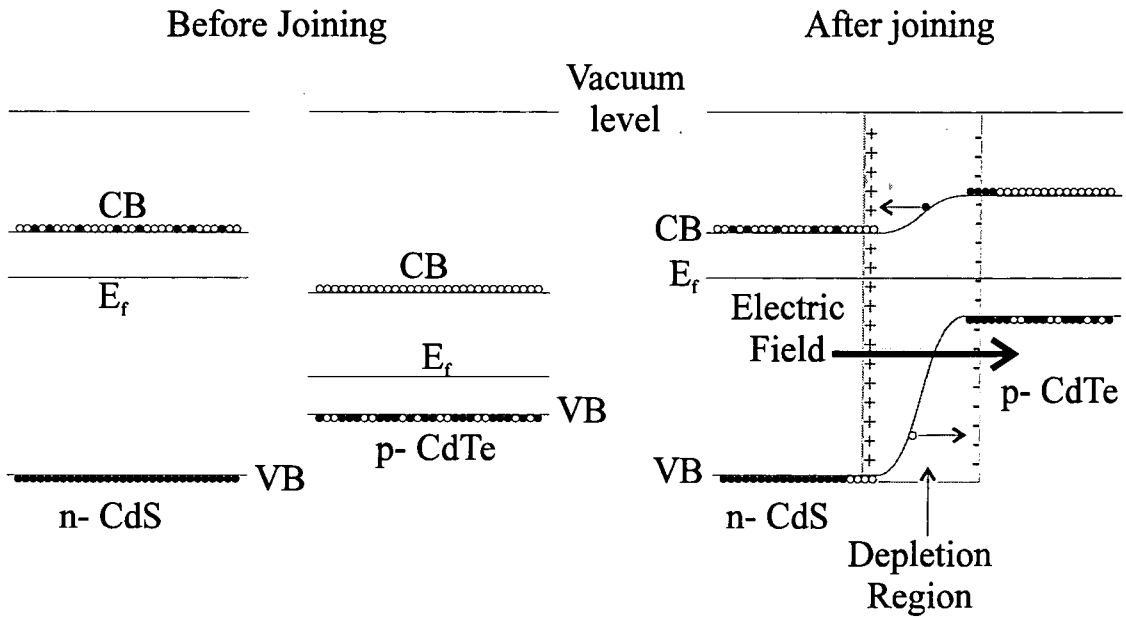

Figure 46: Creation of in built electric field

In the n- type material, some of the large number of electrons diffuse into the p-type region, leaving behind the positively charged ionised donors. Similarly, the some of the excess of holes in the p- type material diffuse into the n- type region, leaving behind negatively charged ionised acceptors.

This means there is now an net positive charge on the n- type side of the junction, produced by the positivly charged ionised donors plus the holes, and an overall negative charge on the p-type side of the junction which is composed of the

negatively charged ionised acceptors and electrons. Therefore an electric field exists across the depletion region which is directed from the n-type side to the p- type side. Now, when an electron and a hole are created by the absorption of a photon in the vicinity of the depletion region, the pair will be separated. The electron will move towards the n-type region, and the hole to the p-type region. The pair can leave the device with the electron higher in energy than the hole. This creates a potential difference between the two terminals of the device which can be used to do work.

The cell must consist of two layers; an absorber layer, which absorbs the majority of the incoming radiation and a window layer (or collector layer), which transmits most of the radiation through to the absorber.

The cell materials are chosen so that the majority of photons entering the device through the window layer have an energy lower than the window layer band gap and will be transmitted to the absorber layer where they create a photovoltage. This is shown in Figure 47 for the CdS/CdTe system.

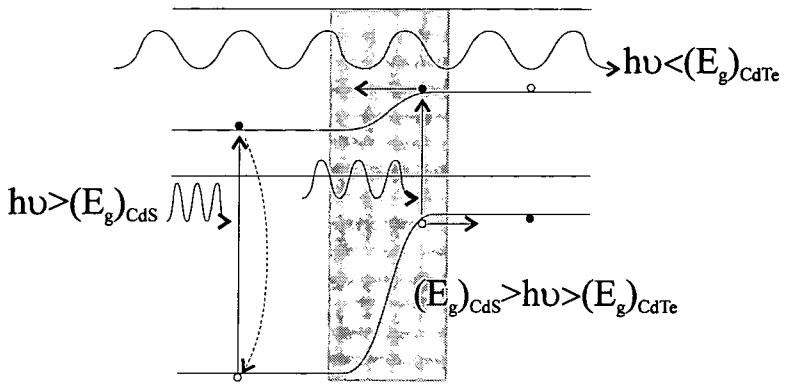

Figure 47: Absorption of photons in a CdS/CdTe solar cell

The output voltage and current of the cell depend on the conditions of use. The voltage can vary from zero up to a maximum voltage, V_{oc} (the open circuit voltage), when the cell is not attached to an external circuit and no current is being drawn, and the current varies up to a maximum current I_{sc} (the short circuit current) when the cell

is shorted and no voltage is being produced. The maximum power that can be drawn is P_{max}. The values are shown in Figure 48. The fill factor, (FF), is the ratio of the area of the maximum power rectangle to the area of an 100% efficient cell:

$$FF = \frac{V_{\max} . I_{\max}}{V_{oc} . I_{sc}}$$

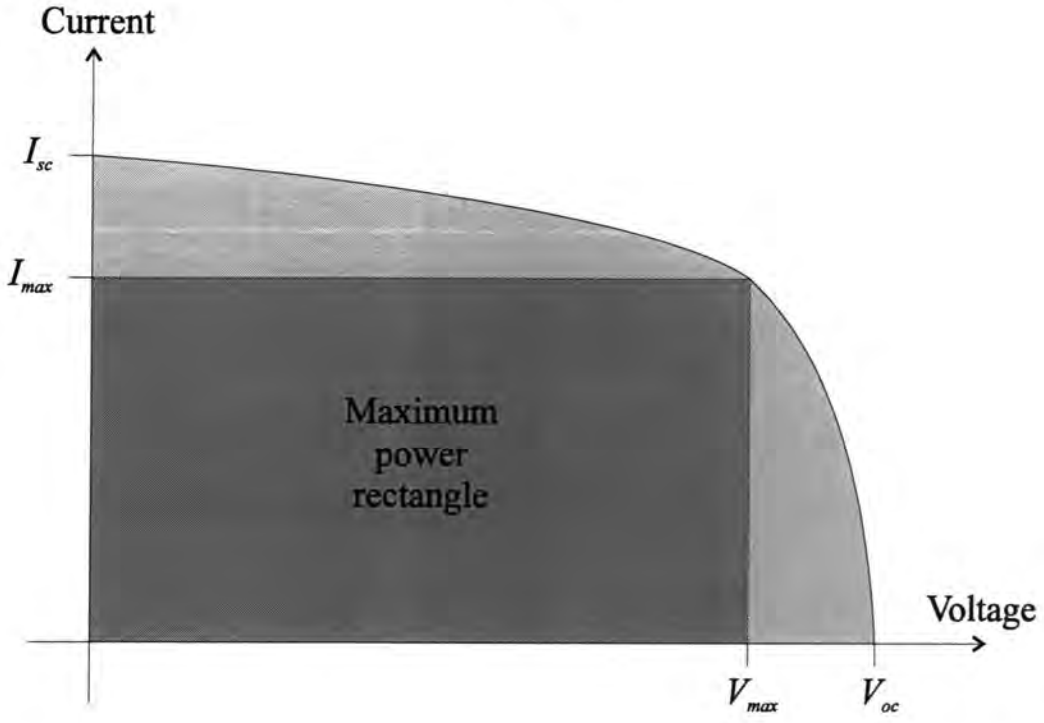

Figure 48: Cell power performance and output values

6.2.4. The Solar Spectrum

A solar cell must be carefully designed to maximise the power output. The fundamental constraint on energy production is the amount of solar power reaching the cell and the spectral distribution of that electromagnetic radiation.

The output of the sun can be approximated to a black body spectrum with a temperature of around 5800K. There are emission lines in this spectrum which complicate it slightly, but for most calculations it is taken as being a classical black body.

Generally cell efficiency will be quoted at a specific Air Mass (AM) number, where the number gives an indication as to distance through the atmosphere that the sun's rays must travel to reach the cell. AM0 is the solar spectrum outside the atmosphere and AM1 is defined as being the spectrum after travelling the path length through the atmosphere at the equator. AM1.5 is the path length at a latitude of 48.19° (approximately that of Great Britain). See Hulstrom et al[96], for example, for further details including actual data sets. Clearly, the larger the AM number the less power reaches the cell and the lower the overall output will be.

However overall cell efficiency can vary with AM number also, as the distribution of the solar spectrum is altered by the extra absorption occurring in the ultraviolet and at certain energies in the infra red (due to water vapour and carbon dioxide for instance). This will lower the average energy of the solar spectrum.

6.2.5. Efficiencies

The main characteristic of the cell is the energy gap of the absorber layer. The higher it is the higher V_{oc} becomes, but more photons are not absorbed and pass straight through the cell so lowering I_{sc}. Lowering the energy gap will increase the number of photons absorbed and so increase I_{sc} by generating more electrons and holes, but the side effect of this is to lower V_{oc} and cause more energy to be lost as heat during the process of thermalising carriers to the band edges after absorption.

So a play off between the two effects is required, and calculations by De Vos et al[97] show that the calculated maximum efficiency for a system collecting energy from a 5762 K black body, consisting of an absorber material with a band gap 1.28 eV

would have $\eta = 30.2\%$, $V_{oc} = 1012$ mV, $I_{sc} = 33.8$ mA/cm^2 and $FF = 88.3\%$. Using an AM1.5 spectrum, slightly higher efficiencies of around 31% are obtained.

Cadmium telluride has a band gap of around 1.45 eV and is therefore a near ideal material. The window layer should be as transparent as possible. Cadmium sulfide, with a band gap of 2.5 eV only absorbs the blue part of the spectrum so losing only a small proportion of solar photons.

As CdTe is also a direct gap material, it has a high absorption coefficient for above band gap energies, typically 5 x 10^4 cm^{-1}[98]. This means only a thin layer of CdTe ≈2 μm thick is needed to collect virtually all the incident light. This compares favourably to indirect materials such as silicon which require some 20μm. This means more carriers will be created near the built in electric field of the device.

The theoretical maximum efficiency for a CdS/CdTe solar cell, under illumination from a black body has been calculated by to be 29.7%, with $V_{oc} = 1173$ mV, $I_{sc} = 28.2$ mA/cm^2 and $FF = 89.6\%$.[99]

6.2.6. History

Since the first use of CdTe as an absorber in the 1960's, many attempts have been made at utilising the material for the creation of an efficient solar cell. Initially, Vodakov et al[100] and Nikolaev[101] used shallow p-n homojunctions to obtain efficiencies of 4 to 6%. Eventually CdS came to be used as the n-type window layer, which solved the problems of forming a thin layer of highly conducting window material.

The world record for the highest measured efficiency of CdS/CdTe solar cells has been increasing steadily over the past few years. In 1991, Chu et al[102] reported a 1

cm^{-2} area cell with an efficiency of 13.4% and then the same group improved upon this in 1993, demonstrating a similar cell with an efficiency of 15.8%[103]. This is still some way below the theoretical maximum efficiency of 29.8%. It should be noted that the absolute maximum for any single stage solar cell is 44%[104]. Higher efficiencies can be achieved by using a second cell to use light which is transmitted through the first. These tandem cells have achieved efficiencies of up to 30.3%[105].

6.2.7. The Effect of the $CdCl_2$ Anneal

As mentioned above, the effect of the $CdCl_2$ annealing process vastly improves the efficiency of these cells as a result of V_{oc}, I_{sc}, and FF also increasing. Table 6.1 gives values for the cells studied in this chapter, before and after treatment and also by an anneal in air at AM1.5.

Cell	V_{oc} (V)	I_{sc} ($mAcm^{-2}$)	FF	η(%)
as deposited	0.55	17	33	1.5
air annealed	0.55	15	39	3.6
$CdCl_2$ treated	0.68	26.7	56.7	10.0

Table 6.1: Cell characteristics

Performing electron microscopy on the cells shows that the effects of the anneal are an increase in the grain size, a decrease in the inhomogeneity across the cell and an increase in the crystal quality (a lower number of defects) at the interface. The purpose of this study is to attempt to study what changes occur in the electronic structure of the material.

There are three acceptable explanations for the increase in the cell efficiency. First a shallow Cl-related acceptor (V_{Cd}-$2Cl_{Te}$) or substitutional O_{Te} causes the CdTe

material to become p-type, increasing in built electric field and V_{oc}, secondly an oxygen related centre helps by passivating the grain boundaries, or thirdly simple grain growth process creates a more uniform cell with less short circuits.

See the review paper by Basol[106] for further details.

6.2.8. Principle of Experiments

The near band edge photoluminescence of semiconductors can give important information for the evaluation of the quality and composition of materials. By studying the dependence of the intensity of the various lines on the incident laser power and sample temperature, it is often possible to deduce the physical nature and chemical origin of those emissions, usually from a range of differently treated samples. See Giles-Taylor et al[107] for such an analysis.

As was described in section 2.5, photoluminescence can be used to measure the electronic states of a crystal. The electrons and holes created by the incident photons are free to move around the crystal until they recombine emitting a outgoing photon, or until a non-radiative process occurs. The immediate surroundings of the electron and hole when recombination takes place affects the energy of the outgoing photon, and by studying these photons, information concerning the internal electronic nature of the material can be obtained.

One commonly used spectral region is the near band edge photoluminescence. Before recombination, electrons and holes may undergo the process of becoming bound into an exciton and then that exciton may in turn become bound at impurity sites. When the exciton collapses, emitting light, the energy separation from the band

edge is only small due to the slight nature of the perturbation to the lattice but it is related to the nature of the binding impurity.

However, if non-radiative pathways in the crystal are of a high enough concentration, and the average time before non-radiative recombination is smaller than the average time before exciton formation, or if a species exists in the crystal which can dissociate excitons, the excitonic luminescence can be small or even non-existent. This is often considered to be the case in polycrystalline materials. In group IV and III-V material, it is known that in order to get significant luminescence in the near band edge region, it is generally necessary to have reasonable quality material. Free carriers still form excitons in low quality crystals, but the excitons are destroyed by interactions with centres in the crystal which have large localised electric fields which split up the lightly bound excitons.

This is not the case in II-VI semiconductors though, as we can clearly observe near band edge photoluminescence from high polycrystalline material.

6.3. Experimental Details

6.3.1. Growth and Production

The samples, shown in Figure 49, were grown using Close Space Sublimation (CSS) Technique by ANTEC, Germany. Firstly, a thin layer of tin oxide was put down to help stop diffusion of indium from the ITO layer into the CdS. Then 500 nm of polycrystalline cadmium sulfide was evaporated on, followed by 5 μm of cadmium telluride.

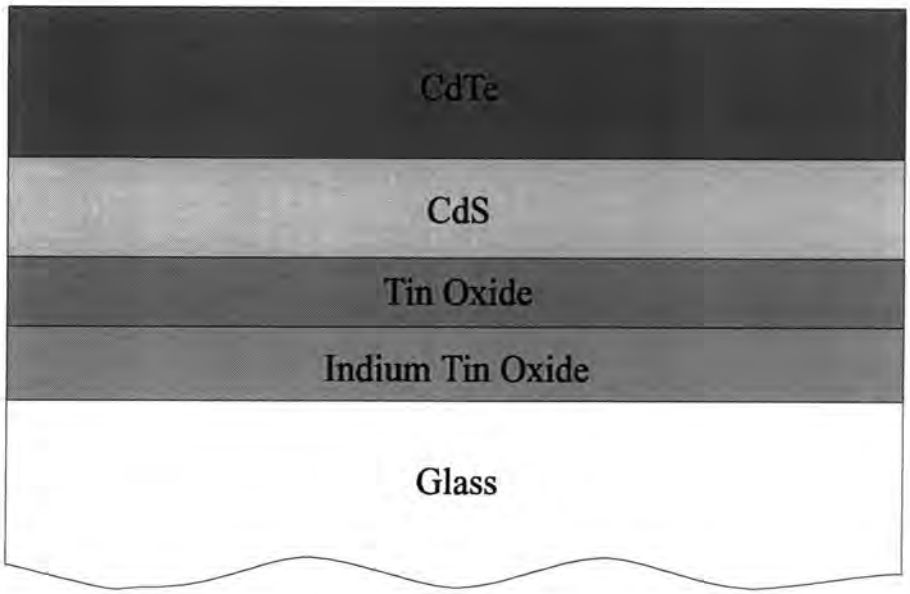

Figure 49: CdS/CdTe solar cell diagram

Three different cells were produced. In addition to the as grown cell, one cell was treated by annealing in air at 400 °C and one was annealed in air at 400 °C after the evaporation of $CdCl_2$.

6.3.2. Optical Layout

The effect of two different parameters on the photoluminescence of the CdTe layer were investigated in the experiments reported here. The effect of incident laser power and the temperature of the sample on the photoluminescence were studied.

The sample was mounted in a Helium Refrigerator cryostat and the sample temperature lowered to 10 K and allowed to equilibrate before any spectra were recorded.

For all of the measurements made, the 488.0 nm line of an Argon Ion laser was selected using a line filter, and OG515 filter used to reject the scattered laser light from the spectrometer. Power levels were checked regularly to ensure that the laser

had not drifted away from set levels. The maximum power density used for these measurements was of the order of 1 Wcm^{-2}.

Laser Power Density variation

To vary the laser power striking the CdTe, it was necessary to use a neutral density filter wheel which allowed the power to be varied over nearly three orders of magnitude. This consisted of two circular discs one behind the other, each disc containing 6 different neutral density filters, mounted in a ring. The first disc contained filters with neutral densities of nominally 0.04, 0.5, 1.0, 1.5, 2.0 and 2.5 with the second wheel having filters of 0.04, 0.1, 0.2, 0.3, 0.4 and 0.5. The filter absorbencies were checked by performing absorption spectra on the individual filters in a Perkin-Elmer spectrophotometer. It was found that several filters varied from the printed figures and the measured values were used instead.

This enables any absorption of the laser power between 0.08 and 3.0 (which corresponds to a transmission of the laser light striking the filters from 83% down to 0.1%). The photoluminescence entering the monochromator was maximised on the diode array by optimising the position of the collecting lens first without the filter wheel in place, and then with the filter wheel in place at the highest transmission, to ensure none of the signal was wasted and a comparison between spectra recorded from different samples could be made.

Temperature Variation

The temperature variation of the photoluminescence was undertaken in a similar manner. After lowering the sample to 10 K, the photoluminescence signal was maximised. After spectra had been recorded at a particular temperature, the set point

would be altered and 20 minutes allowed after the target temperature had been reached to ensure the sample had attained equilibrium.

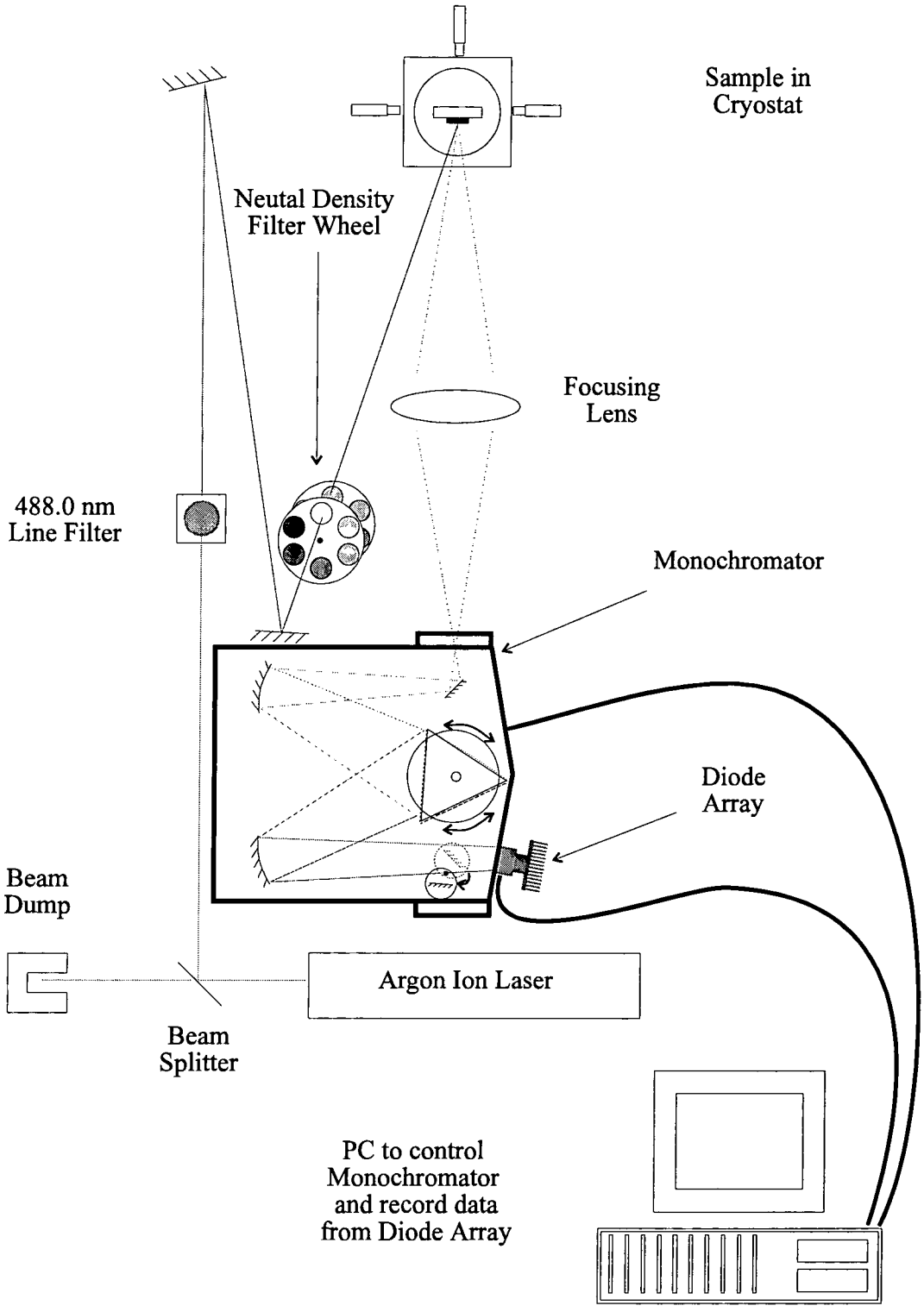

Figure 50: Experimental layout for photoluminescence measurements

6.4. Results

6.4.1. Photoluminescence

The photoluminescence of cadmium telluride has been studied for some years. Good quality material with high resistivity was desirable for use as a material in gamma radiation detectors and the electrical and optical properties of crystals were studied in the 1970's for this purpose[108,109], though the properties of such materials will be very different from that examined here. Photoluminescence from high quality crystals generally only shows near band edge emissions and identification of shallow impurities is possible by high resolution spectroscopy[110,111] of the near band edge region.

Due to the nature of deposition, the material will be polycrystalline and electron microscopy shows that it consists of a large numbers of grains of differing sizes[112]. As grain boundaries often provide an effective route for non-radiative processes, it might be expected that polycrystalline CdTe would not be luminescent. However studies have clearly observed photoluminescence in polycrystalline CdTe[113], even up to room temperatures[114].

One effect of having a polycrystalline system is that photoluminescence emission lines are broadened by the variety of sites that can exist in the material. Even using a laser spot of 1 mm^2 area will probe 10000 10μm grains, each having different dislocation densities, surface areas and impurity concentrations. This means it is no longer possible to observe individual homogenously broadened exciton lines and the lines overlap and merge into one large peak. An attempt was made to analyse spectra using computer software but results proved unreliable so the exciton peak was treated simply as one line for the purposes of analysis.

As can be seen in Figure 51, our material shows three main bands.

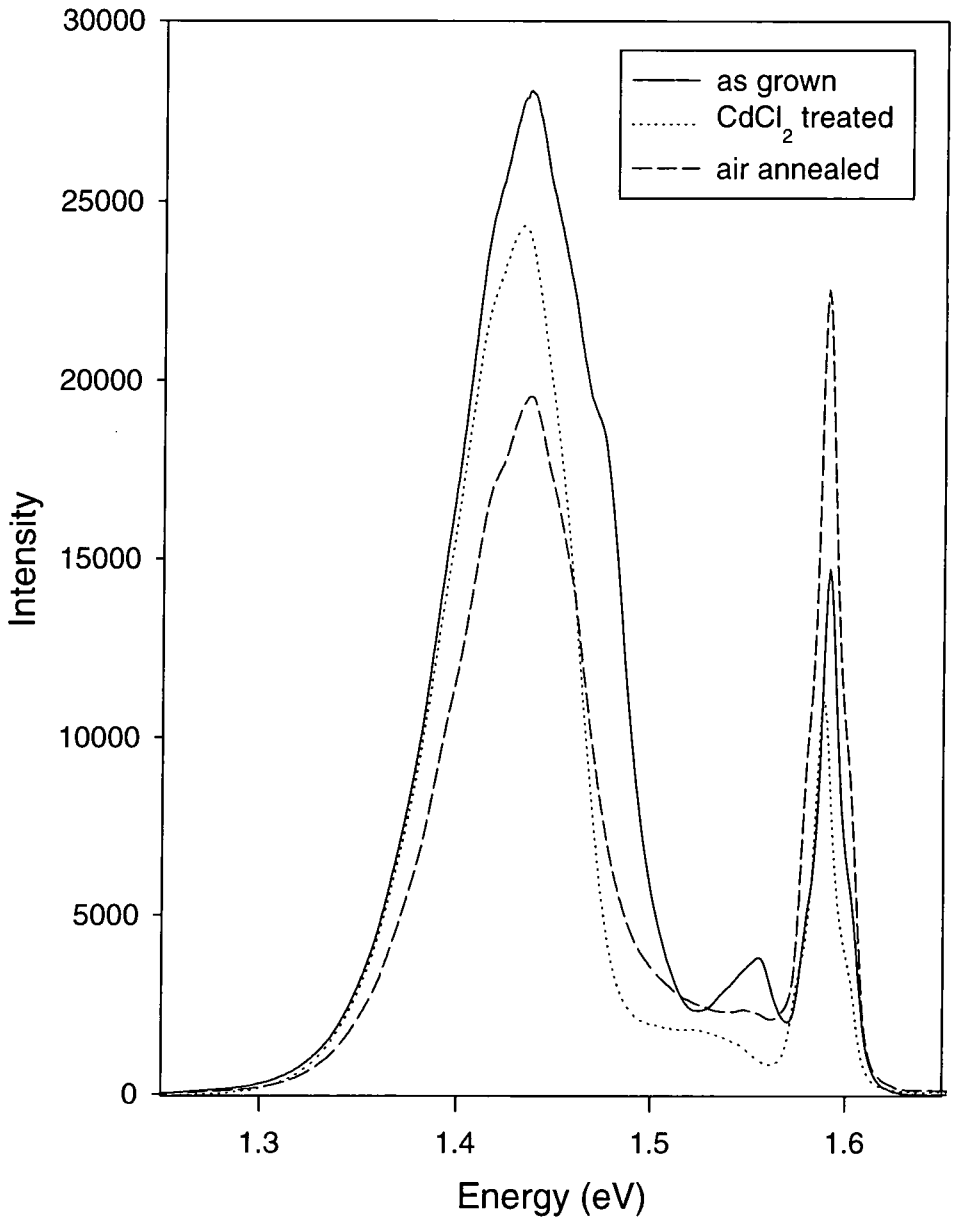

Figure 51: Sample spectra at 10K

The highest energy band is around 1.59 eV, which is near the band gap of cadmium telluride (1.606 eV at 10K). Hence the luminescent centres responsible are assumed to be excitons localised at donors or acceptors. It can be noted that the peak shifts to

slightly lower energies after the $CdCl_2$ anneal, in agreement with V_{oc} increasing and the material becoming p- type[115]. The excitonic band has often been used as an indicator of crystal quality, usually measured relative to the 1.45 eV band[116,117,118]. However, Bubulac et al[119] report the observation that the excitonic emission seems to arise from regions of the samples associated with grain boundaries and the deep level emission from the centre of grains, suggesting that in polycrystalline CdTe this ratio cannot be used as a crystal quality factor. There is certainly no significant change in the ratio of the peak areas in these samples. If anything, the $CdCl_2$ treated sample which was assumed to have the best crystal structure has the worst ratio.

It is also important that the power levels do not alter between measurements for the reasons discussed in the next section.

The largest emission is the broad feature which extends from 1.5 eV down to 1.3 eV. The centre responsible for this emission has proved elusive to conclusively identify, but it seems generally accepted that it involves deep acceptor like levels associated with a complex centre such as $(V_{Cd}X_{Te})$[120], where X is a donor atom such as chlorine. This level has been assigned a binding energy of around 0.14 eV by various authors[121,122], which would be in agreement with our data It also been suggested that the luminescent species is located in the bulk of the material, as opposed to grain boundaries[123]. Many differing results have been reported together with proposed schemes to explain the data, including a level in the crystal being caused by some form of defect in the cadmium crystal[124,125] or phonon replicas of an unknown emission[126]. Norris has published several papers[127,128,129] refuting the claim that cadmium vacancies are involved at all.

There is also another weaker band, around 1.55 eV, which can be most easily seen in the as grown material. Many authors have measured emissions at this energy similar

to that here. Figueroa et al have assigned this to a cadmium vacancy[130] whilst Akimoto ascribed it to a oxygen related donor acceptor pair[131,132].

6.4.2. Laser Intensity Variation

It has been known for some time that the power dependence of emission lines can be fitted by using the following relationship between the peak intensity (I_{peak}) and the incident laser intensity (I_{laser}):

$$I_{peak} \propto I_{laser}^{k}$$

where k is a number between zero and two. k can be measured by fitting a straight line to a $\log(I_{peak})$ against $\log(I_{laser})$ graph and calculating the slope. For excitonic processes, k is between one and two, and for free to bound and donor acceptor pairs, k is less than one. Two different models by Taguchi et al[133] and Cooper et al[134] attempt to explain the observations that bound exciton emissions have k greater than one.

Taguchi et al explained the superlinearity as arising from the increase in the density of neutral impurities as a result of photoexcited carriers and predicted that k=1 for free excitons and k=1.5 for bound excitons. However, if photons with the exact energy to create a bound exciton are used, it is found k=1.

Cooper et al solved this problem by suggesting that as the rate of formation of excitons should be proportional to the product of the concentration of electrons and the concentration of holes, the emission should have k=2. If the photons were resonant with the excitons in energy though, the excitons would form directly from the photon and give k=1. Free exciton emission and donor acceptor emission would also be expected to have k=1. However, experiments tend to give k's which are non-

integers and in the case of non-resonant exciton formation gives k smaller than two. See for Lee et al[135], Gold et al[136] or Aguilar Hernandez et al[137] for other examples of such fits.

It has also been noted that when varying the exciting laser power over more than two orders of magnitude, donor-acceptor and free to bound emissions tend to deviate from $I_{peak} \propto I_{laser}^{k}$.

To explain all of the observed trends and values, Schmidt et al[138,139] have been able to explain all observed features of power dependence experiments by using a set of coupled differential equations.

Figure 52 shows the data recorded for the excitonic emission centred around 1.59 eV and Figure 53 shows the data for the deep level emission from the back surface of the samples examined. It can be clearly seen that the two bands have two distinctly different slopes. The results are summarised in Table 6.2.

The spectra were fed into PeakFit, which fits data to a specific model of peaks. The intensity of a line is related to the total area under a peak, and values of the best fits were calculated by the software.

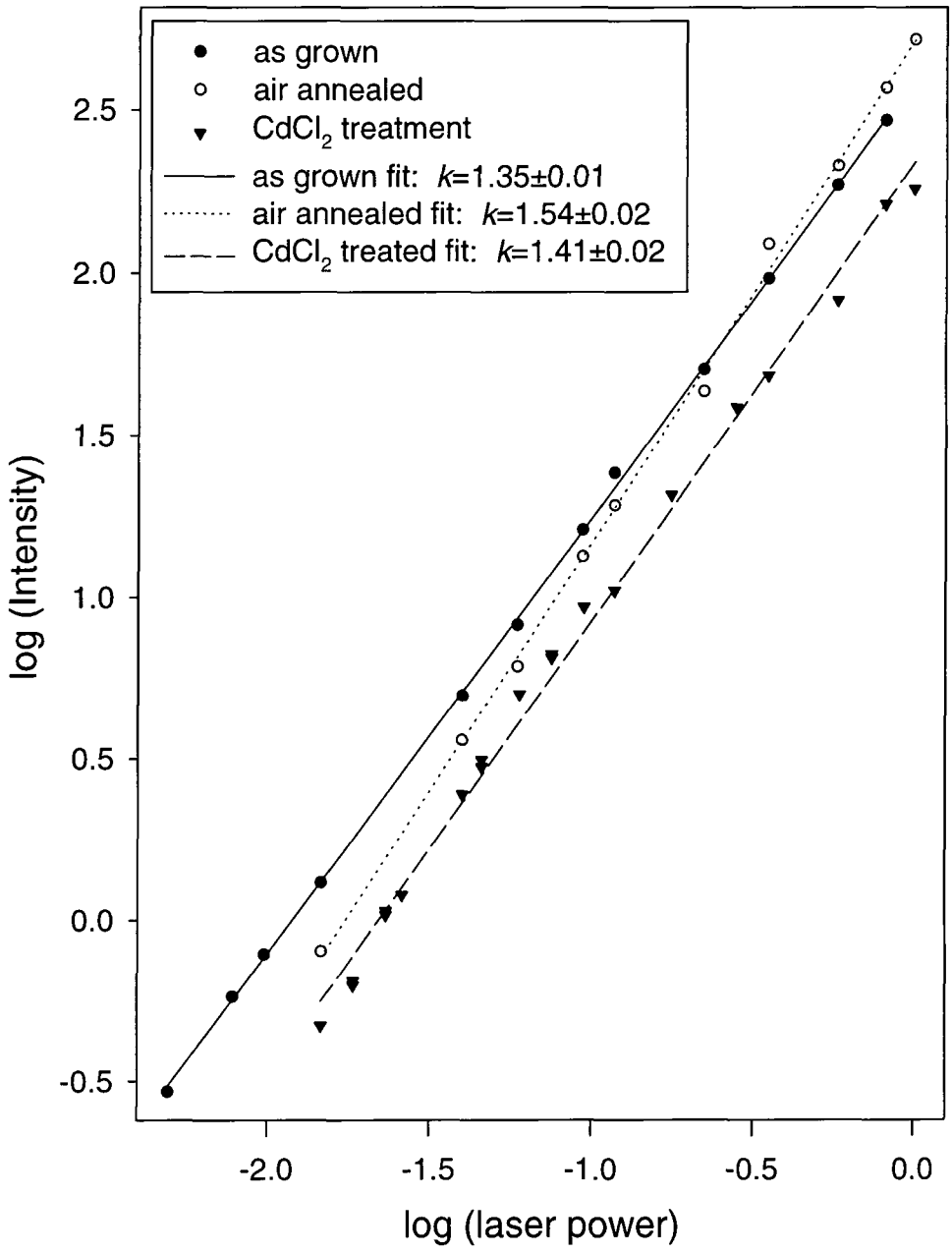

Figure 52: Power dependence of 1.59 eV emissions from samples

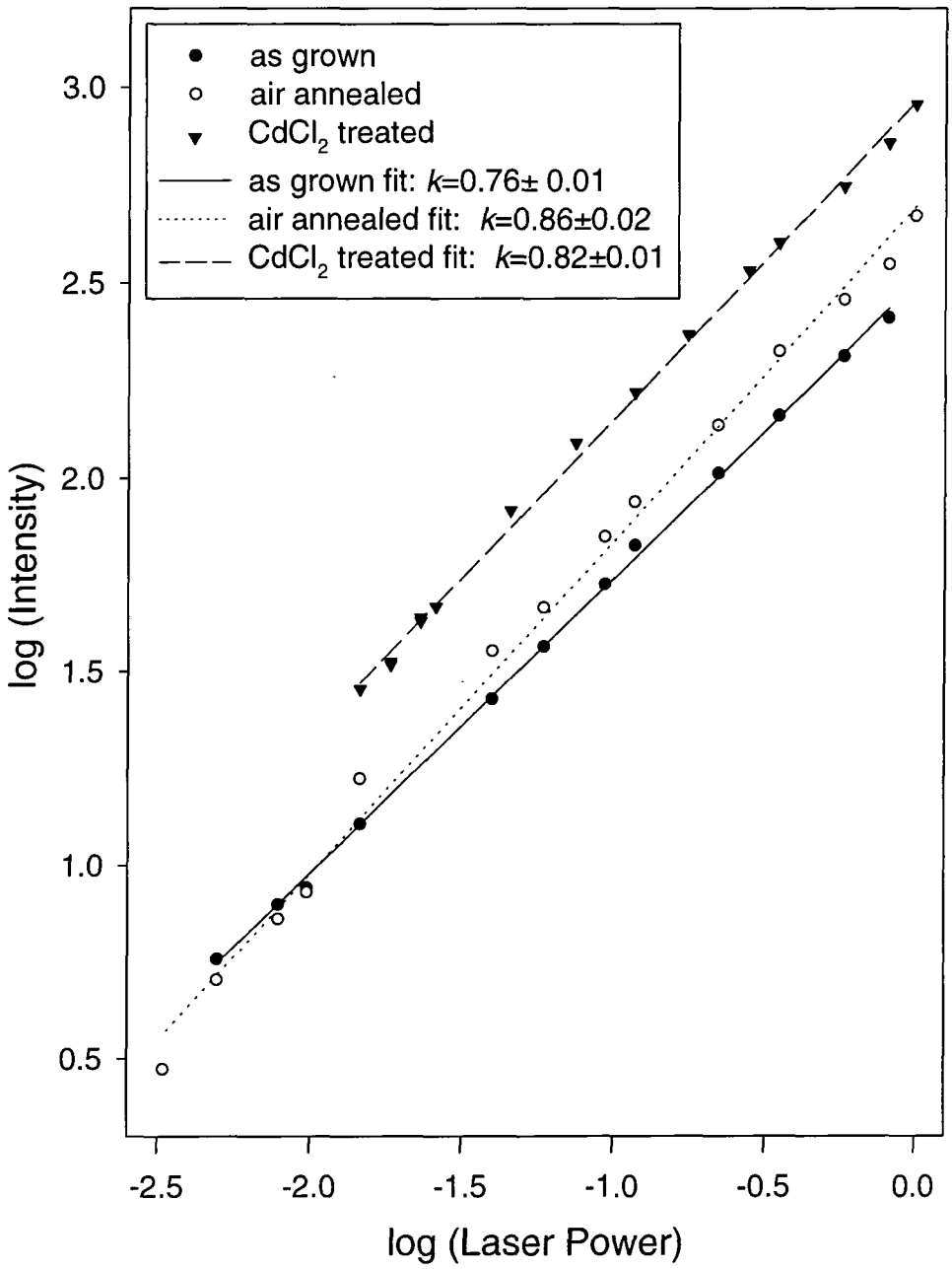

Figure 53: Power dependence of 1.45 eV emissions from samples

Cell	k for 1.59 eV emission	k for 1.45 eV emission
as deposited	1.35±0.01	0.76±0.01
air annealed	1.54±0.02	0.86±0.02
CdCl2 treated	1.41±0.02	0.82±0.01

Table 6.2: Summary of k values for different samples and emissions

It can be seen that this data confirms the association of the region of spectra around 1.6 eV to excitonic centres as described in previous work[140,141]. The superlinear fit to the sample data is a clear indication that the polycrystalline material does allow the existence of excitonic structures. This is contrary to what might be expected in a polycrystalline material, where the high perturbation to the crystal potential caused by the presence of grain boundaries and dislocations cause excitons to be dissociated. It is also possible to identify the deep level emission as being a free to bound transition, since the values are in good agreement with the predicted k of around 0.7. This value excludes the possibility of the transition being some form of donor-acceptor pair, since the k for this type of transition is expected to be about 0.2. Given it is expected to be an acceptor like deep level, this band must result from a free electron recombining at this centre. Further, the peak does not show any blue shift or widening with increasing laser power which is what would be expected of a donor-acceptor pair.

6.4.3. Temperature variation

Due to the low intensities involved, and the thermal quenching which takes place, generally the photoluminescence from samples was only measurable for temperatures of up to around 100K. The results from the three different samples are shown in

Figure 54, Figure 55 and Figure 56. A model, following Bimberg et al[142], was used to fit the data and obtain estimates for the exciton binding energy, E_1, and the impurity binding energy, E_2. By assuming that an exciton bound to an impurity has two main routes of dissociation, it is possible to fit the data using:

$$I(T) = \frac{I(0)}{\left(1 + C_1 \exp\left(\frac{-E_1}{kT}\right) + C_2 \exp\left(\frac{-E_2}{kT}\right)\right)}$$

where $I(T)$ is the intensity at a particular temperature, $I(0)$ is the intensity at absolute zero, C_1 and C_2 are related to the degeneracy of the final states for the two processes and E_1 and E_2 are the excitation energies for the two processes.

The results are summarised in Table 6.3.

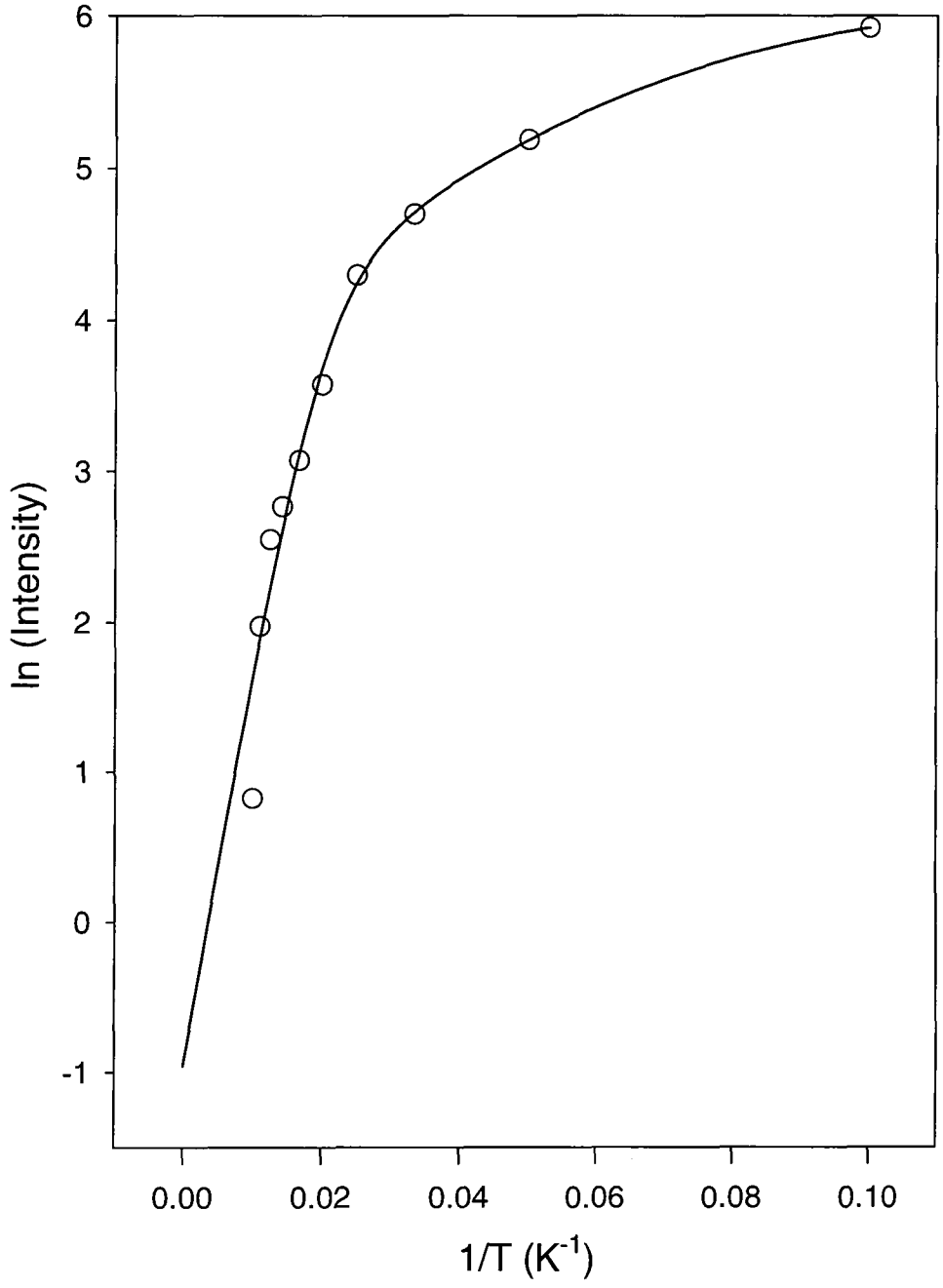

Figure 54: Temperature dependence of excitonic emission from as grown sample

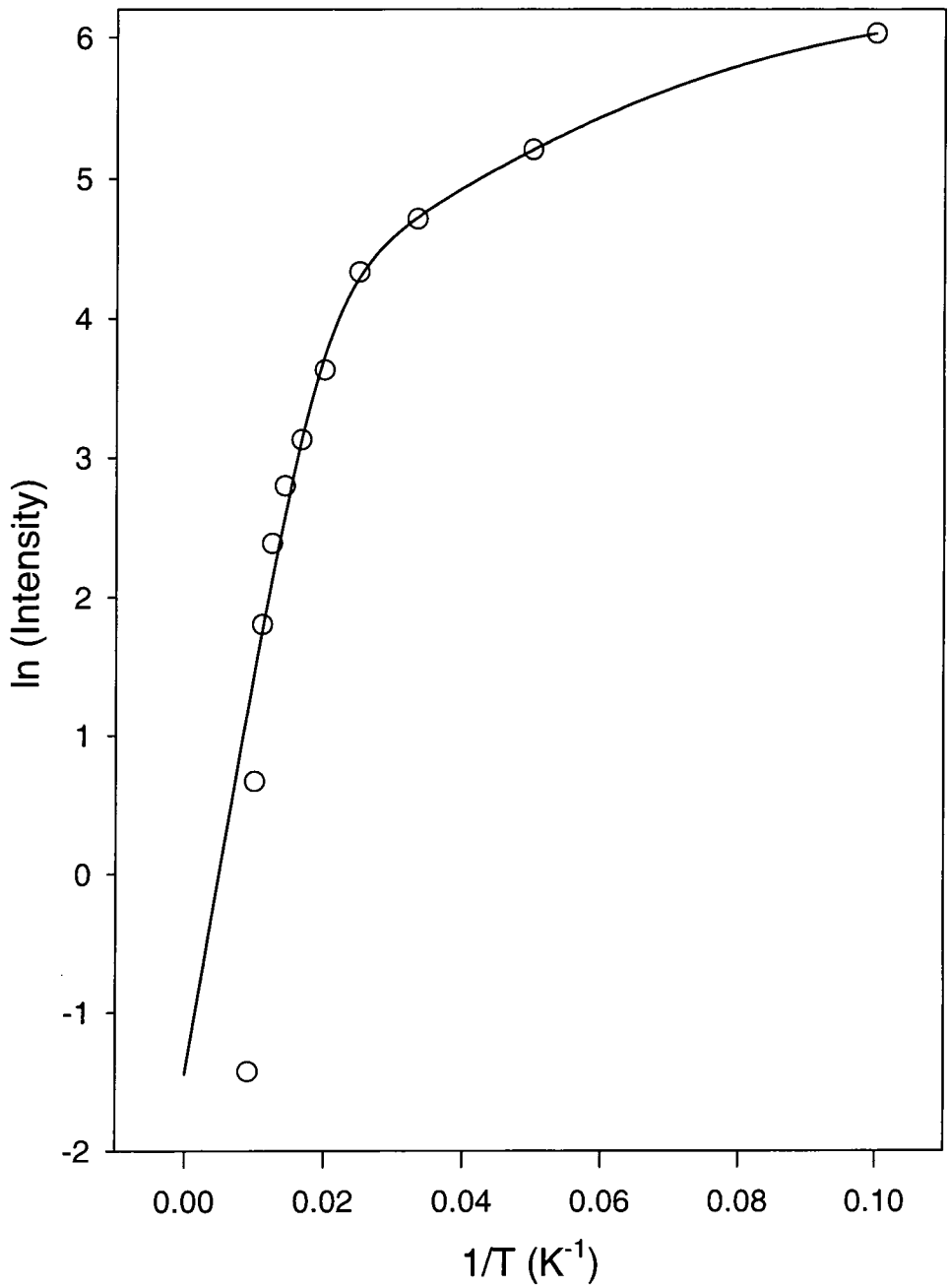

Figure 55: Temperature dependence of excitonic emission from air annealed sample

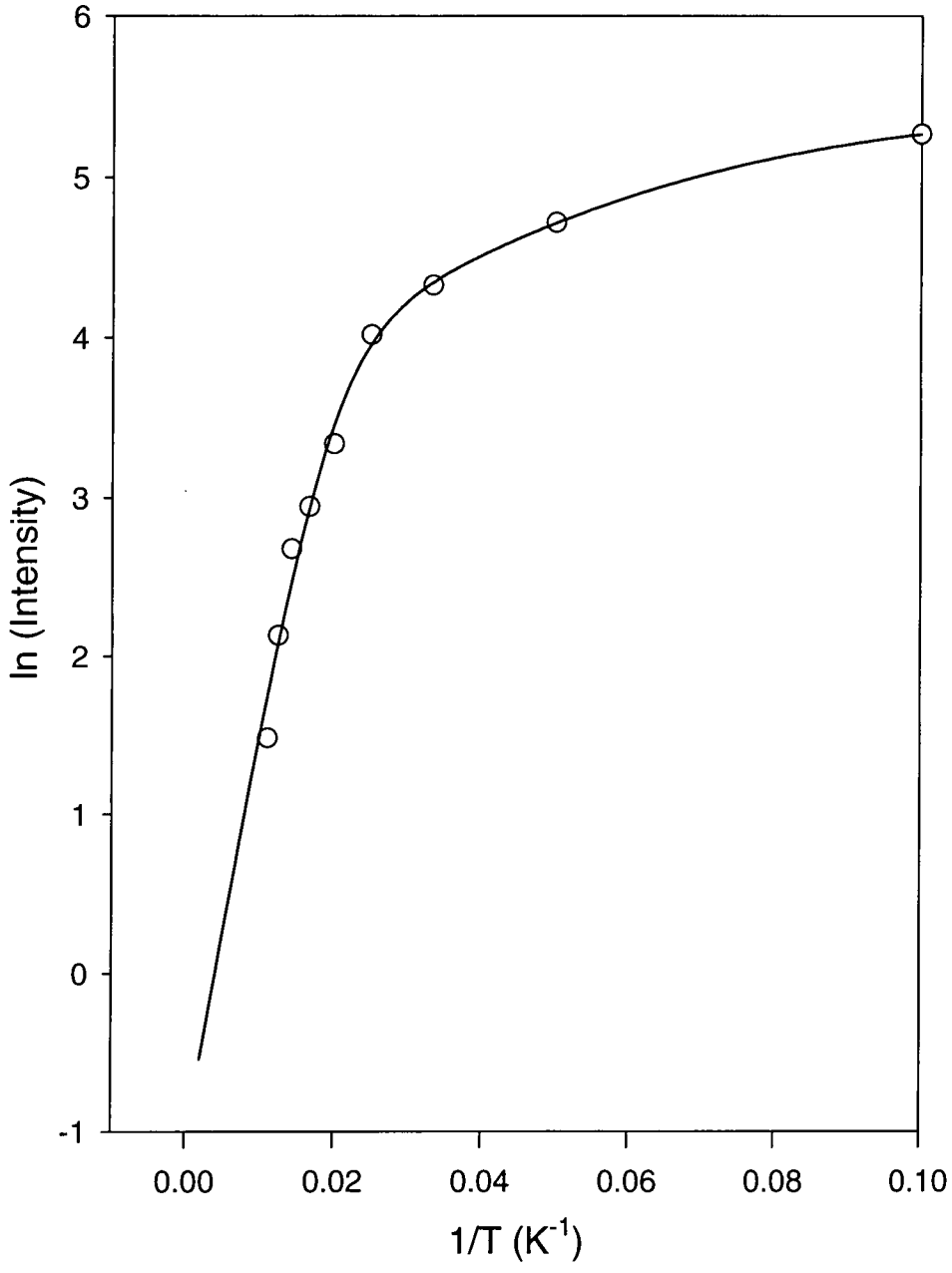

Figure 56: Temperature dependence of excitonic emission from $CdCl_2$ treated sample

Cell	E_1 (meV)	C_1	E_2 (meV)	C_2
as deposited	3.3±0.5	11±2	23±3	1184±660
air annealed	3.3±0.3	13±1	26±3	2250±1220
$CdCl_2$ treated	3.0±0.8	6±1	23±4	663±468

Table 6.3: Summary of fitting results for temperature dependent data

It can be seen that there is no statistically measurable difference between the samples in E_1 and E_2. In the original paper by Bimberg, intensity data is interpreted as resulting from a species which can has two routes of dissociation. The neutral impurity bound exciton can dissociate to an free exciton where E_1 is interpreted as the binding energy of the exciton to the impurity or the neutral impurity can be ionised where E_2 is the donor or acceptor binding energy.

However, this relies on the dissociated species no longer contributing to the luminescence as in high quality material where the free exciton formation will result in a larger free exciton emission. This problem means that E_1 and E_2 must be interpreted in a different manner.

E_1 is the energy associated with the dissociation of the free exciton into a free electron and hole. The exciton binding energy in cadmium telluride has been measured as 10 meV, which is some way distant from these values of around 3 meV.

E_2 becomes the average of the acceptor and donor binding energies would be expected to be quite different. Being unable to resolve the individual peaks means that E_2 is the averaged binding energy for all exciton binding impurities in the material. It is impossible to make any definite statement about the values obtained because of the errors on each measurement mean that they are all statistically similar. The large errors on E_2 and C_2 are due to the lack of accuracy in the data points as there is not a large enough range of temperature values.

The variation in C_1 may indicate that there are less dissociation states for excitons in the $CdCl_2$ annealed material, which is consistent with a lower number of centres responsible for large perturbations in the material capable of destroying excitons.

6.4.4. Analysis of 1.45 eV Emission

Figure 57 show the 1.45 eV centred emission band from one of the samples composed from the proposed series of peaks. Peak Fit was used to find and then fit a number of peaks under the curve. A second order derivative search method was used to find the centre of the peaks. Gaussian line shapes were used (see section 2.6.3) as emission sites are likely to be affected by local lattice imperfections. Table 6.4 gives the results of the fit.

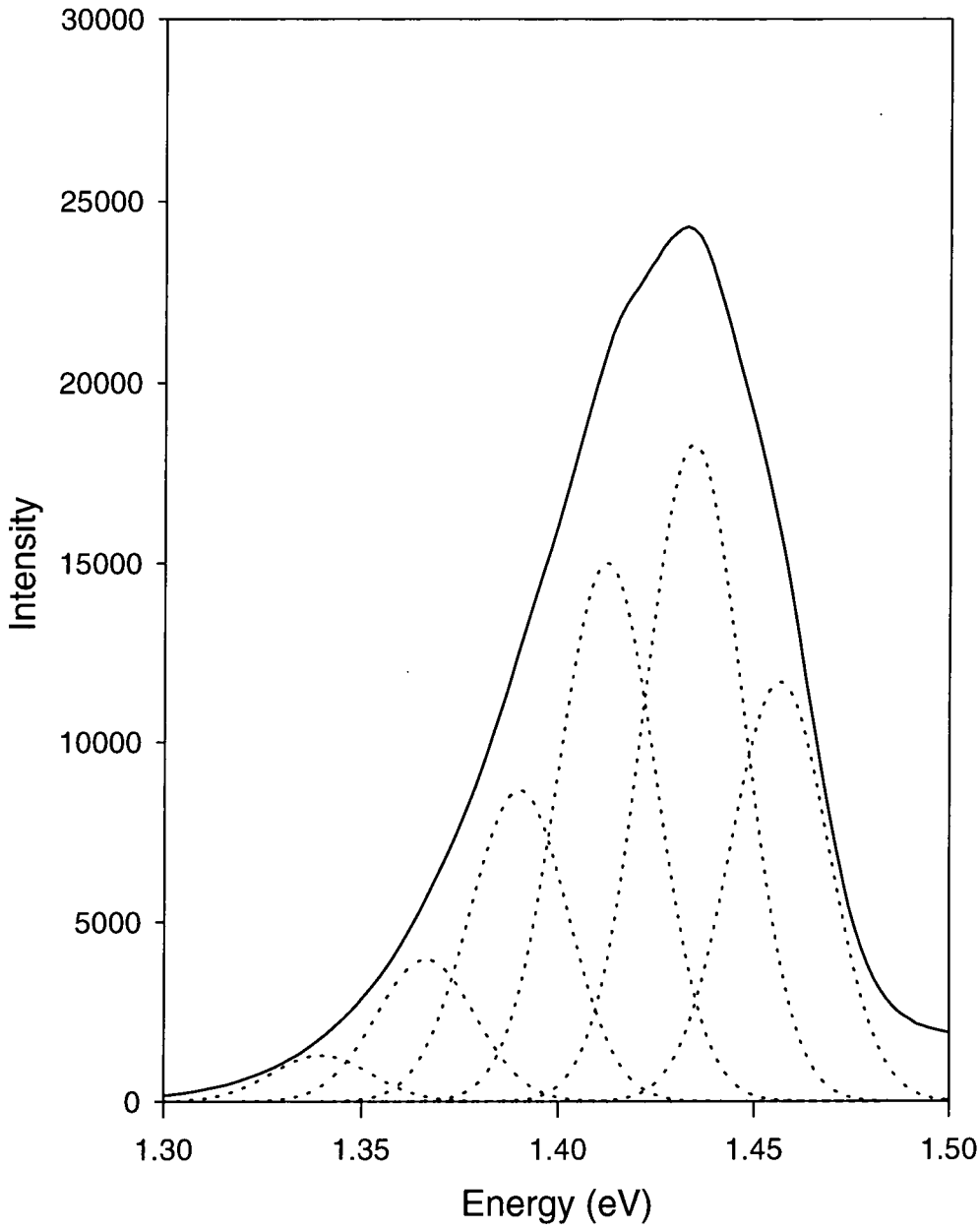

Figure 57: Fit to deep level emission

The fit was restricted so that it had to give each peak the same width at half maximum. The values of the intensity and central energies are given in Table 6.4:

Peak	Intensity	Centre (eV)	difference
1	1274	1.3397	
2	3955	1.3663	0.0266
3	8666	1.3899	0.0236
4	15000	1.4122	0.0223
5	18300	1.4344	0.0222
6	11680	1.4563	0.0219
7	1632	1.4881	0.0318

Table 6.4: Peak fit parameters for deep level emission

It seems clear that the deep level can indeed be modelled using a centre having a strong coupling to the lattice. The LO phonon energy in CdTe has been measured to be 21 meV[143] and the separation between points is within experiment error.

It is also possible to calculate the Huang-Rees lattice coupling parameter for the level. Calculations give S=1.6 if the emission at 1.45 eV is assumed to be the no-phonon line. This indicative of an emission site heavily coupled to the lattice, as might be expected for V_{Cd}-Cl_{Te}.

6.5. Conclusions

Photoluminescence of cadmium telluride reveals there are three clearly separate emissions, one around the band edge at 1.59 eV, one around 1.55 eV and one around 1.45 eV.

The 1.59 eV peak is found to be of excitonic nature. The excitonic peaks in all the samples were significantly broader (≈25 meV) than in single crystal material (≈1 meV). This makes a direct reading of the impurity species responsible for the

peaks through the energy of emission impossible. Even so, there is a definite shift in the excitonic peak of the $CdCl_2$ treated sample, indicating the material has become more p-type.

The 1.55 eV emission is believed to be a donor acceptor pair, by comparison with other authors.

The 1.45 eV is found to be the free to bound transition of an electron recombining at hole trap centre, $V_{Cd}X_{Te}$, 0.14 eV above the valence band edge. This level is highly coupled to the lattice.

7. DEPTH DEPENDENCE OF CdS/CdTe SOLAR CELL PHOTOLUMINESCENCE

7.1. Summary

A study has been undertaken of the depth variation in the photoluminescence emission spectra from the CdTe layer of differently treated CdS/CdTe based solar cell devices. The surface of the cells were bevel etched and the profiles of the depth of cadmium telluride versus position measured. By recording the photoluminescence spectra from different areas of the cells, corresponding to different depths of CdTe material, the trends in the three main photoluminescence peaks were used to aid identification of their microscopic origin and their potential relationship to the improvement in the cell efficiency.

7.2. Introduction

Although photoluminescence is a very useful non-destructive technique in the characterisation and analysis of materials, it has the disadvantage that in the case of a highly absorbing material, such as a direct gap semiconductor like cadmium telluride, only the region close to the surface is probed. The resulting spectra may not be representative of the whole sample. If the material has been surface treated, by polishing or etching for instance, the surface may contain additional defects or impurities resulting in different energy states not present in the bulk.

In the case considered here, the treatment of interest is the coating with $CdCl_2$ and annealing in air. The photoluminescence spectra obtained in the previous chapter will have measured the effect of that treatment at the back surface of the cell,

whereas it has been suggested that the treatment also alters the CdS/CdTe interface region resulting in the observed changes in the cell efficiency[144,145].

The samples used to investigate the changes in photoluminescence with increasing thickness of CdTe had been prepared for EBIC measurements by evaporating gold pads on to the etched devices which made the layout of some samples difficult to use for these photoluminescence measurements.

The measurements provide insight into the changes in the impurity distribution throughout the cadmium telluride layer and suggest and support explanations of the origin of the emissions and the improvement in cell performance.

7.3. Experimental Details

Samples were grown as described in Chapter 6. An extra sample was obtained which had been prepared without any CdS layer, by depositing CdTe onto ITO coated glass using Close Space Sublimation at 500 °C. It then had 60 nm of $CdCl_2$ evaporated on to it and was annealed in air for 25 minutes at 400 °C.

The samples were prepared for the depth dependent measurements by bevel etching them using a mixture of bromine (Br_2), methanol (CH_3OH) and ethyleneglycol ($C_2H_4(OH)_2$) to give cells as shown in Figure 58.

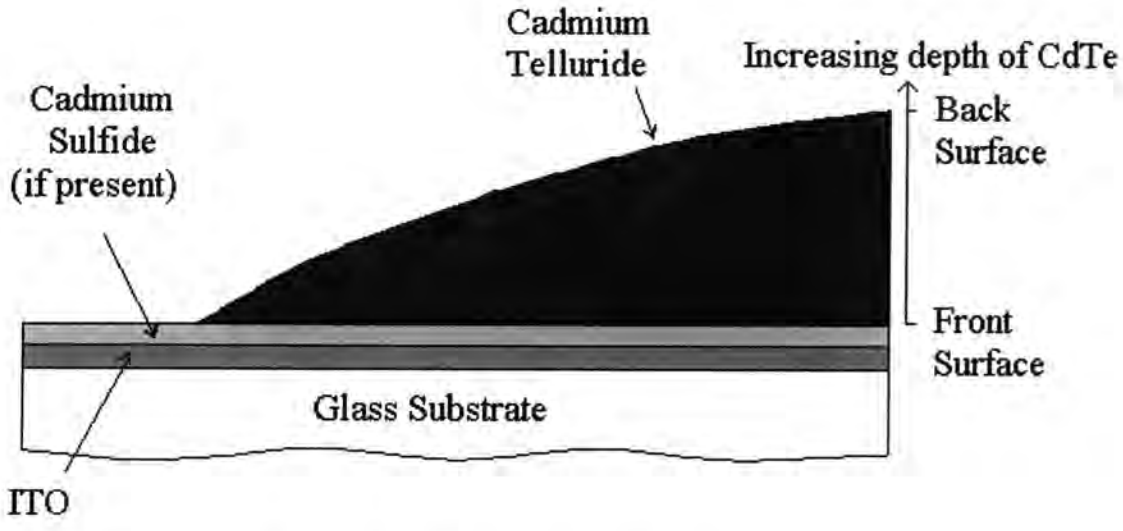

Figure 58: Bevelled solar cell sample

To study the depth dependence it was necessary to move the laser spot over the bevelled samples to allow regions with different depths of CdTe from the junction to be investigated. The sample was moved under a stationary laser spot, rather than altering the laser spot position and hence all of the optics. The facility to allow this was provided by an *xyz* stage on which the entire cryostat was mounted. Once the sample had been mounted in the cryostat, the temperature was reduced to 10 K and the signal optimised. A similar optical layout to that described in the previous chapter was used. The Neutral Density Filter wheel was replaced with a pin hole, created by drilling a sheet of metal foil with a 0.35 mm bit. Examination under a travelling microscope revealed that the hole was in fact slightly elliptical, with a major axis of 0.40 mm and a minor axis of 0.35 mm. A laser power density of 50 $mWcm^{-2}$ was used for the measurements.

As the samples were small (typically 1 cm square) the reductions in the laser spot size dramatically reduced the uncertainty in the measurement of the depth which was being studied. The pin hole was preferred to using a lens to focus the light, which would have introduced an uncertainty in the laser power density and also increased

the excitation density of the laser spot to a level which would have given a significant photoexcited carrier concentration, capable of shifting the energy of some of the observed photoluminescence features through coulomb screening. This also helped to increase the resolution of the depth measurements as a smaller area of the sample was being examined. This meant a more accurate estimate of the depth of cadmium telluride at the laser spot position was possible.

It was also necessary to use a reduced laser spot size as the area of bevelled material available for use in these measurements had been reduced by the gold dot deposited for EBIC measurements. This ensured that no extraneous photoluminescence from the regions of the etch resistant area, or from around the gold dot, was recorded.

To enable the calculation of the depth of the CdTe above the CdS/CdTe interface, a note was made of exactly how far up or down the sample the laser spot was for each spectra recorded. The depth profile of the bevelled samples was measured using a Tencor Instruments Alpha Step 5000. This machine runs a needle point along the surface of the device, recording the surface height. By telling the machine which part of the sample is flat, it calculates the height of the surface relative to that flat line. The samples here had flat regions where all the CdTe had been etched away revealing CdS, or in the case of the no CdS layer sample, ITO. Some had regions down the side which had been coated in etch resistant material which could be used. Once the profiles had been analysed a print out was produced by the machine, an example of which is shown in Figure 59. The thickness of cadmium telluride present at a particular distance up the sample could then be obtained from the print out.

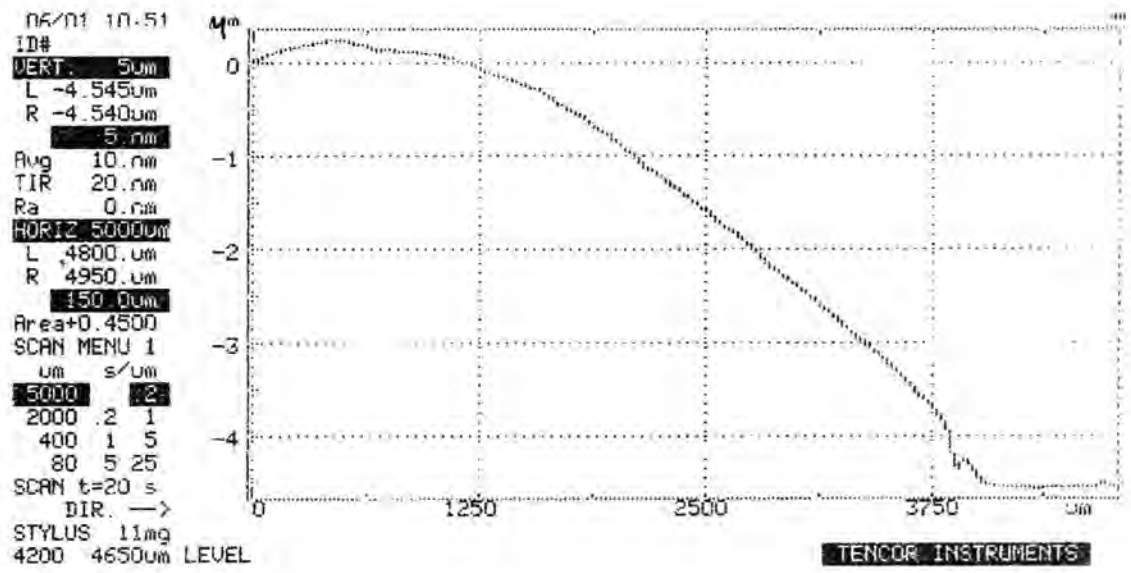

Figure 59: Alpha step scan for $CdCl_2$ sample

7.4. Results

The spectra obtained from various positions on the $CdCl_2$ treated sample are given in Figure 60. It can be clearly seen that the emission spectra changed dramatically as different regions of the sample were examined. The most significant change is in the 1.55 eV band.

Three main luminescence bands were observed. An excitonic band around 1.59 eV, a band around 1.55 eV and a deep level band around 1.45 eV. See the previous chapter for a discussion of the origin of these emissions.

In comparing the spectra from the back surface of $CdCl_2$ treated sample in Figure 51 and the spectra recorded from a depth of 4.90μm in Figure 60 it can be seen that the relative intensity of the three main peaks have altered. The large decrease in the 1.6 eV peak is caused by a variation in the laser power density used for recording the spectra, which will affect the 1.60 eV peak more than the two lower energy peaks as

a result of the superlinear power dependence. In addition, the sample used in Figure 60 will have been etched in the preparation of the bevel. This treatment will alter the states near the luminescent surface probed by the measurement. Sobiesierski et al have demonstrated the changes in photoluminescence caused by varying the surface treatment of CdTe samples[146].

The intensity of each of these peaks versus depth data for the differently treated samples are shown in Figure 61, Figure 62, Figure 63 and Figure 64. The samples generally show increasing levels of luminescence as you move away from the junction between the CdS (or ITO) and CdTe and then decreasing again towards the back surface of the cell. As discussed in the previous chapter, microscopy studies have shown that the grain size increases with the distance from the interface, and it is the grain boundaries which are a major cause of non-radiative recombination[147]. In all the cases shown here though, the spectra recorded at depths of CdTe close to the back surface of the cell give reduced levels of emission. This is probably due to the effect of surface states introduced during the growth and annealing processes.

As the thickness of cadmium telluride approaches zero it is to be expected that the luminescence intensity should fall because the zero reference was made at the point where the laser spot was equally placed on the cadmium telluride layer and the cadmium sulfide (or ITO) layer. Hence any measurement near the zero will have a proportion of the laser power not incident on the CdTe. An absorption coefficient of greater than 5×10^4 cm^{-1}[148] for 457.9 nm light implies that 90% of the light will be absorbed in less than 0.5μm of cadmium telluride so only the zero measurement will suffer from any problems of the excitation light passing through the material and being lost.

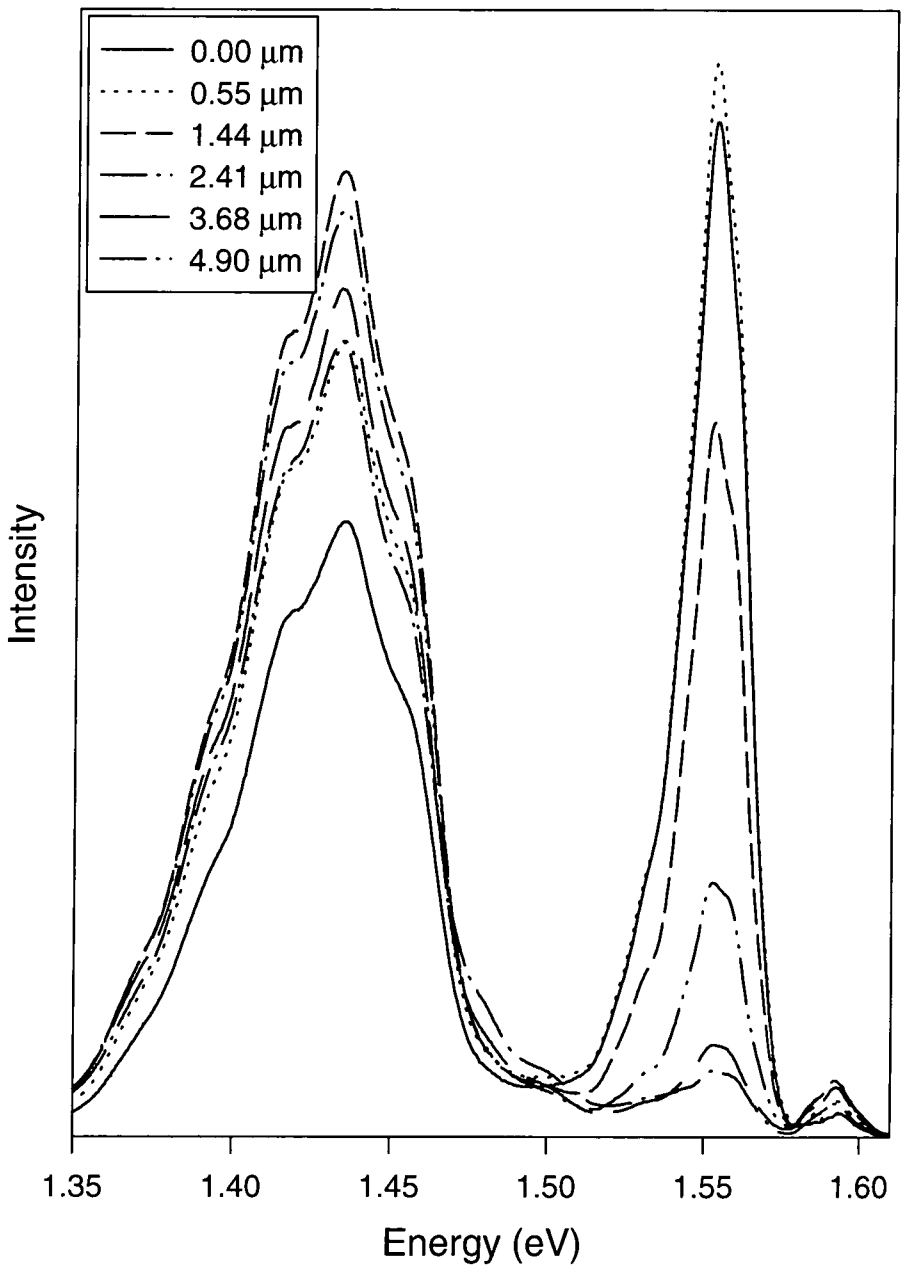

Figure 60: Photoluminescence spectra from different depths of the CdTe layer of a $CdCl_2$ treated CdS/CdTe solar cell

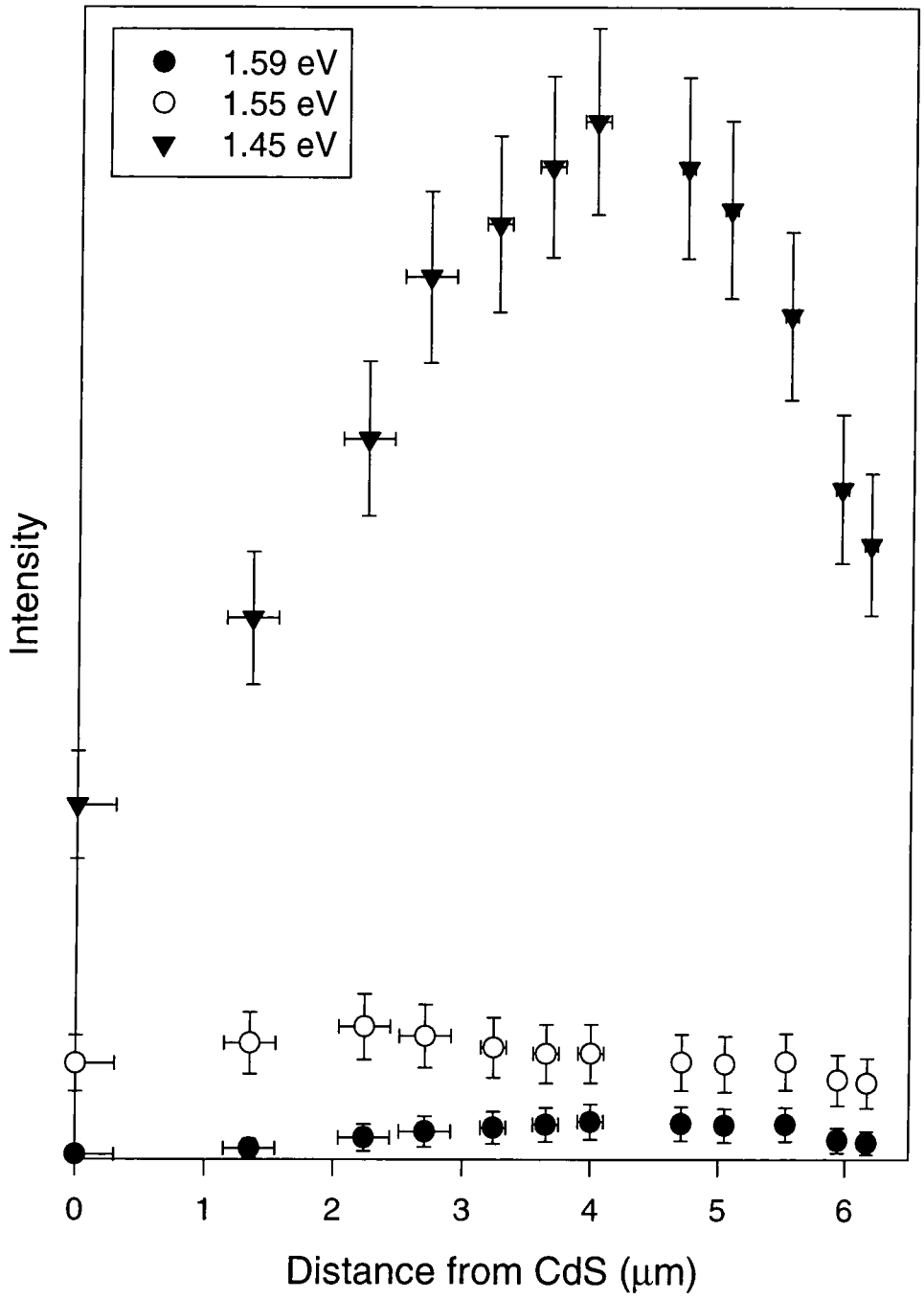

Figure 61: Depth dependence of photoluminescence intensity for as grown sample

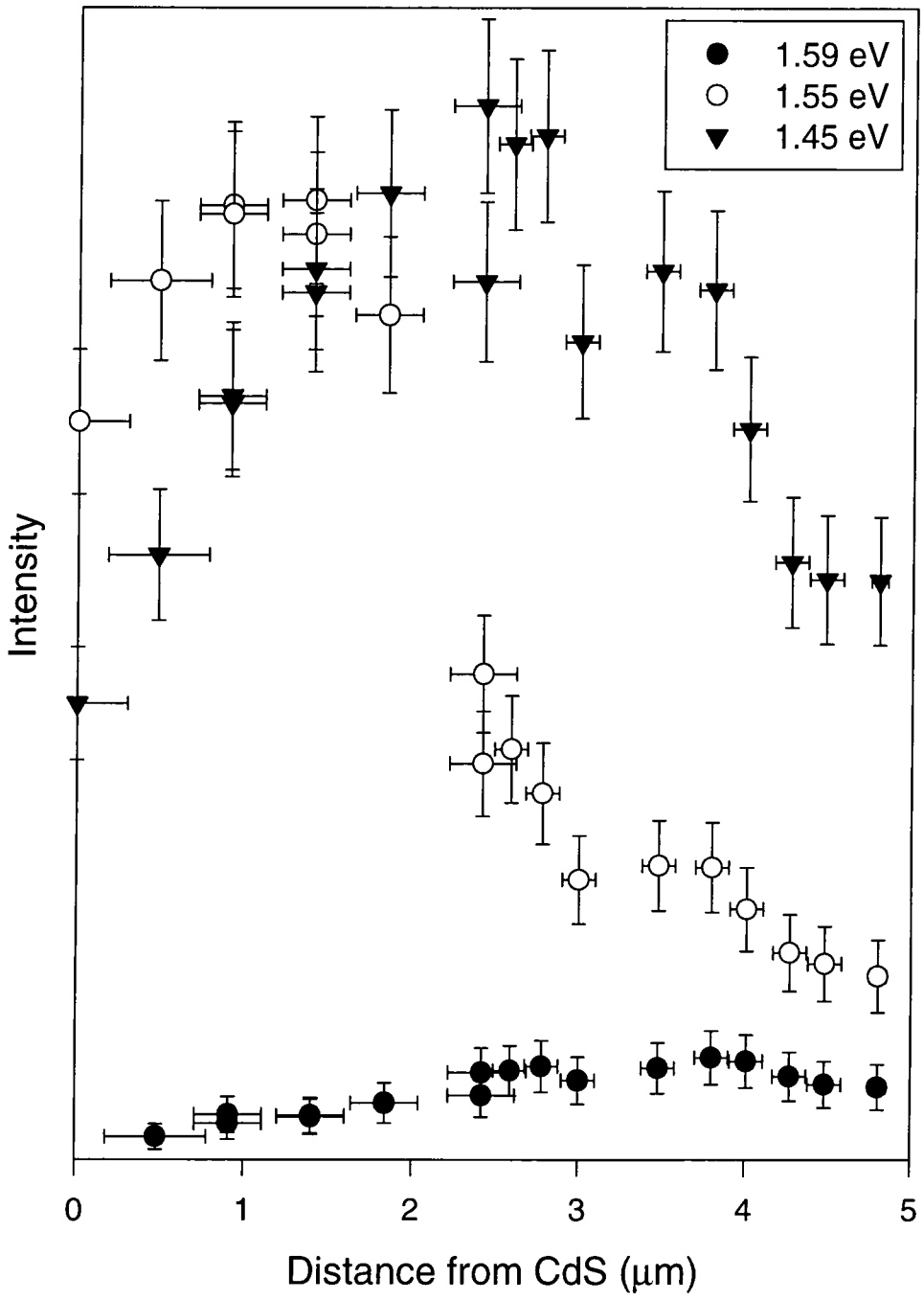

Figure 62: Depth dependence of photoluminescence intensity for air annealed sample

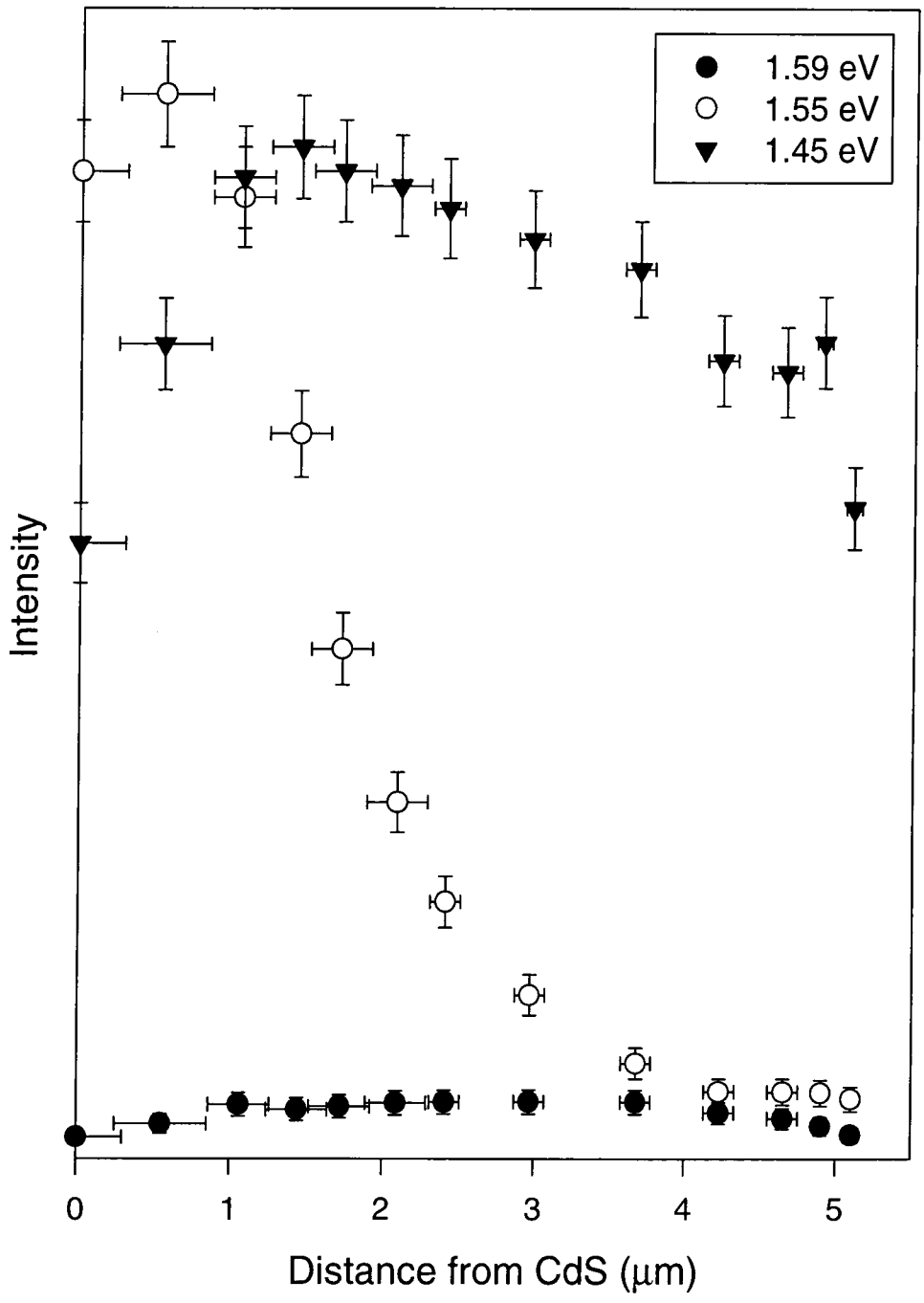

Figure 63: Depth dependence of photoluminescence intensity for $CdCl_2$ annealed sample

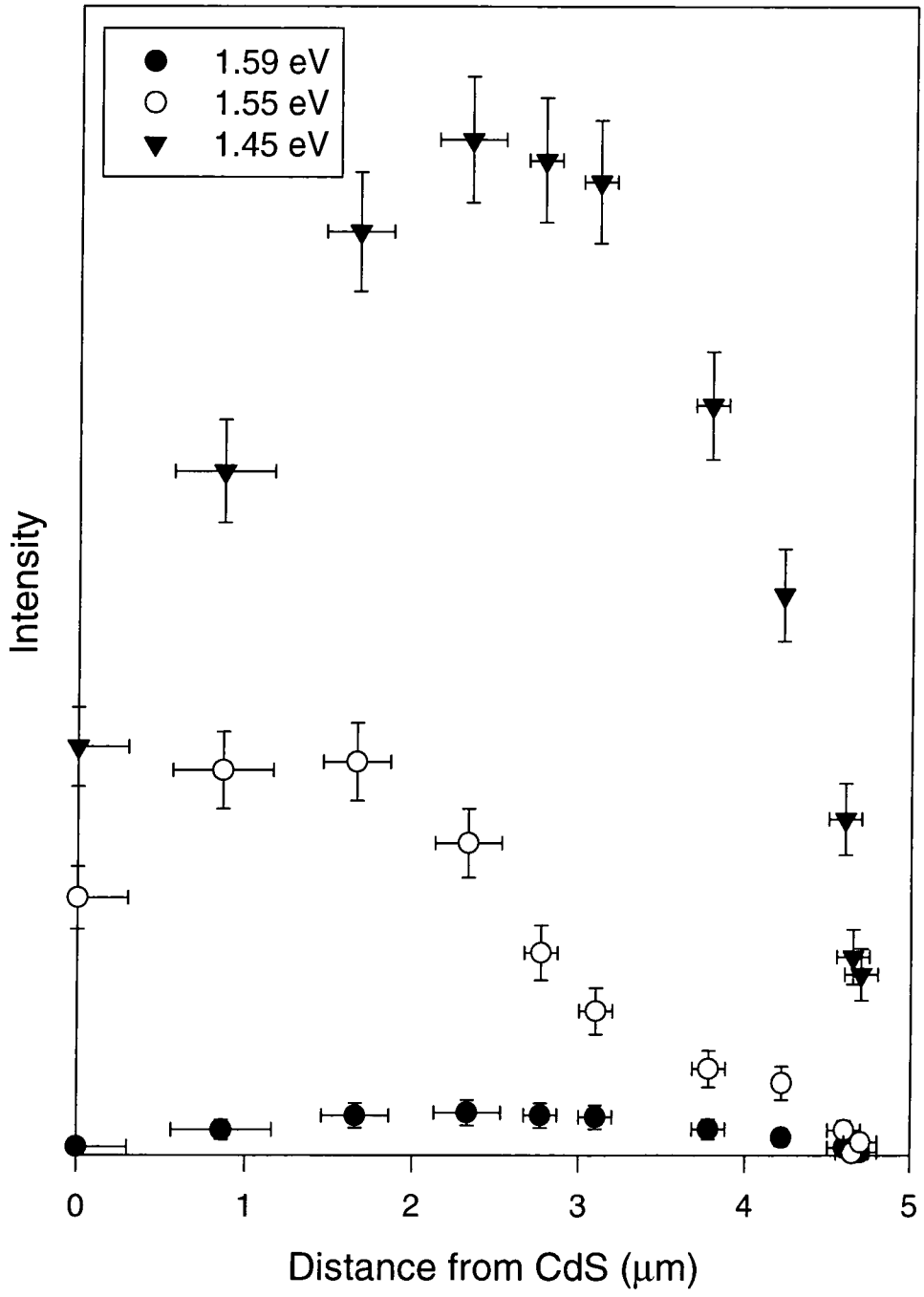

Figure 64: Depth dependence of photoluminescence intensity for sample with no CdS layer

Experiments done with all the samples mounted on the same cold finger showed no discernible difference in the intensity, measured at the same depth, between the

differently treated samples. The spectra were measured under exactly the same conditions.

7.5. Discussion

7.5.1. 1.59 eV Band

As can be seen from the data in the previous section, this band is weak in comparison with the other two emission bands, which indicates a low exciton lifetime caused by the high level of defects and impurities associated with any polycrystalline material. Figure 65 shows a comparison of the depth dependence profile for the intensity of the 1.59 eV peak in each of the four samples.

All of the samples show decreased excitonic emission near the front and back surfaces of the cadmium telluride which is to be expected since structural defects in the lattice in these regions near the surface will be capable of dissociating excitons.

The as grown and air annealed samples have similar distributions. This suggests that the air anneal does not significantly affect the distribution of shallow impurities.

The $CdCl_2$ treatment does alter the emission profile, making it more uniform. The $CdCl_2$ is known to act as a wetting agent or flux, which may help to redistribute the shallow impurities within the CdTe giving this result.

The sample which was grown without any CdS layer, but then treated with the $CdCl_2$ anneal shows a much larger variation through the thickness of CdTe. Hence, the cadmium sulfide layer must be present for a uniform distribution to be obtained. Two possibilities exist for this result; either the lack of a CdS layer allows an increased level of diffusion of an impurity from the ITO which creates states in the

CdTe, or the inclusion of sulfur into the CdTe increases the exciton lifetime at the interface by changing the non-radiative pathways, possibly though a reduction of deep level states. The physical basis for this second process is unknown.

Both the samples that have been annealed in air after treatment with $CdCl_2$ show a shift in the maximum of the intensity profile towards the front of the cell. It is know that this treatment does increase grain size[149], and this re-growth may lower the concentration of structural defects near the surface. The region of the sample to be most affected by this will be those regions close to the CdS/CdTe interface where the crystal structure is heavily dislocated. Hence the exciton lifetime in these regions will increase after the re-growth treatment and emission intensity will increase. This may be due to the $CdCl_2$ acting as a fluxing agent, working from the back of the cell and promoting grain growth, or through passivation of the grain boundaries near the junction[150].

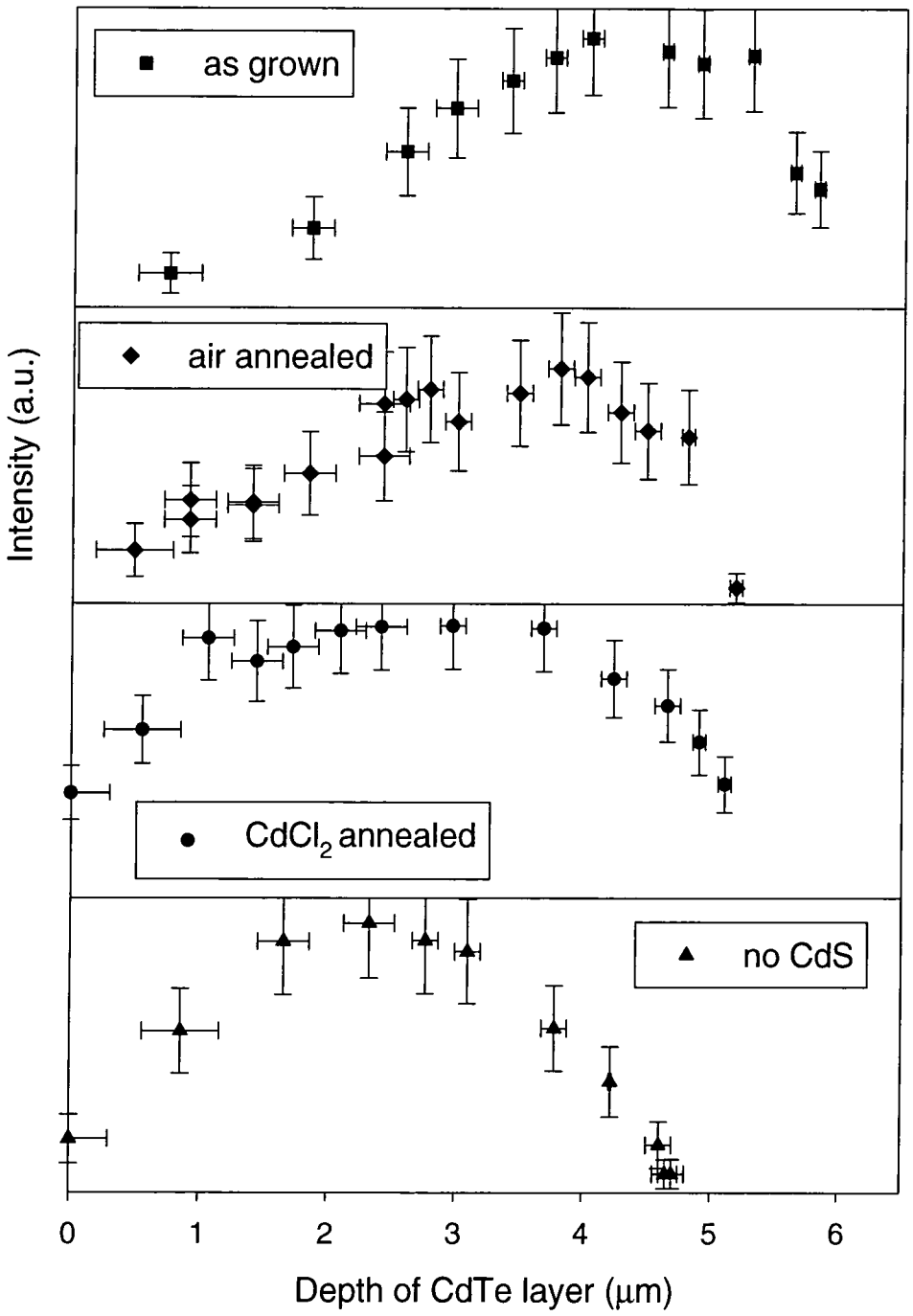

Figure 65: Comparison of 1.59 eV photoluminescence emission band

7.5.2. 1.55 eV Band

The depth dependent intensity profile for the 1.55 eV photoluminescence emission peak is shown in Figure 66 for all samples. This is the emission band which is the most dramatically affected by the treatments. It would seem likely that the process which alters the efficiency of the cells is connected to the origin of this emission.

The as grown profile is approximately flat, with a slight peak in the middle of the CdTe layer. Heating the samples in air causes an increase in the level of this emission, mainly near the interface.

The $CdCl_2$ treatment and anneal in air causes a similar effect to the simple anneal in air, with the peak level of the emission occurring even nearer to the CdS interface than for the anneal without $CdCl_2$.

The lack of presence of sulfur during the $CdCl_2$ treatment again alters the depth profile of the emission, with the peak level occurring slightly further away from the interface.

Although dramatic changes occur in the emission near the interface region of the samples, there is little or no change towards the back surface of the samples.

Two likely candidates exist for the origin of this emission band. Either oxygen could be preferentially diffusing down the grain boundaries, where it forms an acceptor, O_{Te}, as measured by Akimoto[151,152] giving rise to emission through DAP transitions, or $V_{Cd}(Cl_{Te})_2$ sites are created by the anneal, a species which has been associated with an electron trap (donor) some 0.05 eV below the conduction band edge[153].

However, given the level of emission is also seen to increase in samples annealed in air without any prior treatment with $CdCl_2$ it would seem that the O_{Te} site is a more likely candidate. It is possible that the $CdCl_2$ acts as a fluxing agent aiding the flow

of O_{Te} sites to the interface. It is known that cells which undergo the $CdCl_2$ anneal in atmospheres containing no oxygen do not have their efficiencies affected in the same way[154]. It would be of interest to perform these emission profiling experiments on such a cell, as this would enable a resolution to the question of whether oxygen is responsible for this photoluminescence emission band.

If oxygen is responsible, it should be expected that the level of emission should increase in intensity from the front surface to the back, whereas the intensity near the back surface does not show any such increase. It may be that the oxygen is preferentially attracted to locations in the lattice nearer the junction, possibly due to the increased levels of dislocations there.

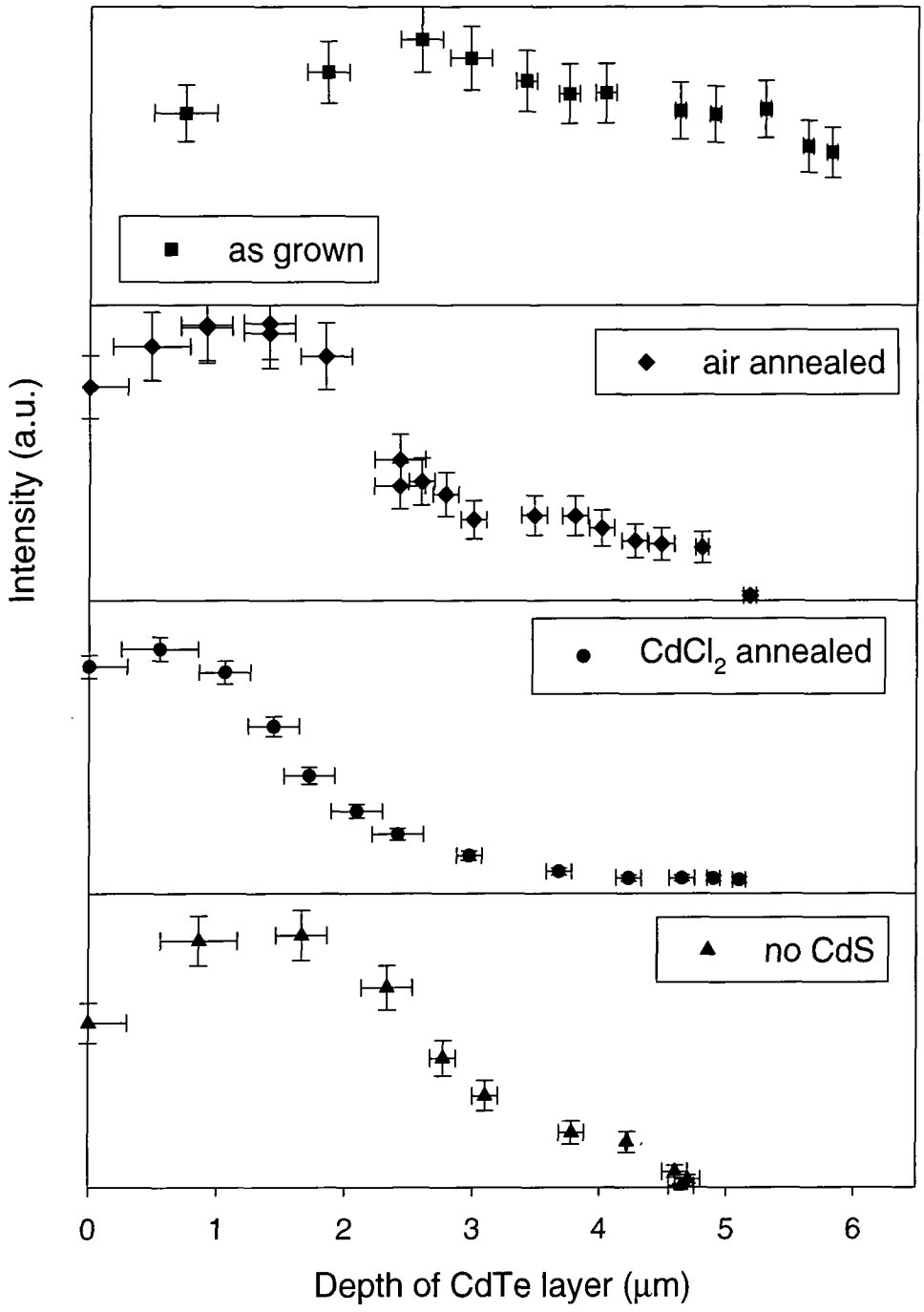

Figure 66: Comparison of 1.55 eV photoluminescence emission band

7.5.3. 1.45 eV Band

Figure 67 shows the profiles of the 1.45 eV photoluminescence emission band for the four differently treated samples. If this emission is a transition between a free electron and a $V_{Cd}Cl_{Te}$ complex as has been assigned in the previous chapter, the fact that this peak exists at all in the as grown material, where no specific doping with chlorine has taken place (the source of the dopant being a residual background level) suggests that this impurity has a strong effect on properties of the CdTe at a relatively low concentration level. The decrease in intensity closer to the CdS interface suggests an increased level of grain boundaries providing non-radiative pathways, as one would expect the concentration of these centres to be relatively constant throughout the layer if the incorporation is through this residual background source.

The air annealed sample shows that the peak intensity has moved toward the interface region. As is discussed later, this may increase the chance of a photogenerated electron leaving the cell thus increasing the cell efficiency.

The $CdCl_2$ treated cell shows a very large shift in the peak level of the emission, which now occurs within the first two microns of the CdS interface. It is also clear that the magnitude of the 1.45 eV emission does not change with the anneal in $CdCl_2$ compared to the other samples. For each molecule of $CdCl_2$ incorporated into the lattice a cadmium vacancy and two chlorine donors would be created, so increasing the number of $V_{Cd}Cl_{Te}$ complexes. However at the temperatures used in the growth and post-growth treatment of these cells, it has been shown by Bell et al[155] by using chemical bond energies that the majority of the chlorine atoms will form $V_{Cd}(Cl_{Te})_2$ complexes, increasing the intensity of the 1.55 eV peak. If the concentration of chlorine atoms is very low then the probability of two chlorine atoms meeting is very

small and so in the residual background doped cases (air annealed and as grown samples) the majority of chlorine atoms will be in the form of $V_{Cd}Cl_{Te}$.

The sample having no CdS layer is similar in profile to the air annealed sample and it is clear that the sulfur does play an important role in the creation of the impurity responsible for this emission, although the process is unknown. Diffusion of the sulfur from the CdS aided by the $CdCl_2$ fluxing agent may be responsible for this. Sulfur, oxygen and chlorine will occupy tellurium sites in the crystal lattice, which will aid cadmium vacancy formation. This can support the interpretation that the emission centre responsible is a $V_{Cd}Cl_{Te}$ complex if one assumes that the tellurium does not become an interstitial impurity or does not diffuse into the CdS layer.

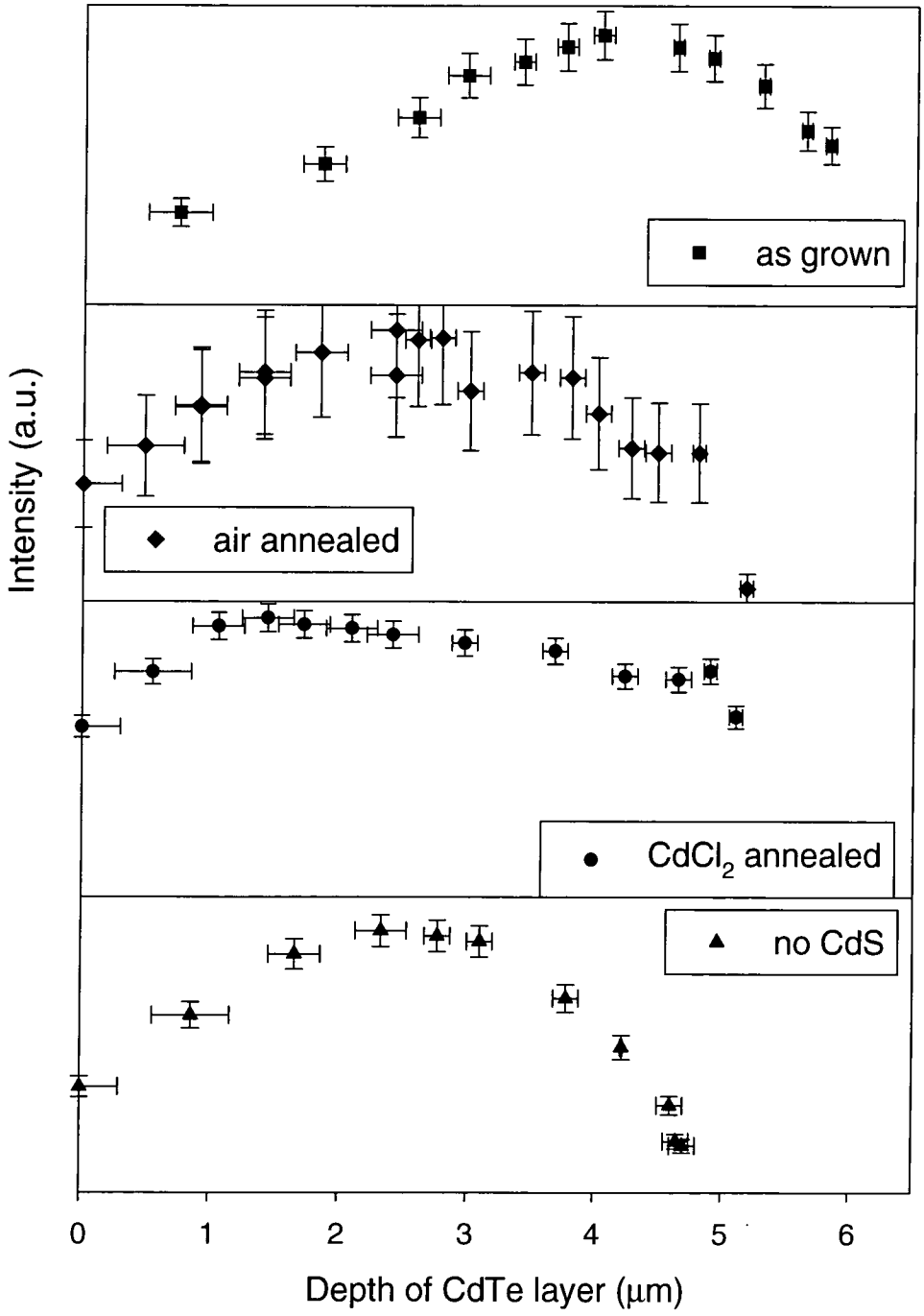

Figure 67: Comparison of 1.45 eV photoluminescence emission band

As to the variation in photovoltaic efficiency of these structures, the deep level hole trap centre, $V_{Cd}Cl_{Te}$ will be a recombination centre of electrons which would otherwise leave the cadmium telluride and perform work in an external circuit. It is

also a relatively deep state and will have a dramatic effect on the electrical properties. Those samples with increased levels of $V_{Cd}Cl_{Te}$ will therefore have lower efficiencies. Samples having a high concentration of this centre will have a Fermi energy closer to the centre of the band gap in those regions, and electrons entering will experience a potential well in which they may reside for a larger portion of time, increasing the chance of recombination. The $CdCl_2$ treated sample, and to a lesser extent the air annealed sample, will have a lower number of these sites all the way from the junction to back surface, so it will not possess any such potential well to lower the cell performance.

It can also be seen that presence of sulfur seems to generally affect the emission near the junction suggesting diffusion out of the CdS layer does occur. Sulfur is a group VI element like tellurium, and will tend to substitutionally replace tellurium atoms. It has been found by Fischer et al[156] that the treatment creates alloys of CdS_xTe_{1-x}, with x=0.1 for tellurium rich regions and $x \approx 1$ for sulfur rich regions. The tellurium rich region will have an energy gap of slightly lower than that of CdTe[157] and hence make it closer to the ideal value of 1.28 eV[158]. The effect would be small but the cell efficiency would increase. The tellurium can of course diffuse into the cadmium sulfide. This will narrow the window layers band gap which will increase the absorption of light in the CdS layer, lowering the cell efficiency.

The potential for further work with this type of measurement on CdS/CdTe solar cells is large. As mentioned above, a combination of samples grown in and then treated in atmospheres both free of and containing oxygen would hopefully yield an answer to the question over the role of oxygen in the process of improving the cell efficiency. Also, it would be preferable to have larger samples bevelled with smaller slopes for the purpose of more accurate measurement of regions close to the

interface. With the increase in the intensity of the 1.55 eV photoluminescence emission band, it would be possible to perform the laser power experiments in chapter 6. This could reveal whether the band resulted from a free to bound transition or from a donor acceptor pair emission.

It would also be useful to use a different cadmium halide flux for the anneal. The incorporation of fluorine, bromine or iodine into the lattice instead of chlorine might give information on the deep level state. The use of different annealing times could reveal how quickly some of changes occur within the cells. This could be of use for optimising the treatment's conditions.

7.6. Conclusions

Many authors have suggested that understanding the interface region is crucial to understanding the origin of the improvement in solar cell efficiency, and using a novel etching technique it has been possible to investigate the depth dependence of photoluminescence emission from the whole thickness of the cadmium telluride layer of CdS/CdTe solar cells. It was found that the major changes do occur at the interface and that the 1.55 eV emission band was the most affected by coating the CdTe with $CdCl_2$ and annealing in air. This band may be associated with O_{Te} sites which causes passivation of the grain boundaries thus reducing the recombination of photogenerated carriers.

Another possibility arises for the improvement in cell efficiency. The treatment creates a concentration gradient for $V_{Cd}Cl_{Te}$ complexes which will not create a potential well capable of trapping electrons and increasing recombination.

It is also clear from our data that the diffusion of sulfur affects the distribution of the states responsible for the observed photoluminescence emissions. It would seem likely that the diffusion of sulfur is involved in the improvement in cell efficiency, although no further conclusion is possible from this work.

Several workers have attempted to use photoluminescence of the back surface of the cadmium telluride layer to gain insight into the source of the efficiency improvement. However, it has not been possible to obtain a satisfactory explanation as to the nature of the increase and it is clear from the data presented in this chapter that the reason for this is that the major changes in cell behaviour occur at the interface between the CdS and CdTe and this region is not probed by measurements of the back surface, such as those in Chapter 6. Since little influence is asserted on these "back-wall" spectra by the interface region, it is questionable whether the standard photoluminescence techniques will be of any significant value when applied to the cell back surface as the improvement in cell efficiency is most likely due to changes at the interface.

8. ACKNOWLEDGEMENTS

I wish to gratefully thank all of the following people:

Dr Douglas Halliday, my supervisor, whose happy soul has been an impenetrable fortress against the forces of disillusionment which are associated with the trials of Ph.D. life. It is mainly through his patient help, both practical and theoretical, that this thesis has been made possible.

Everybody associated with the Physics Department in the University of Durham. So many people have lent me equipment, time or expertise over the three years in the Department they are truly are too numerous to mention.

EPSRC for the grant funding of my Ph.D.

Several others have contributed their skill, time and resources to specific topics contained within this thesis. They are:

Chapter 4: K. Y. Lee of the IBM T. J. Watson Research Centre, P. O. Box 218, Yorktown Heights, NY 10598, U.S.A for the growth of the GaAs membranes.

Chapter 5: P. N. Adams for the production of the polyaniline, S. E. Cox and I. A. Pentland for the production of the porous silicon and porous silicon/polyaniline devices and E. R. Holland for the electrical measurements and Dr. Andrew Beeby for

the photoexcitation spectra. I would like to recognise financial support from The Nuffield Foundation and the EPSRC for some of the work in this project.

Chapter 6: I would like to thank Ken Durose of the University of Durham for providing the samples, which were grown by of D. Bonnet and H. Richter, of ANTEC GmbH, Industriestrasse 2-4, 65779 Kelkheim / Ts, Germany.

Chapter 7: A. Crozier for her project work on the bevel etching of the devices.

Personal thanks go to all of my friends from the department, college, at home around Penrith and at Seaham Harbour. I would especially like to thank Christopher Leighton, with whom I shared a house, department and cricket team for the majority of my Ph.D.

9. REFERENCES

[1] Canham, L. T. (1990). "Silicon quantum wire array fabrication by electrochemical and chemical dissolution of wafers." Appl. Phys. Lett. **57**(10): 1046-1048.

[2] Britt, J. and C. Ferekides (1993). "Thin-Film Cds/Cdte Solar-Cell With 15.8-Percent Efficiency." Applied Physics Letters **62**(22): 2851-2852.

[3] Kittel, C. (1986). Introduction to Solid State Physics. New York, John Wiley & Sons, Inc., 6th Ed., page 43.

[4] Kronig, R. L. and W. G. Penney (1931). Proc. R. Soc. London **A130**: 499.

[5] Singh, S. (1983). "Kronig - Penney in Reciprocal Space." Am. J. Phys. **51**(2): 179.

[6] Abramowitz, M. and I. A. Stegun (1972). Handbook of Mathematical Functions. New York, Dover. Page 75

[7] Chelikowsky, J. R. and M. L. Cohen (1976). "Nonlocal pseudopotential calculations for the electronic structure of eleven diamond and zinc-blende semiconductors." Phys. Rev. B **14**(2): 556-582.

[8] Chelikowsky, J. R. and M. L. Cohen (1976). "Nonlocal pseudopotential calculations for the electronic structure of eleven diamond and zinc-blende semiconductors." Phys. Rev. B **14**(2): 556-582.

[9] Chelikowsky, J. R. and M. L. Cohen (1976). "Nonlocal pseudopotential calculations for the electronic structure of eleven diamond and zinc-blende semiconductors." Phys. Rev. B **14**(2): 556-582.

[10] Kittel, C. (1986). Introduction to Solid State Physics. New York, John Wiley & Sons, Inc., 6th Ed., pages 176-178

[11] Tanner, B. K. (1995). Introduction to the Physics of Electrons in Solids. Cambridge, Cambridge University Press. 1st Ed., pages 112-113.

[12] Kittel, C. (1986). Introduction to Solid State Physics. New York, John Wiley & Sons, Inc., 6th Ed. , page 185

[13] Kittel, C. (1986). Introduction to Solid State Physics. New York, John Wiley & Sons, Inc., 6th Ed., pages 193-194

[14] Tanner, B. K. (1995). Introduction to the Physics of Electrons in Solids. Cambridge, Cambridge University Press, 1st Ed., pages 116-118.

[15] Landolt-Bornstein (1982) "Numerical data and functional relationships in science and technology" Group 3- Crystal and Solid State Physics, **17a** Semiconductors

"Physics of group IV elements and III-V compounds", ed. O. Madelung, Springer-Verlag, Berlin Heildelberg.

[16] Haynes, J. R. (1960). "Experimental proof of the existence of a new electronic complex in silicon." Physical Review Letters **4**(7): 361-363.

[17] Bransden, B. H. and C. J. Joachain (1989). Introduction to Quantum Mechanics. New York, John Wiley & Sons. 1st Ed., chapter 11.

[18] Kittel, C. (1986). Introduction to Solid State Physics. New York, John Wiley & Sons, Inc., 6th Ed., pages 88-91.

[19] Stoneham, A. M. (1985). Theory of Defects in Solids. Oxford, Clarendon Press, 1st Ed., page 295-297.

[20] Hecht, O. (1987). Optics, Addison-Wesley. 5th Ed., pages 480

[21] Eisberg, R. and Resnick, R. (1985). Quantum Physics of Atoms, Molecules, Solids, Nuclei and Particles. New York, John Wiley & Sons, 2nd Ed., page 13-19.

[22] Lee, K. Y., J. Frost, C. Stanley, W. Patrick, W. S. Mackie, S. P. Beaumont and C. D. W. Wilkinson (1987). "Fabrication of ultrasmall devices on thin active GaAs membranes." J. Vac. Sci. Technol. B **5**(1): 322-325.

[23] Wilkinson, C. D. W. and S. P. Beaumont (1986). Electron Beam Lithography, Springer Verlag.

[24] Seidel, L. (1989). "Fabrication and analysis of GaAs Schottky barrier diodes fabricated on thin membranes for Terahertz applications." Int. J. of Infrared and Millimetre Waves **10**(7): 779-787.

[25] Ho, K. M., C. T. Chan, C. M. Soukopulis, R. Biswas and M. Sigalas (1994). "Photonic band gaps in three-dimensions- new layer-by-layer periodic structures." Solid State Comm. **89**: 413-416.

[26] Lee, K. C., J. Silcox and C. A. Lee (1983). "A new method for the fabrication of sub-micron thick gallium arsenide membranes." Appl. Phys. Lett. **43**(5): 488-489.

[27] Lee, K. Y., J. Frost, C. Stanley, W. Patrick, W. S. Mackie, S. P. Beaumont and C. D. W. Wilkinson (1987). "Fabrication of ultra-small devices on thin active GaAs membranes." J. Vac. Sci. Technol. B **5**(1): 322-325.

[28] Mackie, W. S., S. P. Beaumont, C. D. W. Wilkinson and J. S. Roberts (1983). . Proceedings of the 10th International Conference on Electron and Ion Beam Science and Technology, Electrochemical Society, Pennington, NJ.

[29] Sturge, M. D. (1962). "Optical absorption of Gallium Arsenide between 0.6 and 2.75eV." Phys. Rev. **127**(3): 768-773.

[30] Spicer, W. E., P. W. Chye, C. M. Gorner, I. Lindau and P. Pianetta (1979). "The surface electronic structure of III-V compounds and the mechanism of Fermi level pinning by oxygen passivation and metals." Surface Science **86**: 763-788.

[31] Spicer, W. E., P. W. Chye, C. M. Gorner, I. Lindau and P. Pianetta (1979). "The surface electronic structure of III-V compounds and the mechanism of Fermi level pinning by oxygen passivation and metals." Surface Science **86**: 763-788.

[32] Chandra, A., C. E. C. Wood, D. W. Woodward and L. F. Eastman (1979). "Surface and interface depletion corrections to the free carrier density determinations by Hall measurements." Solid State Electronics **22**: 645-650.

[33] Burstein, E. (1954). "Anomalous optical absorption limit in InSb." Phys. Rev. **93**: 632-633.

[34] Moss, T. S. (1954). "The interpretation of the properties of Indium Antimonide." Proc. Phys. Soc. **B76**: 775-782.

[35] Seeger, K. (1985). Semiconductor Physics, Springer Verlag. 305-313

[36] Pankove, J. I. (1971). Optical Processes in Semiconductors, Dover.

[37] Raymond, A., J. L. Robert and C. Bernard (1979). "The electron effective mass in heavily doped GaAs." J. Phys. C: Solid State Phys. **12**: 2289-2293.

[38] Seeger, K. (1985). Semiconductor Physics, Springer Verlag. 323-328

[39] Keldysh, L. V. (1958). "The Effect of a Strong Electric Field on the Optical Properties of Insulating Crystals." Soviet Physics JETP **34**(7): 788-790.

[40] Sturge, M. D. (1962). "Optical absorption of Gallium Arsenide between 0.6 and 2.75 eV." Phys. Rev. **127**(3): 768-773.

[41] Abram, R. A., G. J. Rees, et al. (1978). "Heavily doped semiconductors and devices." Advances in Physics **27**: 799-882.

[42] Sturge, M. D. (1962). "Optical absorption of Gallium Arsenide between 0.6 and 2.75 eV." Phys. Rev. **127**(3): 768-773.

[43]Seeger, K. (1985). Semiconductor Physics, Springer Verlag. 323-328.

[44] Sturge, M. D. (1962). "Optical absorption of Gallium Arsenide between 0.6 and 2.75 eV." Phys. Rev. **127**(3): 768-773.

[45] Lautenschlager, P., M. Garriga, S. Logothetidis and M. Cardona (1987). "Interband critical points of GaAs and their temperature dependence." Phys. Rev. B **35**(17): 9174-9189.

[46] Vina, L., S. Logothetidis and M. Cardona (1984). "Temperature dependence of the dielectric function of germanium." Phys. Rev. B **30**(4): 1979-1991.

[47] Varshini, Y. P. (1967). "Temperature Dependence of the Energy Gap in Semiconductors." Physica **34**: 149-154.

[48] Vina, L., S. Logothetidis and M. Cardona (1984). "Temperature dependence of the dielectric function of germanium." Phys. Rev. B **30**(4): 1979-1991.

[49] Blakemore, J. S. (1982). "Semiconducting and other major properties of gallium arsenide." J. Appl. Phys. **53**(10): R123-R181.

[50] Aspnes, D. E. (1976). "GaAs lower conduction-band minima: Ordering and properties." Phys. Rev. B **14**(12): 5331-5343.

[51] Lautenschlager, P., M. Garriga, S. Logothetidis and M. Cardona (1987). "Interband critical points of GaAs and their temperature dependence." Phys. Rev. B **35**(17): 9174-9189.

[52] Adachi, S. (1985). "GaAs, AlAs, and $Al_xGa_{1-x}As$: Materials parameters for use in research and device applications." J. Appl. Phys. **58**(3): R1-R29.

[53] Blakemore, J. S. (1982). "Semiconducting and other major properties of gallium arsenide." J. Appl. Phys. **53**(10): R123-R181.

[54] Blakemore, J. S. (1982). "Semiconducting and other major properties of gallium arsenide." J. Appl. Phys. **53**(10): R123-R181.

[55] (1985). Landolt-Bornstein Numerical Data and Functional Relationships in Science and Technology. Berlin, Springer-Verlag.

[56] Ulhir, A. Bell Syst. Tech. J. **35**: 333-347.

[57] Turner, D. R. (1958). J. Electrochem. Soc. **105**: 402.

[58] Pickering, C., M. I. J. Beale, D. J. Robbins, P. J. Pearson and R. Greef (1984). J. Phys. C: Appl. Phys. **17**: 6535-6552.

[59] Canham, L. T. (1990). "Silicon quantum wire array fabrication by electrochemical and chemical dissolution of wafers." Appl. Phys. Lett. **57**(10): 1046-1048.

[60] Chuan, Z. and R. Tsu (1995). Porous Silicon. Singapore, World Scientific.

[61] Cullis, A. G. and L. T. Canham (1991). Nature **353**: 335.

[62] Collins, R. T., P. M. Fauchet and M. A. Tischler (1997). "Porous silicon: from luminescence to LEDs." Physics Today **50**(1): 24-31.

[63] Canham, L. T. (1995). "Bioactive silicon structure fabrication through nanoetching techniques." Advanced Materials **7**: 1033-1037.

[64] Peeters, E., B. Puers, W. Sansen, J. Gybels and P. De Sutter (1991). "A two-wire, digital output multichannel microprobe for recording single-unit neural activity." Sensors and Actuators B **4**: 217-223.

[65] Sato, K., Y. Kawamura, S. Tanaka, K. Uchida and H. Kohida (1990). "Individual and mass operation of biological cells using micromechanical silicon devices." Sensors and Actuators A **21-23**: 948-953.

[66] Faulkner, R. A. (1968). "Toward a theory of isoelectronic impurities in semiconductors." Phys Rev **175**: 991-1009.

[67] Brown, T. G. and D. G. Hall (1986). Appl. Phys. Lett. **49**: 245.

[68] Ennen, H., J. Schneider, G. Pomerenke and A. Axmann (1983). Appl. Phys. Lett. **43**: 943.

[69] Oguz, S. (1983). Appl. Phys. Lett. **43**: 848.

[70] Gnutzman, U. and K. Cluasecker (1974). Appl. Phys. Lett. **3**: 9.

[71] Read, A. J., R. J. Needs, K. J. Nash, L. T. Canham, P. D. J. Calcott and A. Qteish (1992). Phys. Rev. Lett. **69**: 1232.

and

Read, A. J., R. J. Needs, K. J. Nash, L. T. Canham, P. D. J. Calcott and A. Qteish (1993). Phys. Rev. Lett. **70**: 2050(E).

[72] Canham, L. T. (1990). "Silicon quantum wire array fabrication by electrochemical and chemical dissolution of wafers." Appl. Phys. Lett. **57**(10): 1046-1048.

[73] Sanders, G. and Y.-C. Chang (1992). Phys Rev B **45**(16): 9202-9213.

[74] George, T., M. S. Anderson, W. T. Pike, L. T. Lin, R. W. Fathauer, K. H. Jung and D. L. Kwong (1992). 60(2359).

[75] Prokes, S. M., O. J. Glembock, V. M. Bermudez, R. Kaplan, L. E. Friedersdorf and P. C. Searson (1992). Phys. Rev. B **45**: 13788.

[76] Prokes, S. M. (1993). J. Appl. Phys. **73**: 407.

[77] Brandt, M. S., H. D. Fuchs, M. Stutzmann, J. Weber and M. Cardona (1992). Solid State Communications **81**: 207.

[78] Stutzmann, M., J. Weber, M. S. Brandt, H. D. Fuchs, M. Rosenbauer, P. Deak, A. Hopner and A. Breitschwerdt (1992). Adv. Solid State Phys. **32**: 179.

[79] Stutzmann, M., M. S. Brandt, M. Rosenbauer, J. Weber and H. D. Fuchs (1993). Phys. Rev. B **47**: 348.

[80] Nash, K. J., P. D. J. Calcott, L. T. Canham, M. J. Kane and D. Brumhead (1994)."The origin of efficient luminescence in highly porous silicon." Journal of Luminescence **60&61**: 297-301.

[81] Calcott, P. D. J., K. J. Nash, L. T. Canham, M. J. Kane and D. Brumhead (1993). Journal of Luminescence **57**: 257.

[82] Calcott, P. D. J., K. J. Nash, L. T. Canham, M. J. Kane and D. Brumhead (1993). J. Phys: Condensed Matter **5**: L91-L98.

[83] Buda, F., J. Kohanoff and M. Parrinello (1992). "Optical properties of porous silicon: a first principles study." Phys. Rev. Lett. **69**: 1272-1275.

[84] Ito, T. and A. Hiraki (1993). "Aging phenomena of light emitting porous silicon." Journal of Luminescence **57**: 331-339.

[85] Lang, W., P. Steiner and F. Kozlowski (1993). "Porous silicon electroluminescent devices." Journal of Luminescence **57**: 341-349.

[86] Li, K., D. C. Diaz, Y. He, J. C. Campbell and C. Tsai (1994). "Electroluminescence from porous silicon with conducting polymer film contacts." Appl. Phys. Lett. **64**: 2394-2396.

[87] Mateeva, E., V. P. Parkhutik, R. D. Calleja and J. M. Martinez-Duart (1993). "Growth of polyaniline films on porous silicon layers." Journal of Luminescence **57**: 175-180.

[88] Bsiesy, A., Y. F. Nicolau, A. Ermolieff, F. Muller and F. Gaspard (1995). "Electroluminescence from n^+-type porous silicon contacted with layer-by-layer deposited polyaniline." Thin Solid Films **225**: 43-48.

[89] Chuan, Z. and R. Tsu (1995). Porous Silicon. Singapore, World Scientific.

[90] Nash, K. J., P. D. J. Calcott, L. T. Canham, M. J. Kane and D. Brumhead (1994). "The origin of efficient luminescence in highly porous silicon." Journal of Luminescence **60&61**: 297-301.

[91] Holland, E. R. and A. P. Monkman (1995). Synthetic Metals **74**: 75-79.

[92] Sze, S. M. (1981). The Physics of Semiconductor Devices. New York, Wiley.

[93] Bsiesy, A., Y. F. Nicolau, A. Ermolieff, F. Muller and F. Gaspard (1995). "Electroluminescence from n^+-type porous silicon contacted with layer-by-layer deposited polyaniline." Thin Solid Films **225**: 43-48.

[94] Bsiesy, A., Y. F. Nicolau, A. Ermolieff, F. Muller and F. Gaspard (1995). "Electroluminescence from n^+-type porous silicon contacted with layer-by-layer deposited polyaniline." Thin Solid Films **225**: 43-48.

[95] Merrigan, J. A. (1976). Sunlight to electricity: Prospects for Solar Energy Conversion by Photovoltaics. MIT Press: 5-6.

[96] Hulstrom, R., R. Bird and C. Riodan (1985). "Spectral solar irradiance data sets for selected terrestrial conditions." Solar Cells **15**: 365-391.

[97] De Vos, A., J. E. Parrott, P. Baruch and P. T. Landsberg (1994). Bandgap Effects in Thin-Film Heterojunction Solar Cells. 12th European Photovoltaic Solar Energy Conference, Amsterdam, The Netherlands.

[98] Palik, E. D. (1985). . Handbook of optical constants. E. D. Palik, Academic Press: 409-427.

[99] De Vos, A., J. E. Parrott, P. Baruch and P. T. Landsberg (1994). Bandgap Effects in Thin-Film Heterojunction Solar Cells. 12th European Photovoltaic Solar Energy Conference, Amsterdam, The Netherlands.

[100] Vodakov, Y. A., G. A. Lomakina and Y. P. Maslakovets (1960). "A p-n junction photocell made of cadmium telluride." Soviet Physics Solid State (USA) **2**(1): 1-4.

[101] Naumov, G. P. and O. V. Nikolaev (1962). "The efficiency of transformation of direct solar radiation energy into electric energy using a CdTe photocell." Soviet Physics Solid State **3**: 2718.

[102] Chu, T. L., S. S. Chu, C. Ferekides, C. Q. Wu, J. Britt and C. Wang (1991). "13.4-Percent Efficient Thin-Film CdS/CdTe Solar-Cells." Journal Of Applied Physics **70**(12): 7608-7612.

[103] Britt, J., C. Ferekides. "Thin-Film CdS/CdTe Solar-Cell With 15.8-Percent Efficiency." Applied Physics Letters **62**(22): 2851-2852.

[104] Shockley, W. and H. J. Queisser (1961). "Detailed balance limit of efficiency of p-n junction solar cells." Journal of Applied Physics **32**(3): 510-519.

[105] Olsen, J. M. and D. J. Friedman (1996). "High efficiency III-VI solar cells." Compound Semiconductor **Nov/Dec**: 27-29.

[106] Basol, B. M. (1992). "Processing high efficiency CdTe solar cells." Int. J. Solar Energy **12**: 25-35.

[107] Giles-Taylor, N. C., R. N. Bicknell, D. K. Blanks, T. H. Myers and J. F. Schetzina (1984). "Photoluminescence of CdTe: A comparison of bulk and epitaxial matter." J. Vac. Sci. Technol. A **3**(1): 76-82.

[108] Siffert, P., A. Cornet, R. Stuck, R. Triboulet and Y. Marfaing (1975). "Cadmium telluride nuclear radiation detectors." IEEE Trans. Nuc. Sci. **22**: 211-225.

[109] Bell, R. O., F. V. Wald, C. Canali, F. Nava and G. Ottaviani (1974). "Characterisation of the transport poperties of halogen doped CdTe used for gamma ray detectors." IEEE Trans. Nucl. Sci. **NS-21**: 331-341.

[110] Francou, J. M., K. Saminadayar, E. Molva and J. L. Pautraut (1984). "Identification of Shallow Donors in CdTe." ICDS 13: 1213-1219.

[111] Molva, E., J. P. Chamontal and J. L. Pautrat (1982). "Shallow Acceptors in Cadmium Telluride." Phys. Stat. Sol. (b) **109**: 635-644.

[112] Al Allak, H. M., S. A. Galloway, A. W. Brinkmann, K. Durose, H. Richter and D. Bonnett (1995). "The effect of processing conditions on the electrical and structural properties of CdS/CdTe solar cells." Proc. 13th European Photovoltaic Solar Energy Conf. **2**: 2135.

[113] Figueroa, J. M., F. Sanchez-Sinencio, J. G. Mendoza-Alvarez, O. Zelaya, G. Contreras-Puente and A. Diaz-Gongora (1990). "Photoluminescence spectra and carrier mobilities in polycrystalline films of CdTe." Journal Of Crystal Growth **106**(4): 651-656.

[114] Aguilar-Hernandez, J., G. Contreras-Puente, J. M. Figueroa-Estrada and O. Zelaya-Angel (1994). "Photoluminescence studies of semiconducting polycrystalline CdTe films." Japanese Journal Of Applied Physics Part 1- Regular Papers Short Notes & Review Papers **33**(1A): 37-41.

[115] Brinkman, A. W. (1994). CdTe based solar cells. Properties of Narrow Gap Cadmium-Based Compounds. P. Capper. London, IEE. **10:** 591-597.

[116] Figueroa, J. M., F. Sanchez-Sinencio, J. G. Mendoza-Alvarez, O. Zelaya, G. Contreras-Puente and A. Diaz-Gongora (1990). "Photoluminescence spectra and carrier mobilities in polycrystalline films of CdTe." Journal Of Crystal Growth **106**(4): 651-656.

[117] Giles-Taylor, N. C., R. N. Bicknell, D. K. Blanks, T. H. Myers and J. F. Scnetzina (1984). "Photoluminescence of CdTe: A comparison of bulk and epitaxial matter." J. Vac. Sci. Technol. A **3**(1): 76-82.

[118] Myers, T. H., J. F. Schetzina, S. T. Edwards and A. F. Schreiner (1983). "Effect of surface preparation on the 77K photoluminescence of CdTe." J. Appl. Phys. **54**(7): 4232-4234.

[119] Bubulac, L. O., J. Bajaj, W. E. Tennant, P. R. Newman and D. S. Lo (1988). "Spatial origin of various PL lines in CdTe at 77K." Journal of Crystal Growth **86**: 536-543.

[120] Norris, C. B. and K. R. Zanio (1982). "Effects of Cd-vapour and Te-vapour heat treatments on the luminescence of solution-grown CdTe:In." J. Appl. Phys. **53**(9): 6347-6359.

[121] Bell, R. O., F. V. Wald, C. Canali, F. Nava and G. Ottaviani (1974). "Characterisation of the transport poperties of halogen doped CdTe used for gamma ray detectors." IEEE Trans. Nucl. Sci. **NS-21**: 331-341.

[122] Siffert, P., A. Cornet, R. Stuck, R. Triboulet and Y. Marfaing (1975). "Cadmium telluride nuclear radiation detectors." IEEE Trans. Nuc. Sci. **22**: 211-225.

[123] Figueroa, J. M., F. Sanchez-Sinencio, J. G. Mendoza-Alvarez, O. Zelaya, G. Contreras-Puente and A. Diaz-Gongora (1990). "Photoluminescence spectra and carrier mobilities in polycrystalline films of CdTe." Journal Of Crystal Growth **106**(4): 651-656.

[124] Norris, C. B. (1980). "Further investigation of the 1.4 eV luminescence in solution-grown CdTe:In." J. Appl. Phys. **51**(12): 6342-6347.

[125] Norris, C. B. and K. R. Zanio (1982). "Effects of Cd-vapour and Te-vapour heat treatments on the luminescence of solution-grown CdTe:In." J. Appl. Phys. **53**(9): 6347-6359.

[126] Halsted, R. E., M. R. Lorenz and B. Segall (1961). "Band Edge Emission Properties of CdTe." J. Phys. Chem. Solids **22**: 109-116.

[127] Norris, C. B. (1978). "Temperature, injection level and frequency dependencies of the luminescence in lightly and heavily doped CdTe:In." Journal of Luminescence **16**: 297-310.

[128] Norris, C. B. (1980). "Further investigation of the 1.4 eV luminescence in solution-grown CdTe:In." J. Appl. Phys. **51**(12): 6342-6347.

[129] Norris, C. B. and K. R. Zanio (1982). "Effects of Cd-vapour and Te-vapour heat treatments on the luminescence of solution-grown CdTe:In." J. Appl. Phys. **53**(9): 6347-6359.

[130] Figueroa, J. M., F. Sanchez-Sinencio, J. G. Mendoza-Alvarez, O. Zelaya, C. Vazquez-Lopez and J. S. Helman (1986). "Influence of Cd vacancies on the photoluminescence of CdTe." J. Appl. Phys. **60**(1): 452-454.

[131] Akimoto, K., H. Okuyama, M. Ikeda, Y. Mori (1992). "Oxygen doping in CdTe, CdS and ZnS." Journal Of Crystal Growth **117**(1-4): 420-423.

[132] Akimoto, K., H. Okuyama, M. Ikeda, Y. Mori (1992). "Isoelectronic oxygen in II-VI Semiconductors." Applied Physics Letters **60**(1): 91-93.

[133] Taguchi, T., J. Shirafuji and Y. Inuishi (1975). "Excitonic Emission in Cadmium Telluride." Physics Status Solidi B **68**: 727-738.

[134] Cooper, D. E., J. Bajaj and P. R. Newman (1988). "Photoluminescence Spectroscopy Of Excitons For Evaluation Of High- Quality CdTe Crystals." Journal Of Crystal Growth **86**(1-4): 544-551.

[135] Lee, J. S., N. C. Giles, D. Rajavel, C. J. Summers (1994). "Room temperature band edge photoluminescence from cadmium telluride." Physical Review B-Condensed Matter **49**(3): 1668-1676.

[136] Gold, J. S., T. H. Myers, N. C. Giles, K. A. Harris, L. M. Mohnkern, R. W. Yanka and D. P. M. W. M. M. E. L. S. N. W Virginia Univ (1993). "Photoluminescence From Heteroepitaxial (211)B Cdte Grown On (211)B Gaas By Molecular-Beam Epitaxy." Journal Of Applied Physics **74**(11): 6866-6871.

[137] Aguilar-Hernandez, J., G. Contreras-Puente, J. M. Figueroa-Estrada and O. Zelaya-Angel (1994). "Photoluminescence studies of semiconducting polycrystalline CdTe films." Japanese Journal Of Applied Physics Part 1-Regular Papers Short Notes & Review Papers **33**(1A): 37-41.

[138] Schmidt, T., G. Daniel and K. Lischka (1992). "The excitation power dependence of the near band edge photoluminescence of II-VI semiconductors." Journal of Crystal Growth **117**: 748-752.

[139] Schmidt, T., K. Lischka and W. Zulehner (1992). "Excitation power dependence of the near-band-edge photoluminescence of semiconductors." Physical Review B **45**(16): 8989-8994.

[140] Feng, Z. C., A. Mascarenhas, et al. (1986). "Low Temperature Photoluminescence Spectra of (001) CdTe Films Grown by Molecular Beam Epitaxy at Different Substrate Temperatures." Journal of Luminescence **35**: 329-341.

[141] Francou, J. M., K. Saminadayar, et al. (1985). "Luminescence Characterisation of Residual Impurites in CdTe grown by Molecular Beam Epitaxy." J. Cryst. Growth **72**: 220-225.

[142] Bimberg, D., M. Sondergeld and E. Grobe (1971). "Thermal dissociation of excitons bound to neutral acceptors in high purity GaAs." Physical Review B **4**(10): 3451-3455.

[143] Landolt-Bornstein (1982) "Numerical data and functional relationships in science and technology" Group 3- Crystal and Solid State Physics, Semiconductors "Physics of II-VI compounds", ed. Nimtz, Springer-Verlag, Berlin Heildelberg. 227

[144] Al-Allak, H. M., A. W. Brinkman, H. Richter and D. Bonnet (1995). "Dependence of CdS/CdTe thin film solar cells characteristics on the processing conditions." J. Cryst. Growth.

[145] Ringel, S. A., A. W. Smith, M. H. MacDougal and A. Rohatgi (1991). "The effects Of $CdCl_2$ on the electronic properties of molecular beam epitaxially grown CdTe/CdS heterojunction solar cells." Journal Of Applied Physics **70**(2): 881-889.

[146] Sobiesierski, Z., I. M. Dharmadasa, et al. (1990). "Photoluminescence As a Probe Of Semiconductor Surfaces - Cdte and Cds." Journal Of Crystal Growth **101**(1-4): 599-602.

[147] Galloway, S. A., P. R. Edwards and K. Durose (1997). "EBIC and cathodoluminescence studies of grain boundary and interface phenomena in CdTe/CdS solar cells." To be published.

[148] Palik, E. D. (1985). . Handbook of optical constants. E. D. Palik, Academic Press: 409-427.

[149] Al-Jassim, M. M., F. S. Hassoon, K. M. Jones, B. M. Keyes, R. J. Matson and H. R. Moutinho (1993). The morphology, microstructure and luminescent properties of CdS/CdTe thin film solar cells. Photovoltaic AR&D, AIP Conference Proceedings.

[150] Galloway, S. A., P. R. Edwards and K. Durose (1997). "EBIC and cathodoluminescence studies of grain boundary and interface phenomena in CdTe/CdS solar cells." To be published.

[151] Akimoto, K., H. Okuyama, M. Ikeda, Y. Mori (1992). "Oxygen Doping In CdTe, CdS and ZnS." Journal Of Crystal Growth **117**(1-4): 420-423.

[152] Akimoto, K., H. Okuyama, M. Ikeda, Y. Mori (1992). "Isoelectronic oxygen in II-VI Semiconductors." Applied Physics Letters **60**(1): 91-93.

[153] Siffert, P., A. Cornet, R. Stuck, R. Triboulet and Y. Marfaing (1975). "Cadmium telluride nuclear radiation detectors." IEEE Trans. Nuc. Sci. **22**: 211-225.

[154] Basol, B. M. (1992). "Processing high efficiency CdTe solar cells." Int. J. Solar Energy **12**: 25-35.

[155] Bell, R. O., F. V. Wald, C. Canali, F. Nava and G. Ottaviani (1974). "Characterization of the transport properties of halogen doped CdTe used for gamma ray detectors." IEEE Trans. Nucl. Sci. **NS-21**: 331-341.

[156] Fischer, A., C. Narayanswamy, D. S. Grecu, E. Bykov, S. A. Nance, U. N. Jayamaha, G. Contreras-Puente, A. D. Compaan, M. A. Stan and A. R. Mason (1996). Interdiffusion of CdS/CdTe in laser-deposited and RF sputtered alloys, bilayers and solar cells. 25th Photovoltaic Specialists Conference, Washington D. C., IEEE.

[157] Pal, R., J. Dutta, S. Chaudhuri and A. K. Pal (1993). "CdS_xTe_{1-x} Films - Preparation and Properties." Journal Of Physics D-Applied Physics **26**(4): 704-710.

[158] De Vos, A., J. E. Parrott, P. Baruch and P. T. Landsberg (1994). Bandgap Effects in Thin-Film Heterojunction Solar Cells. 12th European Photovoltaic Solar Energy Conference, Amsterdam, The Netherlands.